Leading to tomorrow

K¹S T oday

Korea Institute of Science and
Technology

Technical Reviews

Bio / Medical

Spatially and Temporally Controlled
Hydrogels for Tissue Engineering

Materials / Systems

Metallic MXene Saturable Absorber for
Femtosecond Mode-Locked Lasers

Energy / Environment

Preparation, Characterization, and
Application of TiO2-Patterned Polyimide
Film as a Photocatalyst for Oxidation of
Organic Contaminants

EXPLORING BRAIN CONNECTIVITY

Cover image_ **Dr. Keiko Yamamoto**   Center for Functional Cennectomics (see p.66 for interview)
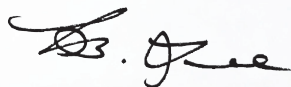
Contents

Foreword

Stephen Hawking, who recently passed away, once said, "*Intelligence is the ability to adapt to change.*" These words resonate in today's constantly changing and complex world. It seems clear that response to change is no longer a matter of choice but an absolute necessity.

For two consecutive years, KIST has been ranked 6th among the world's most innovative publicly funded research institutions, as evaluated by Thomson Reuters. In 2018, we launched The K-DARPA project in which we set challenging, target-oriented objectives in research fields that have low success rates but offer huge potential rewards for bettering lives and ensuring economic growth. I believe the act of taking on such research and thereby stepping into uncharted territory to be the very definition of innovation.

KIST's recent research is targeted on areas which will create an information-driven, technology-enabled future. For example, our researchers have identified factors that lower the performance of electric vehicle batteries and by developing innovative solutions in response, are initiating a new era in fuel technology. KIST researchers have also studied ways to utilize new materials, such as developing a technology that can generate broadband ultrashort laser pulses using MXene, a 2D advanced material.

Our goal in 2018 is to focus on the sources of change and take a leading role in responding to those changes with challenging research. We will continue our work in the fields of security and disaster relief and actively seek solutions to issues we face every day, such as environmental degradation or health challenges. Building a better future is what KIST is all about.

Dr. Byung Gwon LEE
President of KIST

Technical Review

Spatially and Temporally Controlled Hydrogels for Tissue Engineering

Introduction

Jung Mok SEO

Senior Researcher
Center for Biomaterials
Biomedical Research Institute

jungmokseo@kist.re.kr

Recent advances in biomaterials have allowed for a deeper understanding of the fundamentals of cell biology and fueled further development of novel pharmacological *ex vivo* models by recapitulating native physiological processes [1]. Moreover, biomaterials play a fundamental role in tissue engineering in which living replacements are fabricated to restore the functions of damaged tissues and organs. Advances over the last few decades have underscored the essential role of biomaterial design and engineering in improving the function of engineered tissue constructs [2]. In this article, we critically review the steps that are being taken to improve spatiotemporal control over the biomaterial properties of advanced biomaterials that could then facilitate the development of functional tissue-engineered constructs.

Traditionally, research related to biomaterials has centered on the development of biomaterials with novel compositions and properties [3]. At the same time, an intense effort has been made towards the chemical modification of known biomaterials to endow them with improved performance or specific new functions. Moreover, conventional research has focused on the static behavior of biomaterials, while recent findings suggest that spatial and temporal control of biomaterials provides unique opportunities to recapitulate the dynamic nature of the microenvironments in native tissues, which play a key role in controlling cell behaviors and functions.

In addition to advances in biomaterial chemistry, numerous engineering techniques have been developed to fabricate biomaterial constructs with unique spatial modifications and complex architectures [4]. Here we review the recent developments in biofabrication techniques, which have provided practical methods for fabricating biomaterials into relevant sizes, shapes, and compositions for regenerative medicine [5].

We also review the recent achievements in temporal control over biomaterials. While conventional approaches have focused on the controlled release of growth factors and drugs,

recent studies have been dedicated to transforming passive and static scaffolds into responsive and dynamic matrices [6]. Such new approaches are expected to play a major role in recapitulating the unique dynamic features of native extracellular matrix (ECM) to direct multistep biological processes, such as stem cell differentiation and functional tissue regeneration. We conclude by providing a perspective on the future challenges and opportunities in the development of biomaterials for tissue engineering applications.

Spatial control of hydrogels

Conventional hydrogels can be employed for the fabrication of scaffolds, which provide biomimetic chemical and physical microenvironments for the embedded cells to regulate their behaviors. However, these biomaterials lack the heterogeneity and dynamic changes observed in native tissues. Biomimicking the temporal and spatial characteristics of native tissues and organs requires the development of advanced hydrogels. In this section, we will review the recent approaches towards spatial control of hydrogels for tissue engineering to enhance cellular functionality and the therapeutic efficacy of implants.

Photo-patterning

Photo-patterning has rapidly evolved into a very powerful and flexible tool with many reported variations. Photo-patterning refers to the use of lights to form patterns using photo-crosslinkable hydrogels. In its simplest version, the surface of the material is covered with a photo mask containing
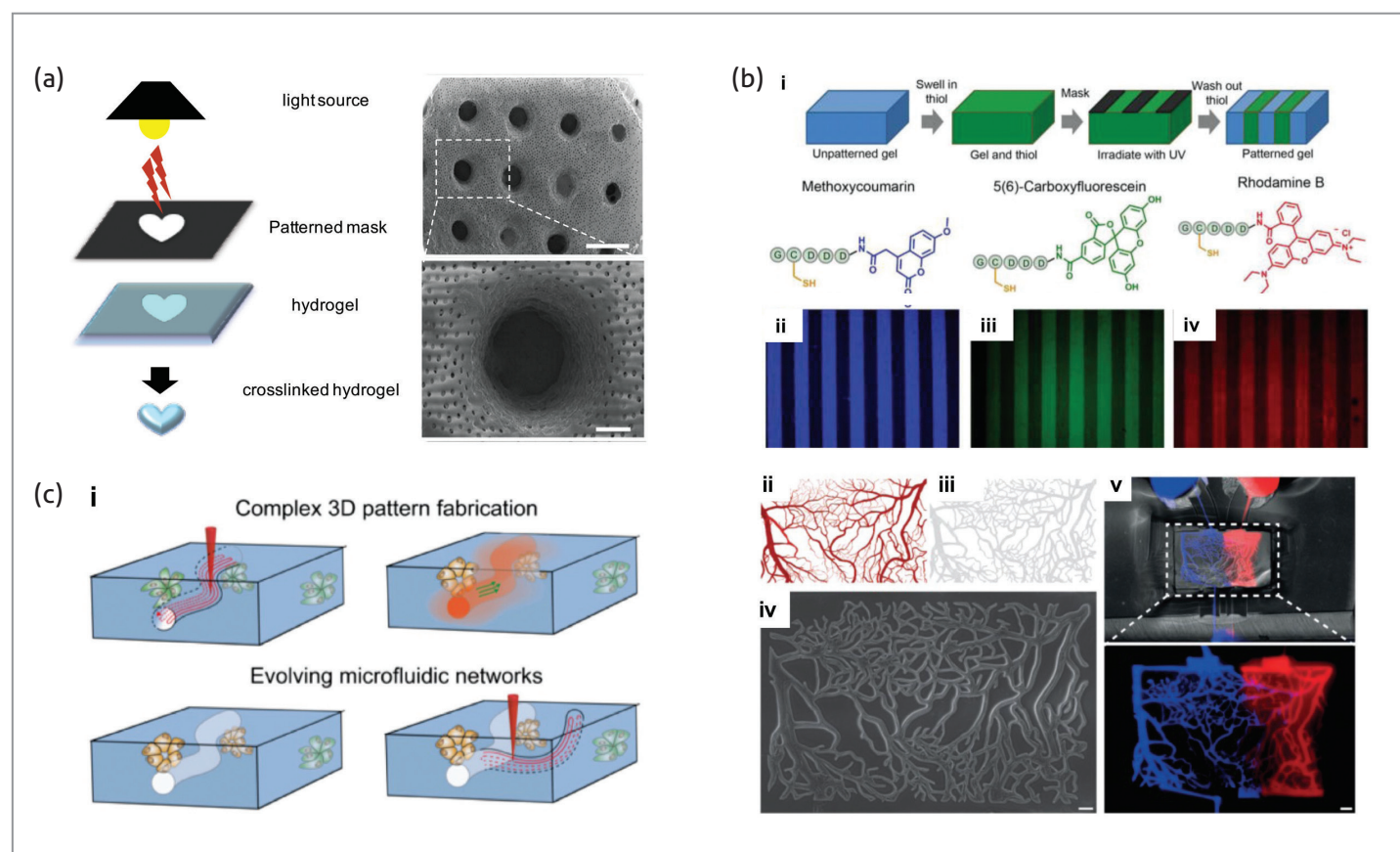
Figure 1   Photo-patterning of hydrogels. (a) Schematic representation of a simple photo-patterning process using a photo-mask and photo-patterned pores (62 µm) in porous pHEMA hydrogels. (b) Chemical patterning of hydrogels. (i) Schematic of process to photo-pattern NorHA gels with thiol-containing molecules. (ii-iv) Chemical structures of fluorescent-dye-terminated peptides with confocal images of photo-patterned NorHA gels with different dyes. (c) (i) Schematic of a fully-controlled maskless laser system that enabled the microfabrication of convoluted microfluidic channels within hydrogels. (ii, iii) Photographs of a capillary bed and mask showing the complexity of the fabricated networks. (iv) Resulting microfluidic capillary network. (v) Connected and perfused network using two different fluorescent molecules

Bio / Medical

Materials / Systems

Energy / Environment

Research Highlights

KIST News

Up Close

Interview

a pre-designed pattern, which locally shields the material from light exposure and subsequent chemical modification of a photo-sensitive material. The work by Bryant et al. represents an example of photo-micropatterning of crosslinkable hydrogels [7]. The authors used a photo mask with microscale circular opaque islands to pattern circular pores onto the surface of photo-crosslinkable PHEMA hydrogels (Figure 1a). In addition to this research, work has been conducted in the photo-patterning of chemical signals, an important step forward to selectively endow (or activate) chemical cues in specific regions of a hydrogel construct with precise spatial control. Gramlich et al. used a norbornene-functionalized HA (NorHA) and the click photo-reaction with dithiols to photo-pattern hydrogels (Figure 1b) [8]. The use of masks with specific patterns enabled the functionalization of specific regions of the hydrogels by exposure to light. The control of the spatial distribution of the dithiol groups allowed the selective induction of secondary reactions.

New laser illumination techniques developed in the last decade have provided new and more precise ways to fabricate 3D microstructures within hydrogels. One of these systems, based on the phenomenon of two-photon absorption, has enabled direct "writing" of micropatterns with nanoscale precision [9]. Two-photon hydrogel polymerization (2PP) platforms use a femtosecond laser source. The intensity of the laser beam is highly regulated and therefore allows for printing within cell-laden hydrogel matrices through the precisely localized excitation of photo-initiator molecules. This polymerization technique enables a uniquely high resolution of 3D patterning (Figure 1c) [10]. In addition, obtaining complex architectures, including perfusable microvessel structures, is feasible once proper computer-aided design files are produced [11-13]. However, the potential to produce complex micropatterns at remarkable resolutions comes at the price of low fabrication speed. When fabricating larger constructs, a single structure could take hours to days to complete, thus limiting the practical applications of 2PP for large scale endeavors towards cell-laden constructs.

Microfluidics-assisted fabrication

The term microfluidics refers to a set of scientific/technological disciplines and resources that enable the manipulation of small volumes of fluid (or small flow rates) through narrow channels or small spaces [14]. Microfabrication is one of the many relevant applications of microfluidics; indeed, microfluidics-assisted fabrication has been previously reviewed [15].

Microfluidics has expanded our tool set for engineering the geometry, composition, and functionality of hydrogel constructs. Microfluidic systems are particularly pertinent for engineering hydrogels for a number of reasons, including their intrinsic capacity to produce flow alignment. Hydrogels are typically prepared from viscous liquids that can be dispensed, dosed, or extruded through microfluidic systems. The laminar flow that prevails in microfluidic systems is a powerful tool for microfabrication. In addition, the small size of microfluidic systems enables a tight control of relevant fabrication conditions, such as heat transfer rates, mass transfer rates, surface tension, and chemical microenvironments.

The use of microfluidic systems has been widely exploited for the microfabrication of hydrogel structures. Microfluidic platforms have been used to microfabricate hydrogel spheres with well-defined diameters, architectures, and chemical compositions [16-20], as well as fibers of specific architecture, including hollow fibers and gradients within hydrogels [21]. Numerous studies have demonstrated the generation of cell-laden hydrogel microparticles using microfluidic devices [20]. Recent innovations have even allowed for microfluidic encapsulation of individual cells in microgels that are only marginally larger than the cell they contain [22]. Spatial placement of the cell in these microgels is of high importance to prevent cell egression; it has been reported that delayed on-chip gelation places cells in the microgel's center, which enables long-term culture [23]. Frequently, hydrophilic hydrogel precursor solutions are co-flown with a hydrophobic liquid, such as oils in a microfluidic channel to generate microdroplets of liquid hydrogel precursor. These microdroplets are subsequently crosslinked within the microfluidic channels or at the outlet by exposure to a crosslinking agent, such as light, heat, chemical reagent, or enzyme that is added downstream. These microfluidic channel systems provide a level of process control that is far superior to those achievable in traditional synthesis methods. Almost perfectly spherical hydrogel microparticles of a precise diameter, and with a very narrow particle-size distribution, can be generated in a facile manner using microfluidic methods. Manipulation of operative parameters, such as the nature of the hydrophobic phase, hydrogel precursor solution, hydrophobic/hydrophilic ratio, flow rate, chemical environment within the channel, and the diameter of the microfluidic channel, allow tight control of shape, diameter, and functionality of the generated microparticles [24].

Microfluidic systems allow for the straightforward tailoring of well-defined physical and chemical microenvironments for cell proliferation, function, or differentiation. Each hydrogel particle can be viewed as an individual tissue micro-niche, i.e., a well-defined cell microenvironment, where the chemical and physical properties can be controlled by dosing chemical and physical cues in the precursor solution. As an example, the fabrication of PEGDA/heparin hydrogel microspheres for the high-throughput encapsulation of mouse embryonic stem cell (ESCs) has been explored and demonstrated the rapid formation of embryonic spheroids with enhanced differentiation [17]. Specifically, a simple microfluidic device was used to co-inject the PEGDA precursors, methacrylated heparin and 8-arm PEG-thiol to produce cell-laden spheroids containing appropriate chemical microenvironments for the proliferation of ESCs and to guide their endodermic differentiation.

Fibers are ubiquitous in natural tissues. Neurons, muscle fibers, and tendons are only some of the many examples of fibrous tissue units in the human body. The fabrication of hydrogel fibers with predefined architectures is therefore of great interest to tissue engineers. Microfluidic platforms have found an important niche in this field, as microfluidic systems behave like microfiber extruders.
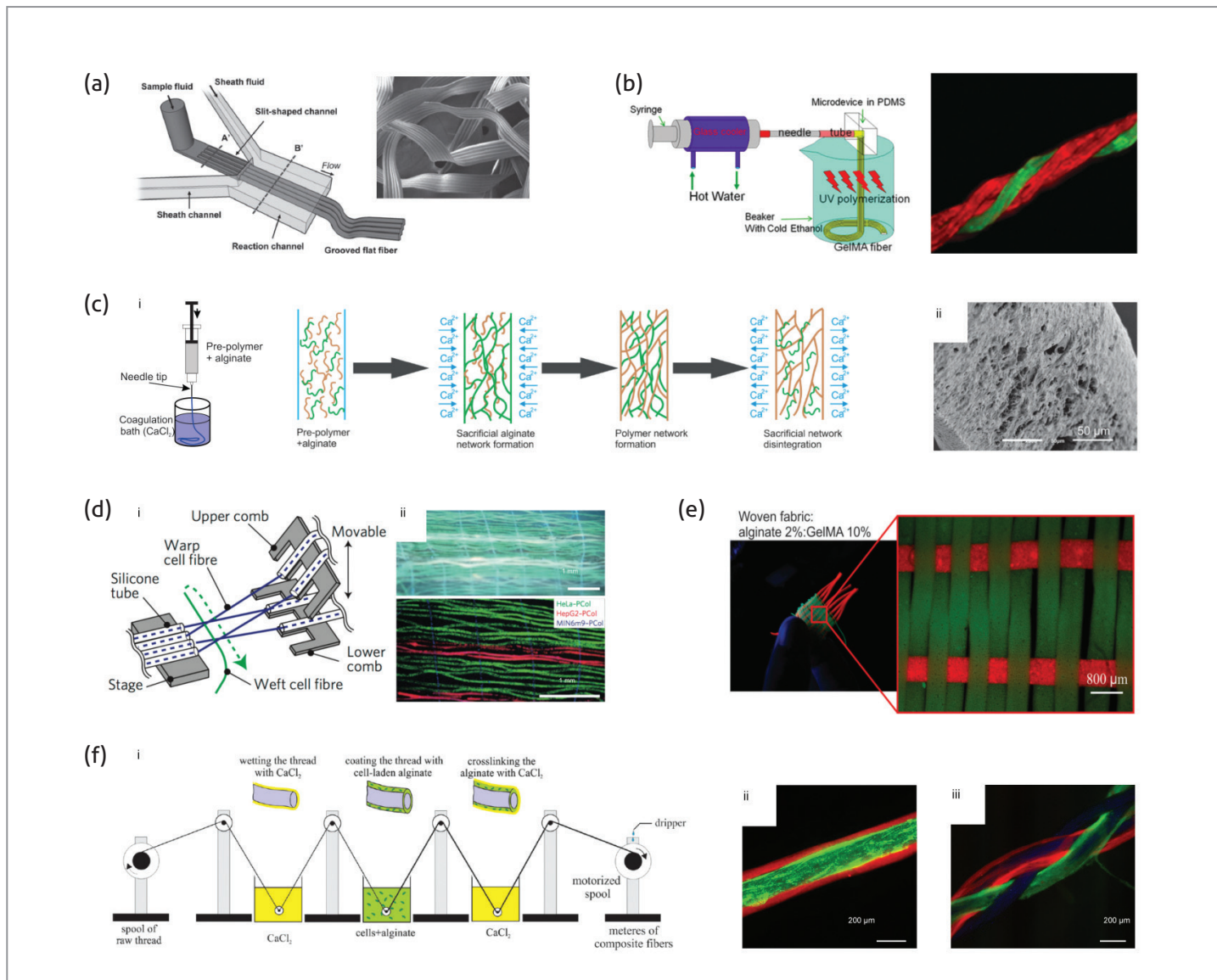
Textile processes for forming complex tissues

Despite the groundbreaking progress of the aforementioned techniques for spatial control of hydrogel shape, it has remained a true challenge to create large constructs with in-depth complexity at the microscale. Textile-like processing of hydrogel fibers has emerged as a powerful tool for fabrication of large 2D and pseudo-3D constructs with tunable mechanical properties, architectures, and patterns. These properties are well aligned with the expectations of ideal scaffolds for tissue engineering applications [25-28]. In addition, the similarity between textile-based fabrics and some tissues, such as muscle, tendon, and ligament, has fueled interest for their use in tissue engineering [29]. Thus, textile technology based on weaving, braiding, and knitting has been used for the engineering of various tissue constructs [30]. Woven hydrogel fabrics can provide anisotropic mechanical properties usually with a higher mechanical strength in the planar directions. In addition, their mechanical strengths in the through-plane direction can be enhanced by interlocking multiple layers of 2D hydrogel fabrics [31, 32].

In the past decade, fibers have been fabricated from a variety of natural polymer-based hydrogels that could carry cells [33-37]. The main methods used for fabrication of cell-laden fibers include wet-spinning, microfluidic spinning, and interfacial complexation [29]. In the case of wet-spinning, the prepolymer is injected into a reservoir containing compounds, and the formation of stable fibers requires a rapid crosslinking rate of the prepolymers to limit the undesired diffusion into the surrounding solution. To this end, alginate has been frequently used for the fabrication of cell-laden fibers through wet-spinning, as alginate can be rapidly crosslinked by divalent ions, such as Ca^{2+} to form biocompatible physical hydrogels [32].

Microfluidic-based wet-spinning has a similar crosslinking process with a major difference being that the precursor and crosslinker are flown co-axially through a microchannel [38-40]. Both methods have been widely used for the fabrication of cellular and acellular fibers. The use of sophisticated microfluidic systems has enabled the formation of fibers with multiple compartments and materials [40-42]. In addition, the surface topography of the fibers and their shape can be tuned through the use of non-circular nozzles (Figure 2a) [43]. Although the majority of the cell-laden fibers fabricated using this technique have been limited to alginate-based materials, recent methods have been proposed for fabrication of fibers from other hydrogels with a slower crosslinking rate. In one example, GelMA hydrogel prepolymer solution was injected into a low-temperature solution to induce rapid thermally-induced gelation, after which the solidified fibers were photo-crosslinked to form stable constructs (Figure 2b) [40, 44]. However, this method suffered from significant dispersion of the hydrogel stream into the cold aqueous solution, resulting in poor controllability of the composition of the final fibers. To address this issue, sacrificial polymeric templates were introduced to assist in generating fibers (Figure 2c) [44]. In this method, the target polymer was mixed with alginate and then injected into a $CaCl_2$ crosslinking solution. The alginate component was crosslinked to physically entrap the polymer chains. A secondary crosslinking process was carried out to form an interpenetrating polymer network (IPN) hydrogel. Alginate was then dissolved by a calcium-chelating agent to leave behind a stable fiber composed of the targeting polymer. Interfacial complexation is another fabrication method that has been widely used to produce cell-laden fibers [45]. In this method, two solutions with a strong interaction (mostly electrostatic) are interfaced and crosslinked. The interface layer is pulled using a needle to form stable fibers. However, controlling the fiber dimension and morphology using interfacial complexation needs to be improved.

Bio / Medical

Materials / Systems

Energy / Environment

Research Highlights

KIST News

Up Close

Interview

Figure 2   Various platforms for the engineering of cell-laden fibers and constructs. (a) Fabrication of flat alginate fibers using microfluidic systems with irregular-shaped nozzles. (b) Fabrication of GelMA fibers by injecting GelMA precursor into a cold bath of ethanol followed by UV irradiation. The fibers were mechanically stable and multiple fibers could be twisted together. (c) The use of sacrificial templates for engineering hydrogels fibers from different polymers. (i) Schematic of fiber fabrication platform and the fiber formation process. (ii) Typical fabricated GelMA hydrogel fiber after alginate dissociation confirming the stability of the fibers. (d) (i) A microweaving loom for fabrication of hydrogel constructs and (ii) a fabricated construct. (e) Centimeter-scale hydrogel fabric engineered from hybrid alginate: GelMA hydrogels. (f) (i) Fabrication of composite fibers by coating polymeric fibers with a layer of cell-laden hydrogel. (ii) A typical composite fiber generated by coating two distinct layers of microbead-laden hydrogel. (iii) Micrograph showing a typical braided construct from composite fibers.

Cell-laden hydrogel fibers are typically fragile and their assembly using textile processes is not trivial. However, a few reports have managed to fabricate cell-laden hydrogel fibers and assemble them using textile processes [46, 47]. A microweaving loom was designed to reduce the exerted mechanical forces during the weaving process (Figure 2d) [45, 48]. However, the density of the generated fabric and the resolution of woven patterns were limited. As another approach, IPN hydrogel fibers were generated with higher mechanical strength and were assembled using manual miniaturized weaving looms and also were braided into centimeter-scale fabrics (Figure 2e) [48]. The resolution of the generated constructs was comparable to commercial conventional textile platforms for fabrics. Although the engineered hydrogel fabrics did offer anisotropic mechanical properties, their strength was still significantly lower than those observed in native tissues.

Since the successful implantation, integration, and function of engineered constructs rely on mimicking the tissue-level mechanical properties, tremendous effort has been dedicated to the fabrication of composite constructs. Many researchers have used textiles as reinforcing mats to strengthen cell-laden hydrogels [45]. Specifically, the hydrogel provides a nurturing environment for cellular growth, while the fabric provides the mechanical support and ensures the physical stability of the construct. However, controlling both the mechanical properties and the cellular distribution at the same time has been difficult. A potential solution was to coat mechanically strong core fibers with a layer of cell-laden hydrogels [31, 49]. It was shown that the mechanical properties of braided constructs could be tuned by three orders of magnitude while the cellular pattern could be preserved in the 3D environment (Figure 2f) [50]. As such, this technology is uniquely suited to simultaneously control the spatial mechanical properties and cellular distribution of engineered tissue constructs. Composite fibers have been assembled using manual weaving looms and have been knitted similarly to regular threads. However, there are still key challenges associated with these composite fibers, including the detachment of the hydrogel layer from the core fiber.

Overall, biotextiles have emerged as a powerful tool for engineering spatially organized tissue constructs with clinically relevant dimensions. Hydrogel fibers have been widely used as acellular scaffolds, and recent advancements have enabled the fabrication of cell-laden fibers as miniaturized textile platforms to engineer tissue constructs. A key advantage of the textile processes is their ability to mimic tissue-level and cell-level properties independently. This unique feature distinguishes textile-based technology from all other microfabrication technologies. However, there are several challenges to be resolved to enable their practical translation. The resolution associated with textile processes has remained poor and requires improvement. Moreover, the current potential applications of this technology have been limited to the engineering of fibrous tissues.

Temporal control of hydrogel

In the past few decades, hydrogels have been developed to mimic native ECMs and are commonly utilized as cell culture substrates, partly due to their high water content, tunable material properties, and biocompatibility. As chemically or physically crosslinked network structures, hydrogels not only provide the mechanical support for cell attachment and survival, but can also present biophysical and biochemical cues to direct cell function. However, the native ECM of living cells is highly dynamic in nature and adapts its properties and structures through various biological processes to guide the response of the encapsulated cells to the changing microenvironmental conditions. This temporal control of the chemical and physical microenvironment of cells plays a vital role in tissue development, homeostasis, and pathology. To recapitulate this important dynamic feature, it would be ideal to develop strategies to temporally control the physical and biochemical properties of hydrogels, e.g., in terms of mechanical stiffness, degradation, as well as the presence of drugs and bioactive moieties.

Reversible tuning of biochemical properties

The complexity of native ECM is further reflected by not only the presence of certain signaling molecules but also their removal at proper time points. Therefore, it is of great interest to develop strategies towards reversible tuning of the ligation and release of bioactive moieties, such as cell-adhesive RGD peptide sequences to control cell spreading and migration in the hydrogel microenvironment [51].

To achieve this, an elegant combination of photo-cleavable linkages and biorthogonal, 3D-patternable click hydrogel systems was reported. A benzyl ether linker was introduced between the thiol groups and the bioactive motifs [52]. 3D patterning of the click hydrogels could be finished with a visible light source [53], while the photo-cleavage was realized under UV light. Using this design, the authors demonstrated patterned addition and subsequent removal of the bioactive molecules within the hydrogel network [52].

Recently, another study reported fully reversible patterning of full-length proteins in a synthetic click PEG hydrogel system. Here the hydrogel network was formed by the SPAAC reaction, functionalized with benzyl ether-protected alkoxyamine groups [54]. As the first step, selective cleavage of the protection groups permitted protein ligation via oxime bond formation. Moreover, treatment of proteins with a special linker molecule with both o-benzyl ether linkage and aldehyde groups enabled both controlled photo-patterning and photo-cleavage. Dual protein patterning was demonstrated with selective subsequent removal of each individual component.

Bio / Medical

Materials / Systems

Energy / Environment

Research Highlights

KIST News

Up Close

Interview

The reversible presence of biochemical cues represented a step forward in our capability to spatiotemporally control hydrogels.

Gandavarapu et al. developed another reversible ligand exchange strategy for dynamic modulation of biochemical motifs [55]. The authors reasoned that allyl sulfide functional groups could be applied to achieve reversible exchange of functional moieties due to fast equilibrium switching when the allyl sulfide group was attacked by a thiyl radical [55]. By consecutively adding new thiolated ligands and a photo-initiator, the present motifs could be replaced *in situ* via an exchange reaction mechanism. Co-patterning of multiple ligands could be possible by careful kinetic control of the exchange reaction. These seminal examples illustrate the concepts and potential methods towards fully reversible control of the dynamic presentation of biochemical cues in hydrogels.
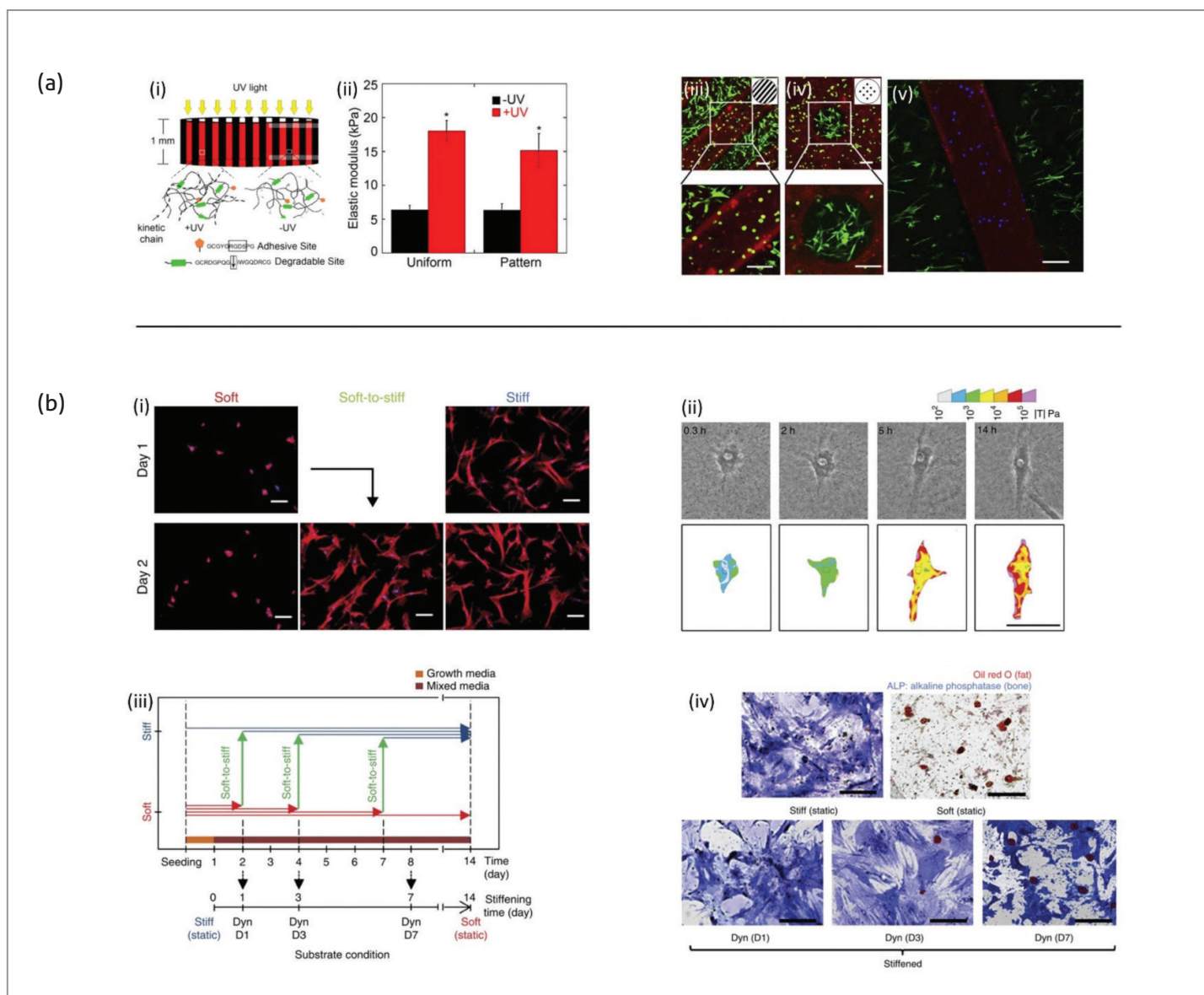
Mechanical stiffness modulation

During the past decade, the effects of mechanical cues in cellular microenvironments to direct cell behaviors have gained increasing attention. Mechanotransduction, which refers to the process of transferring mechanical stimuli to chemical or electrical signals, has been found to play an important role in dictating cell proliferation and differentiation. Engler et al. first identified that the *in vitro* differentiation of MSCs could be tuned by merely changing the mechanical stiffness of the culture substrate [56]. Lineage specification affected by substrate mechanical characteristics was attributed to nonmuscle myosin II, which is an actin-binding protein that controls cell adhesion and migration. Moreover, a recent study revealed that stem cells might potentially possess mechanical memory by sensing and storing the mechanical information from culturing history, which could determine their fate at a later stage [57]. These results highlight the necessity to develop strategies to temporally control the mechanical properties of hydrogel matrices in cell culture studies.

The mechanical strengths of hydrogels rely on their crosslinking density. Therefore, hydrogel stiffness can be increased or decreased with time by increasing or decreasing the number of crosslinking sites. To obtain hydrogels that can stiffen over time, several approaches have been explored. For example, Young et al. reported the use of a kinetically slow crosslinking reaction to achieve hydrogel stiffening within a time scale that is reminiscent of tissue development [58]. In their study, they characterized the crosslinking kinetics of thiolated HA with a PEGDA crosslinker of different molecular weights and found a hydrogel formulation that gradually stiffened from 1 kPa to 8 kPa over a period of two weeks. This kinetic evolution was similar to tissue elasticity evolution during the development of a chicken heart, which resulted in enhanced cardiac cell marker expression of cells cultured on the dynamic hydrogels. Despite this elegant design, the reaction kinetics between the thiol and acrylate groups are fixed by the reaction condition and offer little space for further manipulation.

Sequential multi-step crosslinking mechanisms towards the temporal tuning of hydrogel stiffness have also been explored via user-triggered methods, which allow for abrupt changes in hydrogel stiffness at precise points post-gelation. Photo-polymerization has traditionally been one of the powerful methods to prepare chemically crosslinked hydrogels as it allows convenient spatial and temporal control of the crosslinking reaction. Importantly, the degree of photo-polymerization reaction is dependent on a light irradiation dose [59]. As a result, it is possible to take advantage of the dose-dependent crosslinking density since it leaves unreacted functional groups within the hydrogel matrix which can be subsequently crosslinked in a second step to increase mechanical strength at a time point of choice [59-65].

Khetan et al. reported a novel sequentially crosslinked hydrogel system leading towards spatial and temporal control over hydrogel compositions and properties [60]. They synthesized an acrylate-modified HA, which could be crosslinked via an addition reaction using peptide crosslinkers with two end-capped thiol groups and an MMP-cleavable sequence. This first crosslinking step generated hydrogels that allowed cell remodeling by breaking the peptide crosslinkers. By tuning the feed ratio of the peptide crosslinker, a portion of the reactive acrylate groups remained unchanged after the first crosslinking reaction, which permitted a second crosslinking by photo-polymerization (Figure 3a). The resulting double-crosslinked hydrogels were mechanically stiffer than their precursor hydrogels, and the enzymatically inactive crosslinking sites blocked the cell spreading via matrix remodeling [60]. This study provided the possibility to manipulate cell behaviors through temporal control over matrix properties. Moreover, this system was also compatible with spatial patterning procedures due to the application of the photo-polymerization technique. Besides tuning cell spreading, the authors further demonstrated that the spatially-patterned hydrogels could lead to an entirely different adipogenic/osteogenic fate of encapsulated MSCs through spatiotemporal control of hydrogel crosslinking modes [62].

Bio / Medical

Materials / Systems

Energy / Environment

Research Highlights

KIST News

Up Close

Interview

Figure 3 Representative examples of dynamic stiffening hydrogels. (a) (i) Schematic illustration of a two-step crosslinking strategy to selectively stiffen HA hydrogel zones via photo-patterning. (ii) Comparison of elastic moduli of uniform HA hydrogels and selectively stiffened HA hydrogel zones measured by atomic force microscopy (AFM) (p < 0.05). (iii-iv) Images showing that spreading of encapsulated hMSCs in uniform and photo-patterned HA hydrogels only occurred in regions not exposed to UV light (scale bars, 100 μm). (v) Representative immunostaining images showing selective differentiation of hMSCs towards adipogenic and osteogenic lineage in +UV or -UV HA hydrogels, respectively. Fatty acid binding protein was stained as blue while osteocalcin appears as green (scale bar, 100 μm). (b) (i) Spreading of hMSCs cultured on MeHA substrates showed dependence on substrate stiffness (scale bar, 100 μm). (ii) Time-resolved phase-contrast images and traction stress maps of an hMSC showed response of cell traction force to *in situ* substrate stiffening (scale bar, 50 μm). (iii) Schematic illustration of timeline for temporal stiffening experiments of hMSCs' osteogenic differentiation. (iv) Representative images of hMSCs stained for ALP (osteogenesis) and lipid droplets with oil red O (adipogenesis) after 14 days of culture (scale bars, 50 μm).

Stiffening the HA hydrogels via a second photo-crosslinking mechanism provided a unique and dynamic platform to investigate the effects of abrupt changes in matrix stiffness on cellular behavior and responses given the fact that matrix stiffening in native ECM might be related to tissue regeneration or disease development. Using this platform,

Khetan et al. investigated the cell responses to matrix stiffening in both short-term and long-term time scales in 2D models (Figure 3b). Their results indicated that MSCs cultured on the stiffened hydrogels could sense stiffness changes quickly and showed increased area and traction within hours of the second crosslinking [62]. On the other hand, when MSCs were

cultured in a mixed medium that supported both osteogenic and adipogenic differentiation, the differentiated cell populations demonstrated interesting dependence on the cultured time over hydrogel matrix with different stiffness. MSCs cultured longer on softer matrix tended to differentiate towards adipogenic lineage, while early stiffening of the hydrogels resulted in preferred osteogenic differentiation [62]. These results were consistent with the discovery that stem cells could hold memory of mechanical information [66].

It should be noted that the secondary crosslinking by photo-polymerization of acrylate groups not only stiffened the HA-based hydrogels, but also introduced more non-degradable crosslinking sites. This temporal change of degradability along with mechanical characteristics in the HA-based dynamic hydrogel systems was found to influence stem cell differentiation in 3D cell culture [61]. Khetan et al. further revealed that when encapsulated in this HA hydrogel, differentiation of MSCs showed dependence on the generation of cellular traction due to degradation of the matrix, which was found to be independent of hydrogel stiffness and cellular morphology. In particular, even at identical hydrogel elasticity, when embedded in MMP-degradable HA hydrogels after the first crosslinking, MSCs exhibited high traction and enhanced osteogenesis; on the other hand, the secondary crosslinking resulted in hydrogels with restricted cell-mediated degradation and preferred adipogenesis of encapsulated MSCs [61]. These findings provide more information to understand cell-biomaterial interactions in 3D dynamic, biomimetic microenvironments.

With this dynamic biomaterials-based *in vitro* cell culture model that recapitulates *in vivo* ECM stiffening, both the Burdick and Wells groups investigated how the differentiation of hepatic stellate cells (HSCs) was influenced by matrix stiffness. Differentiation of HSCs into myofibroblasts has been closely related to tissue fibrosis, which might be partially attributed to ECM stiffening during disease development. Their results confirmed that HSCs cultured on stiffer hydrogels (~24 kPa in elasticity) expressed higher levels of alpha-smooth muscle actin (α-SMA) and type I collagen, as compared to HSCs on softer hydrogels (~2 kPa) [63, 65]. These results suggest that the dynamic nature of such hydrogels could be leveraged to study biological processes related to ECM stiffening *in vitro*; a feat that is not easily achieved in traditional static hydrogels.

In situ stiffening of hydrogels to tune cellular behavior has also been demonstrated by Marby et al. in a PEG hydrogel system with MMP-cleavable peptide crosslinkers. Stiffening of cell-laden PEG hydrogels was achieved by diffusing 8-arm PEG derivatives into the base hydrogel to form the second crosslinking network. Responses of valvular interstitial cells encapsulated in 3D hydrogels to the mechanical change were evaluated to reveal different behaviors compared with those from 2D cell culture models [67]. Recently, dynamic hydrogels capable of *in situ* secondary crosslinking were obtained by using an ABA-triblock copolymer. The A-blocks were modified with coumarin side groups, which could undergo photo-dimerization upon UV irradiation to introduce additional crosslinking sites. The UV-initiated crosslinking reaction led to varied viscoelastic properties of the hydrogel matrix, which was found to influence the behavior of encapsulated cells [68]. However, as the photo-dimerization reaction of coumarin moieties is kinetically slow and of relatively low efficiency, potential cell damage associated with long-term exposure to UV light could be a potential concern.

Multiscale materials with multiple scale lengths

Native tissues have precise control over cell behaviors via an arsenal of stimuli that spans across multiple length scales. Developing functional multiscale materials that provide pre-designed cues to cells at the nano- (atomic and molecular-sized), micro-, and macroscale in a unified architecture is a prerequisite toward truly biomimetic biomaterials (Figure 4) [69]. The concept of bottom-up tissue engineering offers a promising pathway to generate multiscale structures via assembling heterogeneous synthons, such as proteins, nucleic acids, cells, nanoparticles, and other bioactive components within the cell-laden hydrogel matrices.

The hierarchical arrangement of nanoscale compartments in a microscale unit is crucial to achieve the desired mechanical, physical, and chemical characteristics of the multiscale materials. Such precise hierarchical arranging of, for example, cells inside the tissue, eventually outline the cell-cell contacts and paracrine signaling to dictate cellular behavior and subsequently construct function. Creation of sophisticated multiscale units not only necessitates the understanding of interactions ranging from the molecular level to macro scale, but also permits reconstruction and re-engineering of the complexity that nature has developed over billions of years. As yet, several strategies have been developed to fabricate multiscale architectures, which have provided new opportunities
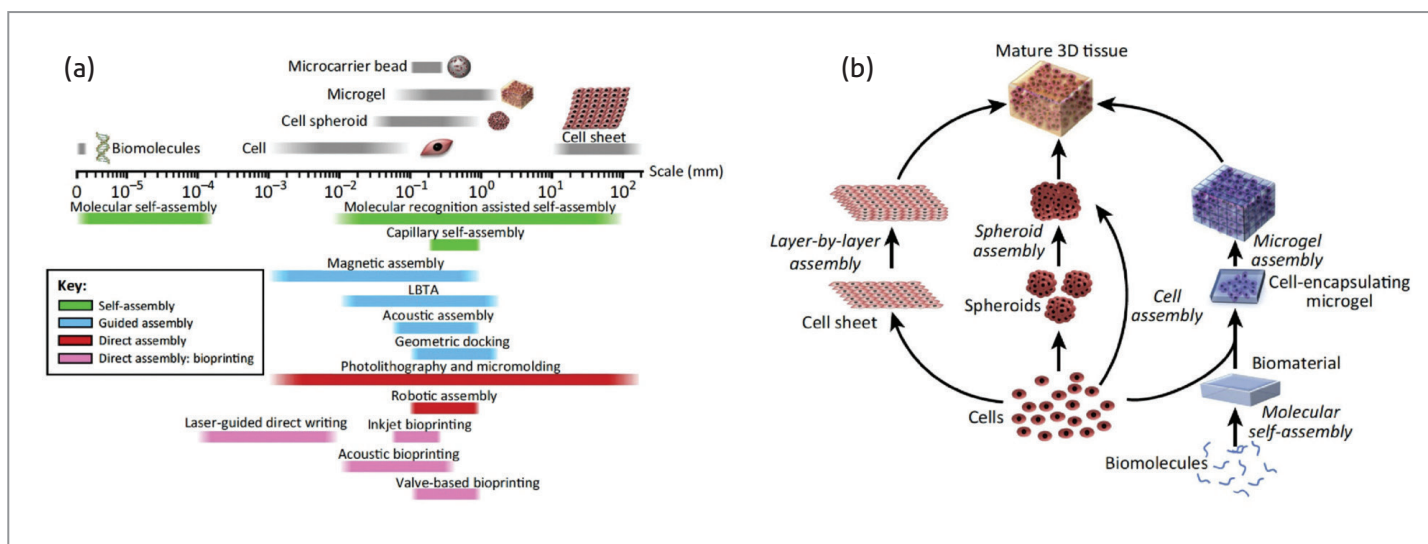
Figure 4　(a) Existing technologies for assembling building units (shown above the scale) at varying sizes. (b) Schematic of multiscale organization technologies from bottom to top for designing 3D tissue architectures.

to mimic the organization of native tissues to realize biomimetic engineered tissue constructs.

　　Supramolecular chemistry based on bio-macromolecules in which biological information can be loaded using self-assembling units of DNA or proteins represents a promising method to engineer multiscale structures. It has been shown that the supramolecular structures can be constituted from

single-stranded *ss*-DNA and peptides (e.g., RGDs), which offer a facile pathway to investigate the effects of nanotube architecture and peptide bioactivity in cellular function (Figure 5a) [70]. DNA origami is another promising approach to create nanoarchitectures and decorate specific functionalities at precise and controlled locations, which not only can help to understand the function of individual moieties, but also can controllably
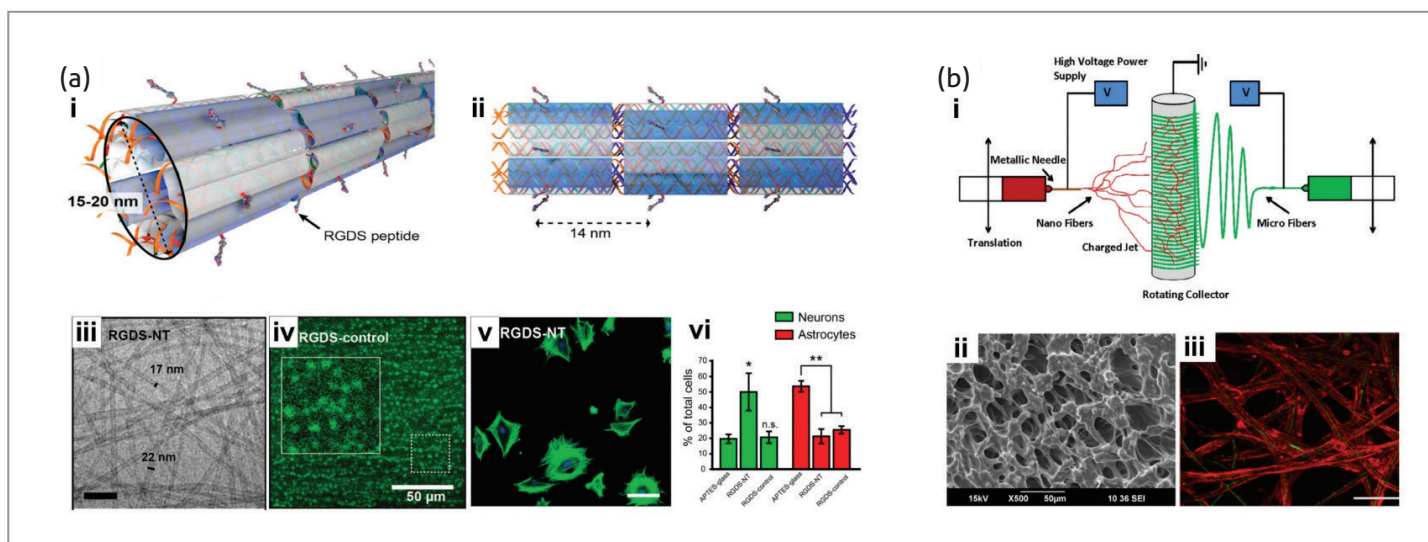
Figure 5　(a) (i, ii) Schematic illustration of RGD-functionalized DNA nanotubes with a comparable organization of the tiles and size of the peptide with respect to the DNA, (iii) its cryo-TEM characterization and (iv-v) cellular behavior. (b) (i) Schematic depicting a dual-electrospinning setup. (ii, iii) Characterization of generated multiscale PCL nano/micro fiber and *in vitro* cellular reaction of PCL random multiscale fibers coated with Ch-HA.

emulate cellular microenvironments. It has been shown that the precise positioning of ephrin-A5 in nanofabricated DNA origami scaffolds can regulate the degree of activation in EphA2 receptor in human breast cancer cells and control the invasive characteristics of cancer cells [71]. This opens a unique opportunity to control nano-organization and macroscale function by spatially positioning ligands for the activation of specific receptors to dictate cellular behavior.

Electrospinning has proven to be a practical method to fabricate nanoscale fibers for a wide range of materials in a facile step. However, pre-made nanofibers might find novel application when merged in bio-inks to afford macroscale hydrogel constructs with nanoscale spatial control. It has been shown that solutions of nanofibrillated cellulose had excellent shear-thinning characteristics, which can be combined with alginate to yield a unique cell-laden bio-ink for 3D bio-printing of living tissues [72]. Simultaneous electrospinning of nano and microfiber has led to the formation of multiscale fibrous scaffolds of PCL, which was combined with a chitosan hydrogel for ligament regeneration [73]. This scaffold induced rabbit ligament fibroblast cells to elongate along the aligned PCL fibers, which is required for the native ligament tissue microenvironment (Figure 5b). Furthermore, electrospinning has been integrated with 3D fiber deposition to create a multiscale scaffold of a PEG/poly(butylene terephthalate) (PBT) block copolymer that possessed a microarchitecture similar to the native tympanic membrane [74]. *In vitro* studies have revealed that hMSCs cultured on these scaffolds remained viable and metabolically active and arranged along architectural directions of the scaffold. This study paves the way for multi-scale, multi-compound, and multi-functional engineered tissues which could potentially better mimic the complexity of native tissues.

Conclusions

In summary, the field of hydrogel-based biomaterials is rich with strategies for engineering material constructs with innovative functionalities and physicochemical properties. Of particular note are the chemical modifications and technological platforms that have granted spatial and temporal control over various hydrogel systems. Advancing hydrogels from static to dynamic experimenter-controlled systems is expected to expand our capability to guide complex and multi-faceted cellular processes such as stem cell differentiation and tissue

regeneration. Recently developed high-throughput platforms are expected to aid in the identification of high-performing formulations, which might accelerate the translation of these promising advanced biomaterials.

Note

This article and images are drawn from "Spatially and Temporally Controlled Hydrogels for Tissue Engineering" *in Material Science and Engineering R: Reports*, 2017; Vol. 119: 1-35.

References

[1] Leijten J, Khademhosseini A. *Cell Stem Cell* 2016; 18: 20-4.

[2] Kaushik G, Leijten J, Khademhosseini A. *Stem Cells* 2016; 35: 51-60.

[3] Lutolf MP, Hubbell JA. *Nat. Biotechnol*. 2005; 23: 47-55.

[4] Leijten J, Rouwkema J, Zhang YS, Nasajpour A, Dokmeci MR, Khademhosseini A. *Small* 2016; 12: 2130-45.

[5] Mandrycky C, Wang Z, Kim K, Kim DH. *Biotechnol. Adv*. 2016; 34: 422-34.

[6] Kirschner CM, Anseth KS. *Acta Mater*. 2013; 61: 931-44.

[7] Bryant SJ, Cuy JL, Hauch KD, Ratner BD. *Biomaterials* 2007; 28 :2978-86.

[8] Gramlich WM, Kim IL, Burdick JA. *Biomaterials* 2013; 34: 9803-11.

[9] Torgersen J, Qin XH, Li Z, Ovsianikov A, Liska R, Stampfl J. *Adv. Funct. Mater*. 2013; 23: 4542-54.

[10] Brandenberg N, Lutolf MP. *Adv. Mater*. 2016; 28: 7450-6.

[11] Ovsianikov A, Deiwick A, Van Vlierberghe S, Dubruel P, Möller L, Dräger G, et al. *Biomacromolecules* 2011; 12: 851-8.

[12] Ovsianikov A, Deiwick A, Van Vlierberghe S, Pflaum M, Wilhelmi M, Dubruel P, et al. *Materials* 2011; 4: 288-99.

[13] Ovsianikov A, Mühleder S, Torgersen J, Li Z, Qin X-H, Van Vlierberghe S, et al. *Langmuir* 2013; 30: 3787-94.

[14] Whitesides GM. *Nature* 2006; 442: 368-73.

[15] Chung BG, Lee K-H, Khademhosseini A, Lee S-H. *Lab Chip* 2012; 12: 45-59.

[16] Krutkramelis K, Xia B, Oakey J. *Lab Chip* 2016; 16: 1457-65.

[17] Siltanen C, Yaghoobi M, Haque A, You J, Lowen J, Soleimani M, et al. *Acta Biomater*. 2016; 34: 125-32.

[18] Leong J-Y, Lam W-H, Ho K-W, Voo W-P, Lee MF-X, Lim H-P, et al. *Particuology* 2016; 24: 44-60.

[19] Yang B, Lu Y, Luo G. *Ind. Eng. Chem. Res*. 2012; 51: 9016-22.

[20] Henke S, Leijten J, Kemna E, Neubauer M, Fery A, van den Berg A, et al. *Macromol. Biosci*. 2016; 16: 1524–32.

[21] Hancock MJ, Piraino F, Camci-Unal G, Rasponi M, Khademhosseini A. *Biomaterials* 2011; 32: 6493-504.

[22] Kamperman T, Henke S, van den Berg A, Shin SR, Tamayol A, Khademhosseini A, et al. *Adv. Healtc. Mater*. 2017; 6: 1600913.

[23] Kamperman T, Henke S, Visser CW, Karperien M, Leijten J. *Small* 2017; 13: 1603711.

[24] Min NG, Ku M, Yang J, Kim S-H. *Chem. Mater*. 2016; 28: 1430-8.

[25] Gong JP, Katsuyama Y, Kurokawa T, Osada Y. *Adv. Mater*. 2003; 15: 1155-8.

[26] Haque MA, Kurokawa T, Gong JP. *Polymer* 2012; 53: 1805-22.

[27] Li Z, Shen J, Ma H, Lu X, Shi M, Li N, et al. *Materials Science and Engineering: C* 2013; 33: 1951-7.

[28] Guo Y, Yuan T, Xiao Z, Tang P, Xiao Y, Fan Y, et al. *J. Mater. Sci: Mater. Med*. 2012; 23: 2267-79.

[29] Fallahi A, Khademhosseini A, Tamayol A. *Trends Biotechnol*. 2016; 34: 683-5.

[30] Tamayol A, Akbari M, Annabi N, Paul A, Khademhosseini A, Juncker D. *Biotechnol. Adv*. 2013; 31: 669-87.

[31] Moutos FT, Freed LE, Guilak F. *Nat. Mater*. 2007; 6: 162-7.

[32] Akbari M, Tamayol A, Bagherifard S, Serex L, Mostafalu P, Faramarzi N, et al. *Adv. Healtc. Mater*. 2016; 5: 751-66.

[33] Hwang CM, Khademhosseini A, Park Y, Sun K, Lee S-H. *Langmuir* 2008; 24: 6845-51.

[34] Majima T, Funakosi T, Iwasaki N, Yamane S-T, Harada K, Nonaka S, et al. *J. Orthop. Sci*. 2005; 10: 302-7.

[35] Horst M, Madduri S, Milleret V, Sulser T, Gobet R, Eberli D. *Biomaterials* 2013; 34: 1537-45.

[36] Lee KH, Shin SJ, Park Y, Lee S-H. *Small* 2009; 5: 1264-8.

[37] Subramanian A, Vu D, Larsen GF, Lin H-Y. *J. Biomater. Sci. Polym. Ed*. 2005; 16: 861-73.

[38] Lee BR, Lee KH, Kang E, Kim D-S, Lee S-H. *Biomicrofluidics* 2011; 5: 022208.

[39] Fan L, Du Y, Huang R, Wang Q, Wang X, Zhang L. *J. Appl. Polym. Sci*. 2005; 96: 1625-9.

[40] Kang E, Choi YY, Chae S-K, Moon J-H, Chang J-Y, Lee S-H. *Adv. Mater*. 2012; 24: 4271-7.

[41] Ghorbanian S, Qasaimeh MA, Akbari M, Tamayol A, Juncker D. *Biomed. Microdevices* 2014; 16: 387-95.

[42] Daniele MA, North SH, Naciri J, Howell PB, Foulger SH, Ligler FS, et al. *Adv. Funct. Mater*. 2013; 23: 698-704.

[43] Kang E, Jeong GS, Choi YY, Lee KH, Khademhosseini A, Lee S-H. *Nat. Mater*. 2011; 10: 877-83.

[44] Shi X, Ostrovidov S, Zhao Y, Liang X, Kasuya M, Kurihara K, et al. *Adv. Funct. Mater*. 2015; 25: 2250-9.

[45] Tamayol A, Najafabadi AH, Aliakbarian B, Arab-Tehrany E, Akbari M, Annabi N, et al. *Adv. Healtc. Mater*. 2015; 4: 2146-53.

[46] Wan ACA, Liao IC, Yim EKF, Leong KW. *Macromolecules* 2004; 37: 7019-25.

[47] Wan ACA, Leong MF, Toh JKC, Zheng Y, Ying JY. *Adv. Healtc. Mater*. 2012; 1: 101-5.

[48] Onoe H, Okitsu T, Itou A, Kato-Negishi M, Gojo R, Kiriya D, et al. *Nat. Mater*. 2013; 12: 584-90.

[49] Kim M, Hong B, Lee J, Kim SE, Kang SS, Kim YH, et al. *Biomacromolecules* 2012; 13: 2287-98.

[50] Akbari M, Tamayol A, Laforte V, Annabi N, Najafabadi AH, Khademhosseini A, et al. *Adv. Funct. Mater*. 2014; 24: 4060-7.

[51] Azagarsamy MA, Anseth KS. *Angew Chem., Int. Ed*. 2013; 52: 13803-7.

[52] DeForest CA, Anseth KS. *Angew Chem., Int. Ed*. 2012; 51: 1816-9.

[53] DeForest CA, Polizzotti BD, Anseth KS. *Nat. Mater*. 2009; 8: 659-64.

[54] DeForest CA, Tirrell DA. *Nat. Mater*. 2015; 14: 523-31.

[55] Gandavarapu NR, Azagarsamy MA, Anseth KS. *Adv. Mater*. 2014; 26: 2521-6.

[56] Engler AJ, Sen S, Sweeney HL, Discher DE. *Cell* 2006; 126: 677-89.

[57] Vicente-Manzanares M, Ma X, Adelstein RS, Horwitz AR. *Nat. Rev. Mol. Cell Biol*. 2009; 10: 778-90.

[58] Young JL, Engler AJ. *Biomaterials* 2011; 32: 1002-9.

[59] Nowatzki PJ, Franck C, Maskarinec SA, Ravichandran G, Tirrell DA. *Macromolecules* 2008; 41: 1839-45.

[60] Khetan S, Katz JS, Burdick JA. *Soft Matter* 2009; 5: 1601-6.

[61] Khetan S, Guvendiren M, Legant WR, Cohen DM, Chen CS, Burdick JA. *Nat. Mater*. 2013; 12: 458-65.

[62] Khetan S, Burdick JA. *Biomaterials* 2010; 31: 8228-34.

[63] Guvendiren M, Perepelyuk M, Wells RG, Burdick JA. *J. Mech. Behav. Biomed. Mater*. 2014; 38: 198-208.

[64] Guvendiren M, Burdick JA. *Nat. Commun*. 2012; 3: 792.

[65] Caliari SR, Perepelyuk M, Cosgrove BD, Tsai SJ, Lee GY, Mauck RL, et al. *Sci. Rep*. 2016; 6: 21387.

[66] Yang C, Tibbitt MW, Basta L, Anseth KS. *Nat. Mater*. 2014; 13: 645.

[67] Mabry KM, Lawrence RL, Anseth KS. *Biomaterials* 2015; 49: 47-56.

Bio / Medical

Materials / Systems

Energy / Environment

Research Highlights

KIST News

Up Close

Interview

[68] Tamate R, Ueki T, Kitazawa Y, Kuzunuki M, Watanabe M, Akimoto AM, et al. *Chem. Mater*. 2016; 28: 6401-8.

[69] Guven S, Chen P, Inci F, Tasoglu S, Erkmen B, Demirci U. *Trends Biotechnol*. 2015; 33: 269-79.

[70] Stephanopoulos N, Freeman R, North HA, Sur S, Jeong SJ, Tantakitti F, et al. *Nano Lett*. 2015; 15: 603-9.

[71] Shaw A, Lundin V, Petrova E, Fordos F, Benson E, Al-Amin A, et al. *Nat. Meth*. 2014; 11: 841-6.

[72] Markstedt K, Mantas A, Tournier I, Martínez Ávila H, Hägg D, Gatenholm P. *Biomacromolecules* 2015; 16: 1489-96.

[73] Deepthi S, Jeevitha K, Nivedhitha Sundaram M, Chennazhi KP, Jayakumar R. *Chem. Eng. J*. 2015; 260: 478-85.

[74] Carlos M, Serena D, Delfo DA, Luisa T, Claudio R, Dario P, et al. *Biofabrication* 2015; 7: 025005.

Bio / Medical

Materials / Systems

Energy / Environment

Research Highlights

KIST News

Up Close

Interview

Feature Articles

In Vivo Stem Cell Tracking with Imageable Nanoparticles that Bind Bioorthogonal Chemical Receptors on the Stem Cell Surface

Introduction

Kwang Meyung KIM

Principal Researcher
Center for Theragnosis
Biomedical Research Institute

kim@kist.re.kr

Recent research has investigated the pluripotency of stem cells and their capacity for self-renewal which has, in turn, stimulated interest in stem cell applications in both academic and clinical fields [1]. As a result of their pluripotent properties, stem cells could potentially be used to repair various organs and body systems, such as endocrine, joint, musculoskeletal and cardiovascular systems. Furthermore, they show considerable promise in adjuvant treatment for malignant tumors [2]. However, to ensure successful stem cell therapy after transplantation, it is essential to acquire precise information relating to the *in vivo* fate of stem cells, particularly as regards their biodistribution and functioning [3]. Although biopsy-based techniques have been used to monitor stem cells after transplantation, it is practically impossible to monitor all the transplanted cells because they spread over a wide range of tissue. Consequently, there is an urgent need to develop non-invasive stem cell imaging technology for monitoring the *in vivo* fate of transplanted stem cells. This article discusses KIST's efforts in developing a platform technology for tracking stem cells in a living body.

To address the challenge of stem cell tracking, we developed a new stem cell labeling and tracking technology using metabolic glycoengineering with bioorthogonal copper-free click chemistry [4]. First, we introduced targetable chemical receptors containing azide groups on stem cell surfaces via metabolic glycoengineering with precursors. We assessed three metabolic precursors: tetraacetylated N-azidoacetyl-mannosamine (A_{c4}MAnNAz), tetraacetylated N-azidoacetyl-galactosamine (A_{c4}GalNAz), and tetraacetylated N-azidoacetyl-glucosamine (A_{c4}GlcNAz) to select the optimal one with which to generate azide groups on the stem cell surface. Second, we prepared bicyclo[6.1.0]nonyne (BCN)-conjugated glycol chitosan nanoparticles (BCN-CNPs) with diverse imaging agents (Cy5.5, superparamagnetic iron oxide nanoparticles (SPIONs, gold nanoparticles) to label stem cells via bioorthogonal click chemistry between azide and BCN groups. These BCN-CNPs were specifically labeled to

the chemical reporters present on the stem cell surface and taken up into the stem cell via the cell membrane turnover mechanism. In addition, these labeled stem cells were successfully tracked non-invasively using *in vivo* imaging modalities, including fluorescence imaging, magnetic resonance (MR) imaging, and computed tomography (CT) imaging.

Results

Preparation of BCN-modified glycol chitosan nanoparticles (BCN-CNPs)

To label stem cells with diverse imaging agents, we prepared BCN-CNPs as template nanoparticles. They were prepared through the self-assembly of amphiphilic glycol chitosan, which was directly conjugated of 5β-cholanic acid and BCN molecules by formation of amide bond linkages (Figure 1a). For fluorescence, MR, and CT imaging, Cy5.5, SPIONs, and gold nanoparticles were introduced to the BCN-CNPs, respectively. BCN-CNP-Cy5.5, BCN-CNP-IRON, and BCN-CNP-GOLD manifested as spherical nanoparticles with average diameters of 314.0 ± 16.24 nm, 336.56 ± 14.64 nm, and 339.8 ± 26.26 nm, respectively (Figures 1b and 1c). The average diameters of all three types of nanoparticles showed no significant changes for up to 2 weeks under physiological conditions (PBS, pH 7.4, 37°C), indicating that all the imaging agent-encapsulated nanoparticles were highly stable in PBS (Figure 1d). Before *in vitro* and *in vivo* stem cell labeling and tracking, we performed fluorescence, MR, and CT phantom tests of BCN-CNP-Cy5.5, BCN-CNP-IRON, and BCN-CNP-GOLD, respectively, to assess their contrast effects. As shown in Figure 1e, BCN-CNP-Cy5.5, BCN-CNP-IRON, and BCN-CNP-GOLD showed a dose-dependent increase in fluorescence signals, T2-weighted MR signals, and higher X-ray absorption, respectively. Based on the *in vitro* phantom tests, all BCN-CNPs containing different imaging agents showed potential imaging signals in each imaging modality.
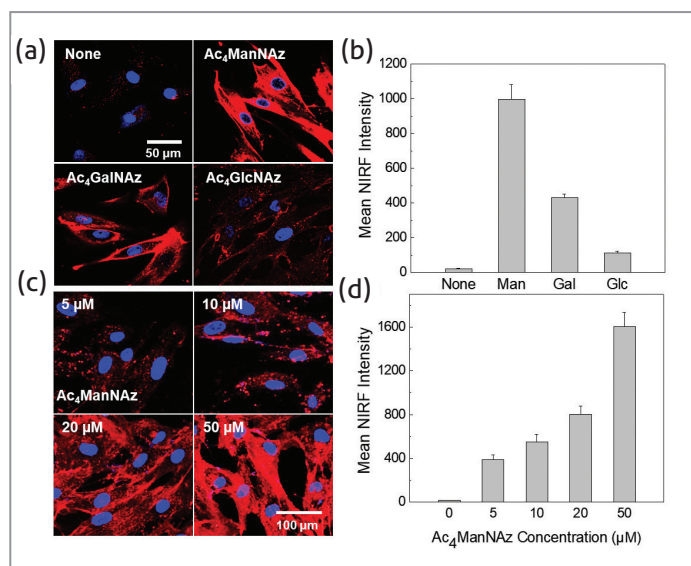
Generation of exogenous chemical receptors on the stem cell surface

In order to produce the exogenous chemical receptors of unnatural sialic acids containing azide (N_3) groups on the stem cell surface, human mesenchymal stem cells (hMSCs)
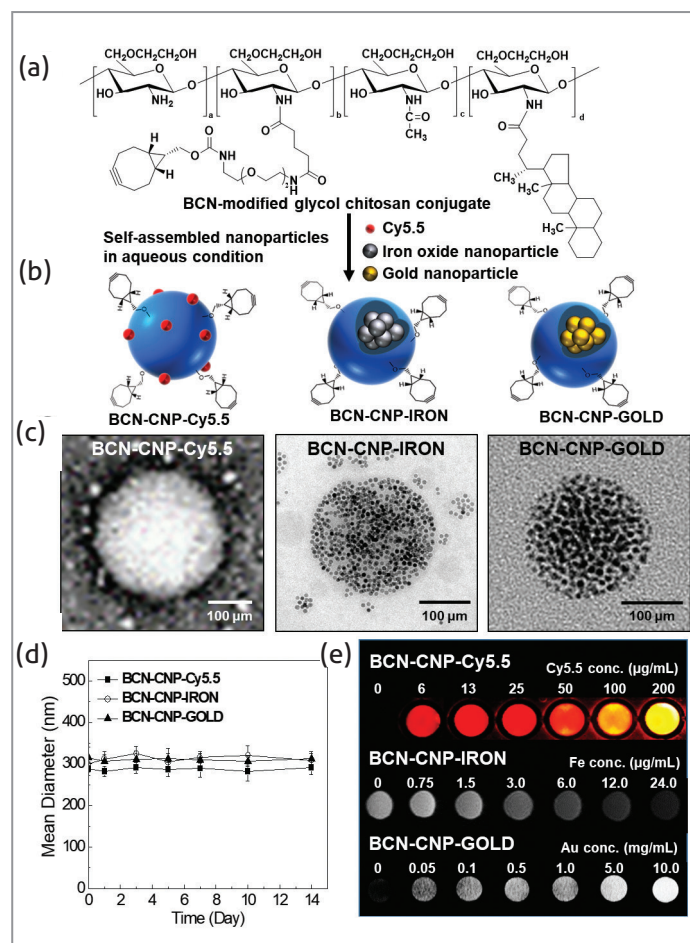
Figure 1 Preparation of BCN-CNPs containing diverse imaging agents for stem cell labeling and tracking. (a) Chemical structure of BCN-CNPs. (b) Schematic illustration of BCN-CNPs-Cy5.5, BCN-CNP-IRON, and BCN-CNP-GOLD. (c) The morphology of BCN-CNP-Cy5.5, BCN-CNP-IRON and BCN-CNP-GOLD. (d) Size stability of three BCN-CNPs in PBS (pH 7.4, 37°C) as a function of time. (e) NIRF, MR and CT phantom images of aqueous solutions containing BCN-CNP-Cy5.5, BCN-CNP-IRON and BCN-CNP-GOLD, respectively.

were treated with three metabolic precursors containing azide groups (A_{c4}MAnNAz, A_{c4}GalNAz and A_{c4}GlcNAz) that can be used as chemical counterparts of BCN molecules on CNPs for bioorthogonal copper-free click chemistry. As shown in Figures 2a and 2b the A_{c4}MAnNAz-treated hMSCs presented the strongest fluorescent signals when they were labeled with DBCO-Cy5.5 through the bioorthogonal copper-free click chemistry between azide groups on the stem cells and the cyclic alkyne groups of DBCO-Cy5.5. However, no signal was detected from the control hMSCs without any metabolic precursor treatment, indicating that the azide groups of unnatural sialic acids were exogenously introduced onto the stem cell surface. Based on these results, we selected A_{c4}MAnNAz as the metabolic precursor for further studies.
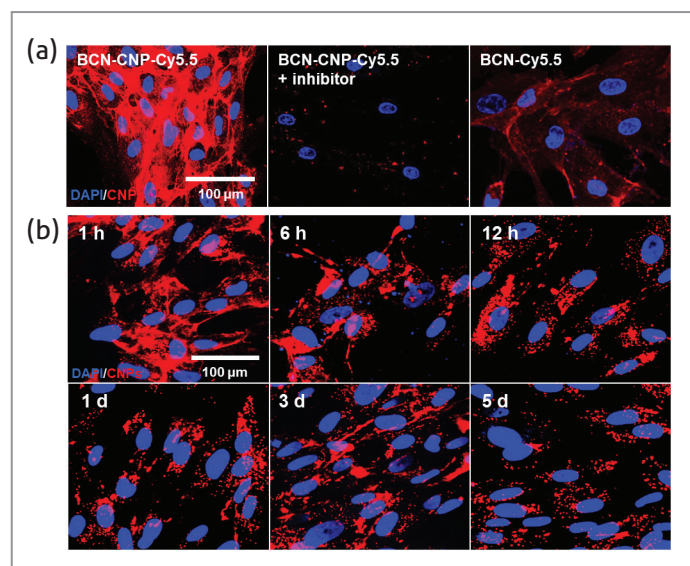
Figure 2   Generation of exogenous chemical receptors containing azide groups on the stem cell surfaces after treatment of three metabolic precursors. (a) Visualization of azide groups on the surfaces of hMSCs after treatment of three metabolic precursors. (b) Flow cytometry analysis of (a). (c) Comparative analysis of hMSC labeling on the dose of A_{c4}MAnNAz. Dose-dependent generation of azide groups on the hMSC surface after treatment with varying concentrations of A_{c4}MAnNAz (5, 10, 20 or 50 μM A_{c4}MAnNAz in media). (d) Flow cytometry analysis of (c).
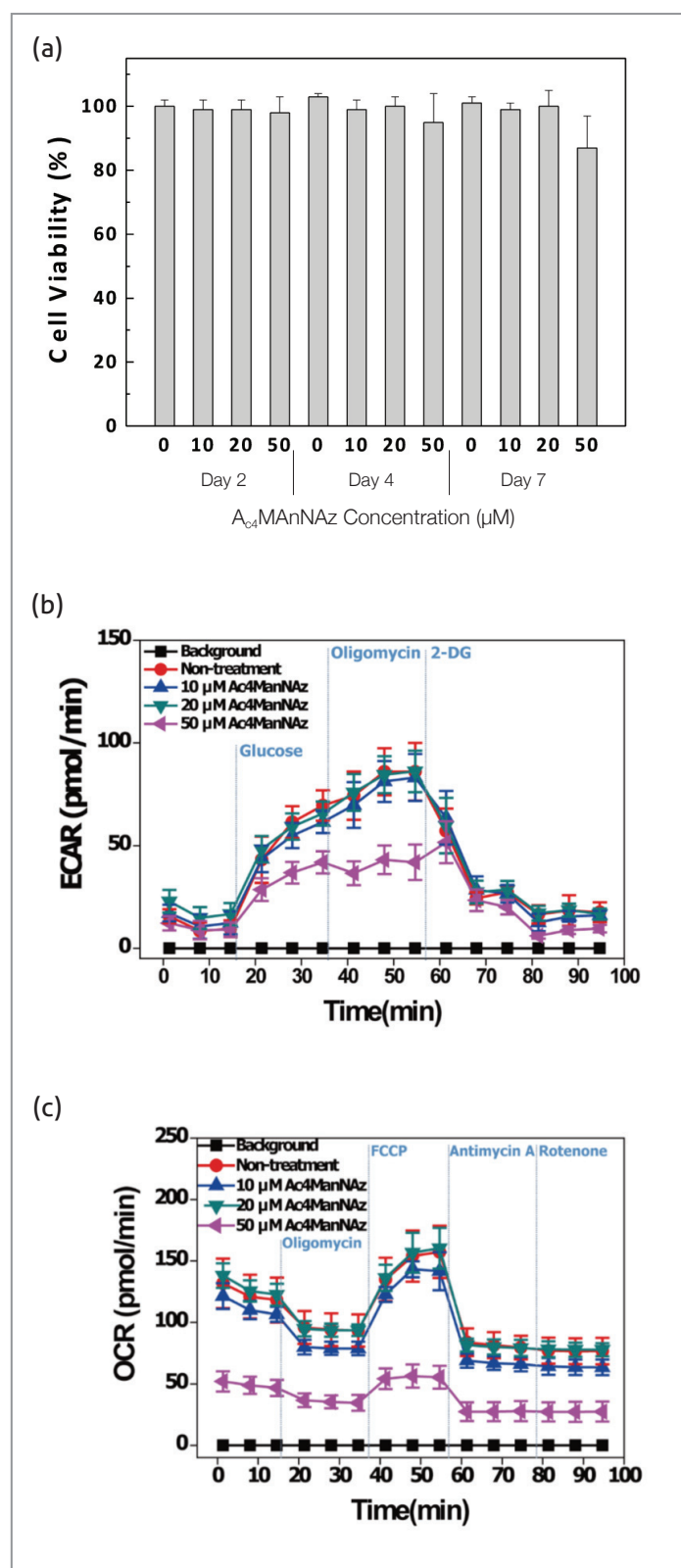

Figure 3   *In vitro* labeling and imaging of hMSCs. (a) Labeling of BCN-CNP-Cy5.5 to A_{c4}MAnNAz-treated hMSCs and control experiments with other group. (b) Time-lapse images of BCN-CNP-Cy5.5-labeled hMSCs, pretreated with A_{c4}MAnNAz, after growth for pre-determined time point.

One of the advantages of metabolic glycoengineering is that the number of chemical receptors on the cell surface can be carefully controlled by feeding different amounts of A_{c4}MAnNAz into the stem cell culture system. We found that when the concentration of A_{c4}MAnNAz increased from 5 to 50 μM in the hMSC culture media, the fluorescence intensity of DBCO-Cy5.5 (10 μM)-treated hMSCs increased proportionally in the confocal images and flow cytometry data, indicating that this chemical receptor targeting labeling method could control the number of chemical receptors on the stem cell surface in a dose-dependent manner (Figures 2c and 2d). This mechanism is completely different from that of biological receptors, which limits image labeling in other cells.

In vitro stem cell labeling and tracking

To demonstrate the potential advantage of the chemical receptor targeting labeling method described above, we carefully compared the cellular images of BCN-CNP-Cy5.5 to those of control hMSCs and A_{c4}MAnNAz-treated hMSCs pretreated with 10 μM of A_{c4}MAnNAz for 2 days. After 1 h post-incubation with BCN-CNP-Cy5.5 (200 μg/mL), the cellular binding efficiency of BCN-CNP-Cy5.5 to control stem cells decreased dramatically compared to that of 10 μM

of A_{c4}MAnNAz-treated hMSCs (Figure 3a).To confirm the efficiency of cell labeling and tracking of BCN-CNP-Cy5.5, we investigated the intracellular fate of these nanoparticles for up to 5 days in 10 μM of A_{c4}MAnNAz-treated hMSCs. After 1 h post-incubation with BCN-CNP-Cy5.5, the hMSCs were incubated in fresh media for up to 5 days, and the cellular uptake of BCN-CNP-Cy5.5 was observed using confocal microscopy (Figure 3b). After more than 6 h post-incubation, most particles were localized to the cytoplasm, indicating that the BCN-CNP-Cy5.5 on the stem cell surface was taken up rapidly via the cell membrane turnover mechanism [5]. Consequently, it was also notable that our labeling method using bioorthogonal copper-free click chemistry provided efficient and homogeneous labeling for each stem cell compared to the non-specific uptake of nanoparticles, which provided inefficient and heterogeneous labeling.

Toxicity analysis of metabolic glycoengineering

An ideal stem cell labeling and tracking method should be non-cytotoxic and not have harmful effects on the function of stem cells. Therefore, we determined the effect of metabolic glycoengineering on toxicity, proliferation, and differentiation potential of hMSCs. Firstly, the standard cell viability assay showed no decrease in the relative viabilities of A_{c4}MAnNAz-treated hMSCs at concentrations up to 50 μM of A_{c4}MAnNAz

Bio / Medical

Materials / Systems

Energy / Environment

Research Highlights

KIST News

Up Close

Interview

Figure 4 Toxicity of metabolic glycoengineering to hMSCs. (a) Cell viability of hMSCs at 2, 4, 7 days after treatment with A_{c4}MAnNAz. (b) ECAR data from the XP96 analyzer of the control and A_{c4}MAnNAz-treated hMSCs. (c) OCR data from the XP96 analyzer of the control and A_{c4}MAnNAz-treated hMSCs.

for 2, 4, and 7 days (Figure 4a). However, in the case of 50 μM A_{c4}MAnNAz-treated hMSCs, we observed that the cell viability significantly decreased at day 7 after treatment with A_{c4}MAnNAz. To further examine potential cellular toxicity and damage to A_{c4}MAnNAz-treated hMSCs, we also carefully analyzed the extracellular acidification rate (ECAR), which measures the oxygen consumption rate (OCR) to indicate cell damage (Figures 4b and 4c). ECAR data did not change in any of the treatment methods except in the 50 μM of A_{c4}MAnNAz-treated stem cells. However, the OCR data of 50 μM of A_{c4}MAnNAz-treated hMSCs dramatically decreased compared to the control stem cells and low-dose (10–20 μM) A_{c4}MAnNAz-treated stem cells, indicating the high-dose A_{c4}MAnNAz-treated hMSCs were substantially damaged. Based on the ECAR and OCR measurements, the optimum concentration of A_{c4}MAnNAz for metabolic glycoengineering of hMSCs was confirmed to be 10–20 μM.

In vivo imaging of stem cells after transplantation

In order to evaluate stem cell imaging efficacy *in vivo*, BCN-CNP-Cy5.5-labeled hMSCs (1×10^6 cells) both with and without A_{c4}MAnNAz treatment were transplanted into the dorsal subcutaneous region of nude mice. As expected, the NIRF intensity of A_{c4}MAnNAz-treated hMSCs was about 15-fold higher than those of the hMSCs that had not been treated with A_{c4}MAnNAz for 15 days (Figure 5a). The NIRF signal of hMSCs labeled without A_{c4}MAnNAz treatment was not detected beyond 5 days post-transplantation. Our *in vivo* imaging data thus clearly presents a potential method for *in vivo* stem cell tracking over a prolonged time in a living animal.

In addition to optical imaging, many researchers have focused on MR or CT imaging for longitudinal stem cell monitoring of specific tissue locations in humans because these technologies are capable of deep penetration and high spatial resolution. To extend the chemical receptor targeting imaging method, we tested the imaging efficiency of BCN-CNPs containing iron oxide nanoparticles (BCN-CNP-IRON) or gold nanoparticles (BCN-CNP-GOLD) in live animals. BCN-CNP-IRON-labeled hMSCs (1×10^6 cells) or BCN-CNP-GOLD-labeled hMSCs (1×10^7 cells), both with and without A_{c4}MAnNAz pretreatment, were subcutaneously transplanted into the dorsal sides of nude mice, which were then imaged under a 9.4T micro MRI scanner and micro CT (mCT) scanner, respectively, 1 day after transplantation. In the MR images, a noticeable darkening effect in the T2-weighted MR image
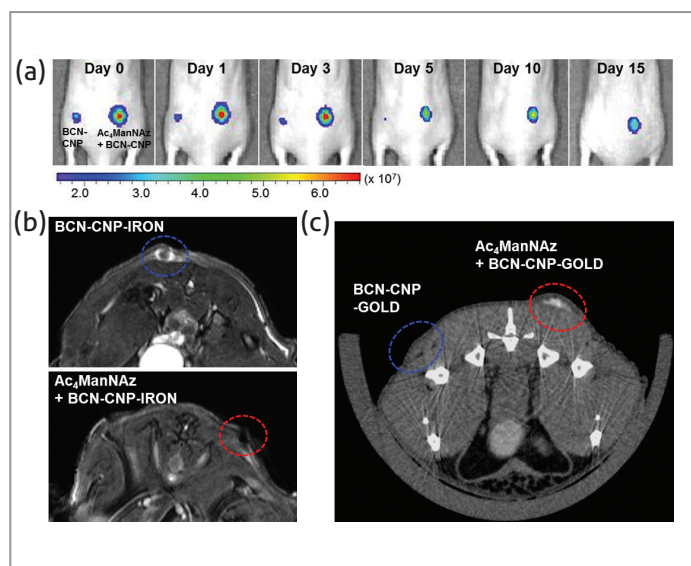
Figure 5   *In vivo* imaging of labeled hMSCs. (a) NIRF images of mice after subcutaneous transplantation of BCN-CNP-Cy5.5- labeled hMSCs with/without $Ac_4MAnNAz$ pretreatment. (b) T2-weighted MR image of mice injected with BCN-CNP-IRON-labeled hMSCs without pretreatment (blue dot) and with pretreatment of $Ac_4MAnNAz$ (red dot). (c) mCT image of mice injected with BCN-CNP-GOLD-labeled hMSCs without pretreatment (blue dot) and with pretreatment of $Ac_4MAnNAz$ (red dot).

(red dotted circle) was clearly observed at the transplantation site (Figure 5b). The T2-weighted MR signal of $Ac_4MAnNAz$-treated stem cells was 5.4-fold higher than that of stem cells labeled without $Ac_4MAnNAz$ pretreatment (blue dotted circle). In the case of mCT images obtained 1 day after transplantation, the bright spots (red dotted circle) of stem cells were clearly identifiable at the transplanted site. A 2.5-fold higher mCT signal was measured in comparison to stem cells labeled without $Ac_4MAnNAz$ pretreatment (blue dotted circle), which were not detectable in mCT images (Figure 5c). These results indicate that both BCN-CNP-IRON- and BCN-CNP-GOLD-labeled hMSCs can be well visualized in MR and mCT imaging *in vivo* due to the higher labeling efficiency of our chemical receptor targeting method compared to non-specific nanoparticle uptake. The success of our method in non-invasively tracking stem cells through MR and mCT imaging is a demonstration of its promising potential for clinical applications in human subjects as well.

Conclusions

Our studies provide proof-of-concept results for the potential of a novel stem cell labeling and tracking technology using metabolic glycoengineering and bioorthogonal click chemistry. Exogenous chemical receptors containing azide groups were successfully incorporated on $Ac_4MAnNAz$-treated stem cell surfaces via metabolic glycoengineering. These azide groups were then specifically labeled with bicyclo[6.1.0] nonyne (BCN)-conjugated glycol chitosan nanoparticles (BCN-CNPs) encapsulating different imaging agents: Cy5.5, superparamagnetic iron oxide nanoparticles and gold nanoparticles. No negative effects on stem cell functioning were observed after applying this labeling technology, as evidenced by the cells' continuing viability, proliferation, and differentiation ability during cell culture. BCN-CNP-labeled stem cells exhibited high contrast at the transplanted site in mice after the transplantation of stem cells, resulting in efficient cell tracking for up to 15 days. Furthermore, these stem cells could be tracked using fluorescence, MR, and CT imaging when labeled with BCN-CNP-Cy5.5, BCN-CNP-IRON, or BCN-CNP-GOLD, respectively. We conclude that our stem cell labeling and tracking technology has excellent potential as a new stem cell imaging technology for the non-invasive tracking of transplanted stem cells and represents a viable method for stably labeling stem cells with various imageable nanoparticles.

Note

This article and images are drawn from "*In vivo* stem cell tracking with imageable nanoparticles that bind bioorthogonal chemical receptors on the stem cell surface" in *Biomaterials*, 2017; Vol. 139: 12-29.

References

[1] Xin T, Greco V, Myung P. *Cell* 2016; 164 (6): 1212-25.

[2] Dazzi F, Horwood NJ. *Curr. Opin. Oncol*. 2007; 19 (6): 650-5.

[3] Kurtz A. *International Journal of Stem Cells* 2008; 1 (1): 1-7.

[4] Sletten EM, Bertozzi CR. *Acc. Chem. Res*. 2011; 44 (9): 666-676.

[5] Tettamanti G. *Glycoconj J*. 2004; 20 (5): 301-17.

Bio / Medical

Materials / Systems

Energy / Environment

Research Highlights

KIST News

Up Close

Interview

Serial Changes in 3-Dimensional Supraspinatus Muscle Volume After Rotator Cuff Repair

Young Jun KIM

Principal Researcher
Center for Bionics
Biomedical Research
Institute

junekim@kist.re.kr

Background:

There is considerable debate on the recovery of rotator cuff muscle atrophy after rotator cuff repair.

Purpose:

To evaluate the serial changes in supraspinatus muscle volume after rotator cuff repair by using semiautomatic segmentation software and to determine the relationship with functional outcomes.

**Study Design:**

Case series; Level of evidence, 4.

Methods:

74 patients (mean age, 62.8 ± 8.8 years) who had undergone arthroscopic rotator cuff repair were included in the study. Magnetic resonance imaging (MRI) scans showing complete Y-views and taken at three distinct times (preoperatively, immediately postoperatively, and ≥1 year postoperatively) were obtained for each patient. We generated a 3-dimensional (3D) reconstructed model of the supraspinatus muscle by using in-house semiautomatic segmentation software (ITK-SNAP) and calculated both the 2-dimensional (2D) cross-sectional area and 3D volume of the muscle in three different views (Y-view, 1 cm medial to the Y-view [Y + 1 cm] and 2 cm medial to the Y-view [Y + 2 cm]) at the three different time points. The area and volume changes at each time point were evaluated according to repair integrity. Later postoperative volumes were compared with volumes found immediately postoperatively. The relationships of these volumes with various clinical factors were investigated as well as the effect of higher volumes on range of motion, muscle strength, visual analog scale pain and the scoring system used by the American Shoulder and Elbow Surgeons.
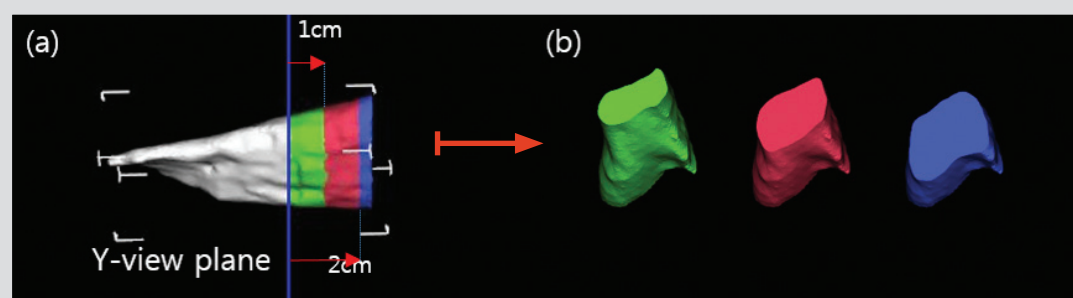
(a) Definition of the Y-view and clipped planes
(b) Clipped models to measure the volume and cross-sectional area of supraspinatus
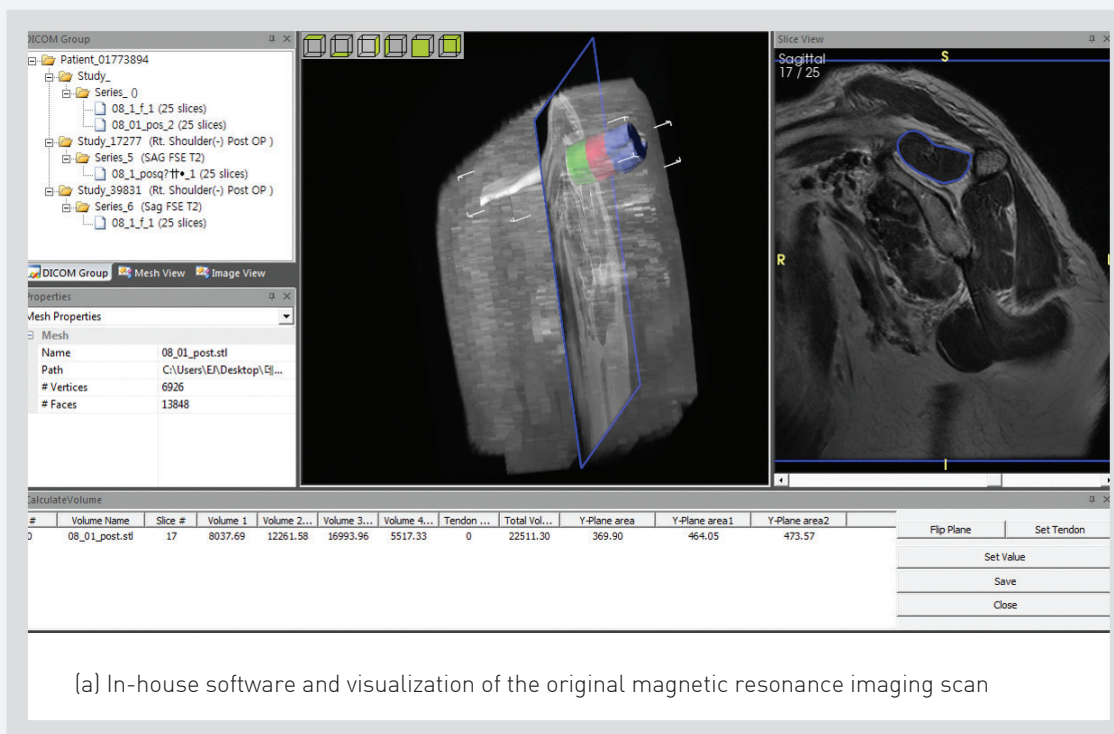
(a) In-house software and visualization of the original magnetic resonance imaging scan

Results:

The interrater reliabilities were excellent for all measurements. Areas and volumes increased in the immediate postoperative scans as compared with the preoperative views; however, only volumes on the Y + 1 cm views and Y + 2 cm views significantly increased in the later postoperative period compared with immediately postoperatively (P < .05). Nine patients had healing failure; area and volume changes were significantly less in the later postoperative scans compared with the immediate postoperative scans in these patients at all measurement points (P < .05). After omitting results from these patients, volume increases in the later postoperative scans became more prominent (P < .05) in the following order: Y + 2 cm view, Y + 1 cm view, and Y-view. Volume increases were higher in patients with larger tears who healed successfully (P = .040). Higher volume increases were associated only with an increase in abduction power (P = .029) and not with other outcomes

Conclusion:

The supraspinatus muscle volume increased immediately postoperatively and continuously for at least 1 year after surgery. The increase was evident in patients who had larger tears and healed successfully and when measured toward the more medial portion of the supraspinatus muscle. The volume increases were associated with an increase in shoulder abduction power.

Bio / Medical

Materials / Systems

Energy / Environment

Research Highlights

KIST News

Up Close

Interview

Technical Review

Metallic MXene Saturable Absorber for Femtosecond Mode-Locked Lasers

Young Min JHON

Principal Researcher
Sensor System Research Center
National Agenda Research Division

ymjhon@kist.re.kr

Introduction

Since the invention of the laser, nonlinear optics has been one of the most rapidly growing scientific fields, particularly over the last few decades. Nonlinear optics describes the interaction of light with matter in the regime where the response of materials to the applied electromagnetic field becomes nonlinear in a strong field like lasers. This nonlinearity gives rise to many interesting optical phenomena, including frequency mixing processes such as second harmonic generation, Kerr effects, optical rectification, saturable absorption, and so forth. There is a strong consensus that the discovery of promising nonlinear optical materials will play a pivotal role in the evolution of future optics with a significant impact on both fundamental research and industrial applications. In materials with saturable absorption, the absorption of light decreases with an increasing light intensity. After the early use of dyes as saturable absorbers (SAs) to produce high-peak-power and/or ultra-short laser pulses via passive Q-switching and/or mode locking, semiconductor saturable absorber mirrors were developed and became prevalent materials in SA research for a long time. One of the most valuable products enabled by SAs is the femtosecond laser, which is used in precise micromachining, molecular spectroscopy and high-speed information processing. Researchers have started to pay particular attention to nanomaterials for the development of novel SAs.

Recently, a new group of 2D materials known as MXenes, which are 2D transition metal carbides, nitrides, and carbonitrides, has attracted much interest due to the various outstanding properties of these materials. However, the potential of MXenes in laser optics has not yet been explored. We suggest that MXenes should exhibit interesting nonlinear performance, and particularly due to their excellent electronic mobility and/or relaxation, MXenes should play a critical role in ultra-fast intensity-dependent optical switching.
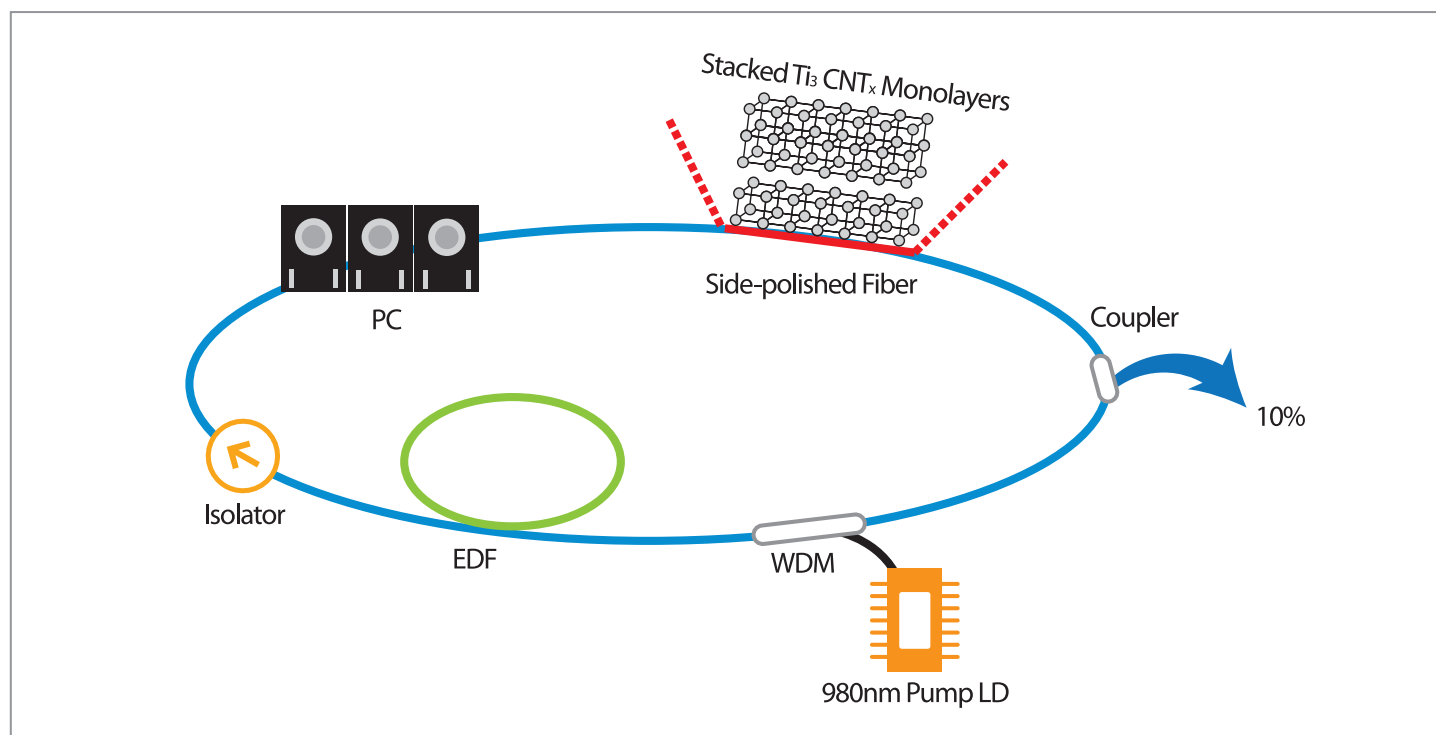
Figure 1 Schematic of the ring-cavity erbium-doped fiber laser incorporating stacked Ti3CNTx SAs. Here, PC, EDF, WDM, and LD denote a polarization controller, an Er-doped fiber, wavelength division multiplexing, and a laser diode, respectively.

Results and discussion

Our research has demonstrated for the first time that MXenes (specifically Ti_3CN) can serve as an ultra-fast mode-locker that produces femtosecond laser pulses, suggesting the great potential of MXenes in many other nonlinear applications as well [1]. Stable laser pulses with a duration as short as 660 fs are readily obtained at a repetition rate of 15.4 MHz and a wavelength of 1557 nm. Density functional theory calculations show that 2D structural and electronic characteristics are well conserved in their stacked form due to the unique interlayer coupling in MXenes. The calculations also suggest the promise of MXenes in broadband saturable absorber applications due to their metallic characteristics, which is absent in other 2D SAs reported so far to be operative for mode locking. This was confirmed by our experiments of Q-switched lasers based on MXenes at wavelengths of 1558 and 1875 nm.

Work carried out by another research group on the basis of our findings validated our arguments even more decisively by showing that MXenes provide ~159 fs pulse lasers via optimization and exhibit a negative nonlinear refractive index to an extent comparable to graphene [2].

We expect that our study will provide a valuable blueprint and basis for the development of nanomaterial-based nonlinear optics while opening a new avenue for the development of advanced nonlinear photonic devices based on MXenes.

Note

This article and images are drawn from "Metallic MXene saturable absorber for Femtosecond mode-locked lasers" in *Advanced Materials,* 2017; Vol. 29: 40.

References

[1] Jhon YI, Koo JH, Anasori B, Seo MA, Lee JH, Gogotsi Y, Jhon YM. *Adv. Mater*. 2017; 29: 1702496.
[2] Jiang X, Liu S, Liang W, Luo S, He Z, Ge Y, Wang H, Cao R, Zhang F, Wen Q, Li J, Bao Q, Fan D, Zhang H. *Laser Photonics Rev*. 2017; 12: 1700229.

Bio / Medical Materials / Systems Energy / Environment Research Highlights KIST News Up Close Interview

Feature Articles

Online Hydrogen/Deuterium Exchange of Gas-Phase Molecules by Electrospray Ionization Mass Spectrometry Coupled with Gas Chromatography

Jae Ick LEE

Principal Researcher
Doping Control Center
Research Planning &
Coordination Division

jaeicklee@kist.re.kr

Introduction

Hydrogen/deuterium (H/D) exchange mass spectrometry (MS) is a widely used technique for identifying metabolites [1] or pharmaceutical impurities [2] in drug discovery and development processes. H/D exchange MS can be implemented in various ways with the most popular being to infuse a pure compound prepared in a deuterated solvent [1]. However, this method requires a process to separate and purify the target analyte from the sample. Meanwhile, an online H/D exchange MS method, which can directly analyze a sample, has also been reported. This method can be implemented using both on-column and post-column techniques. On-column H/D exchange MS has been performed with a deuterated solvent as a mobile phase in liquid chromatography-mass spectrometry (LC-MS) [1, 3]. However, this method suffers from high consumption of an expensive deuterated solvent, such as D_2O, and shifts in chromatographic retention times due to the different mobile phase-analyte-stationary phase interactions caused when two different mobile phases, such as H_2O and D_2O, are used. The post-column H/D exchange method has been performed by mixing LC-eluted analytes with a D_2O solvent using a tee union. In this method, the D_2O solvent is infused using a syringe pump, and H/D exchange occurs after column separation; thus, it does not cause a chromatographic retention time shift [4]. However, in this method, the use of H_2O as an LC mobile phase can give rise to back-exchange, thus resulting in poor H/D exchange efficiency.

Recently, gas chromatography-electrospray ionization tandem mass spectrometry (GC-ESI-MS/MS), combining both the excellent chromatographic resolving power of GC and the soft ionization of ESI, has been reported [5]. Our group has also shown that steroids such as trimethylsilyl derivatives can be analyzed using GC-ESI/MS with high separation efficiency and enhanced selectivity and sensitivity [6]. Despite such advantages, the GC-ESI/MS setup is not yet commercially available. In this study, we first performed in-ESI-source H/D exchange using a GC-ESI/MS configuration to identify the unknown compounds and reduce

the consumption of expensive deuterated reagents. With this configuration, simultaneous H/D exchange MS of multi-target analytes in conjunction with GC is enabled with minimal use of a deuterated solvent.

Results and discussion

Optimization of in-ESI-source H/D exchange

The configuration of GC-ESI/MS and an overview of the H/D exchange of the gas-phase molecule in the ESI source are shown in Figure 1. The experimental parameters for online in-ESI-source H/D exchange coupled with GC-ESI/MS were optimized using propylhexedrine with a secondary amine as a representative analyte among the 11 target analytes of interest.
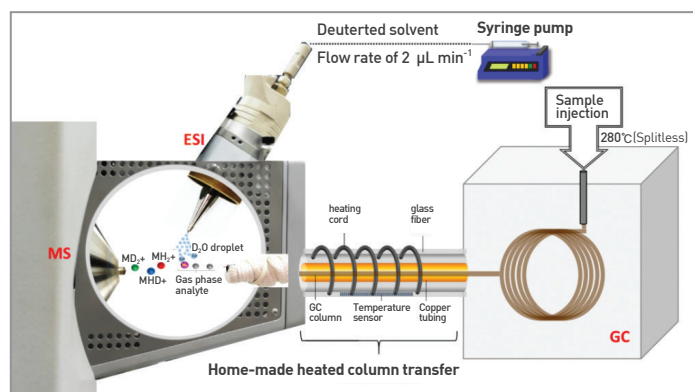
Figure 1   Overview of the H/D exchange of the gas-phase molecule using GC-ESI/MS.
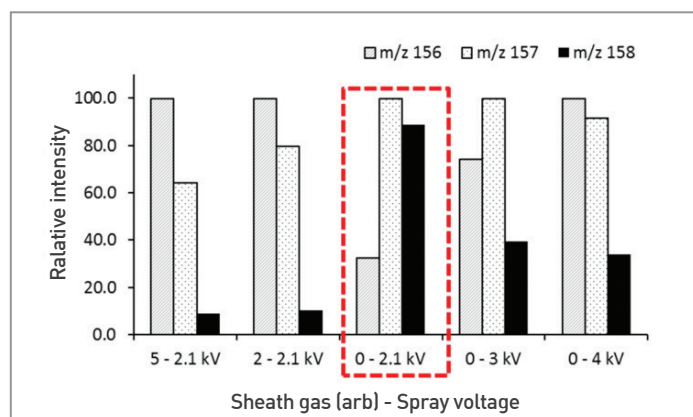
Figure 2   Degree of H/D exchange for propylhexedrine according to spray voltage and sheath gas flow rate in GC-ESI/MS: The D_2O:acetonitrile (50:50, v/v) solution with 0.1% formic acid as spray solvent was used at a flow rate of 2 μL min^{-1} without sheath gas.

It was found that the degree of H/D exchange depends on three experimental parameters: spray potential, sheath gas flow rate, and the temperature of the desolvating capillary. First, the spray potential was tuned in the range of +2.1 to +4.0 kV, with the sheath gas flow rate set to a fixed value. Below a spray potential of +2.1 kV, it was difficult to acquire stable mass spectral signals. As shown in Figure 2, the degree of H/D exchange was the highest at a spray potential of +2.1 kV and zero sheath gas flow. As the spray potential was increased, the degree of H/D exchange decreased accordingly. Specifically, the relative abundances of the peaks at m/z 156, 157, and 158 were 32.6, 100, and 88.7, respectively, at a spray potential of +2.1 kV and changed to 74.3, 100, and 39.4 at +3.0 kV and 100, 91.9, and 34.1 at +4.0 kV. Second, the sheath gas flow rate was varied from 0 to 5 (arbitrary units) at a spray potential of +2.1 kV. As the sheath gas flow rate increased from 0 to 5, the degree of H/D exchange dramatically decreased. Thus, in the following online H/D exchange experiments coupled with GC-ESI/MS, a spray potential of +2.1 kV and no sheath gas were used, although there was some loss of chromatographic peak shape due to the absence of sheath gas. In GC-ESI/MS, the ionization occurs by ion evaporation after a dissolution process of the gas-phase analyte into the charged droplet or by a gas-phase proton transfer reaction between protonated solvent and analyte. In this study, the ionization mechanism is likely to be ion evaporation rather than a gas-phase proton transfer reaction. This ionization mechanism is also supported by the fact that sheath gas and a high spray potential decrease the exchange yield. In other words, the gaseous molecules from the GC capillary might be dissolved into the charged H_2O or D_2O droplet and then protonated (or deuterated) before the formation of single ions according to the ESI mechanism. Third, the temperature of the desolvating capillary was tuned in the range 150°C–350°C at a spray potential of +2.1 kV without sheath gas. The relative abundances of the MD_2+ ion (m/z 158) were 68.6% at 150°C, 96.4% at 200°C, 95.1% at 250°C, 94.1% at 300°C, and 91.7% at 350°C. The H/D exchange efficiency was relatively low at 150°C but not significantly different at 200°C or higher. However, because the source dissociation of some stimulants increased at higher temperatures, 200°C was used as the temperature for the desolvating capillary in this study.

The H/D exchange efficiency for a spray solvent in GC-ESI/MS was investigated using D_2O:CH_3CN (50:50, v/v) solutions with various modifiers, based on the experiments by Shah et al. [4]. The relative abundances of the MD_2+ ions of stimulants, except fenetylline, were the highest in 0.1% formic

Bio / Medical

Materials / Systems

Energy / Environment

Research Highlights

KIST News

Up Close

Interview

Table 1   Relative abundances of the fully exchanged MD$_2$+ ion according to the spray solvents in GC-ESI/MS.

Compound	MD$_2$+	Modifier of spray solvent				
		Formic acid	Ammonium formate	Ammonium acetate	Ammonia	Pure
Isometheptene	m/z 144	80.0	50.9	38.4	36.3	75.0
Propylhexedrine	m/z 158	96.4	51.8	45.5	32.6	62.0
Methoxyphenamine	m/z 182	76.2	53.9	33.7	27.0	61.1
Methylephedrine	m/z 182	33.7	20.2	19.7	33.6	31.5
Mefenorex	m/z 214	90.0	52.3	51.7	66.2	71.9
Fencamfamine	m/z 218	75.0	47.2	41.5	42.1	51.0
Cyclazodone	m/z 219	39.6	9.8	16.8	16.1	6.1
Etamivan	m/z 226	3.2	1.9	2.1	2.9	5.0
Fenfluramine	m/z 234	76.5	30.4	31.0	43.8	60.7
Clobenxorex	m/z 262	78.6	61.1	61.6	84.7	67.9
Fenetylline	m/z 344	50.6	45.2	46.5	100.0	30.4

acid solution (e.g., 96.4% for propylhexedrine), followed by a pure solution (62.0%), a 10 mM ammonium formate solution (51.8%), a 10 mM ammonium acetate solution (45.5%), and a 0.1% NH3 solution (32.6%). For fenetylline, the relative abundance of the MD$_2$+ ion was the highest at 100% in 0.1% NH$_3$ solution. This was sufficient to observe the MD$_2$+ ion in the mass spectrum of the 0.1% formic acid solution. The fully exchanged MD$_2$+ ion for etamivan was not produced under any of these conditions. Therefore, the D$_2$O solution with 0.1% formic acid as the spray solvent was used for simultaneous H/D exchange of stimulants. The relative abundances of the MD$_2$+ ions of stimulants according to spray solvents are summarized in Table 1.

Figure 3a shows a representative chromatogram acquired with D$_2$O as a spray solvent. For comparison, a
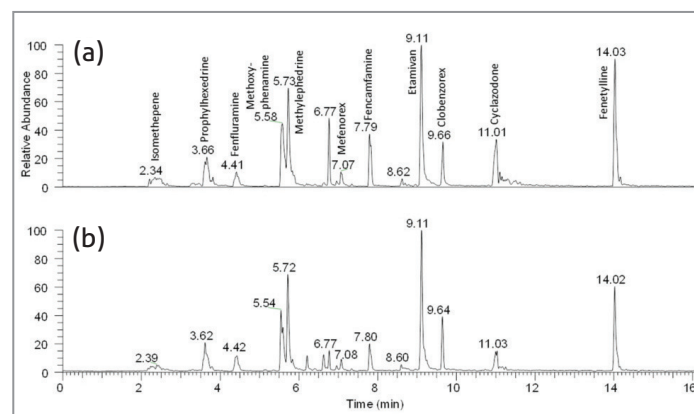
Figure 3   Total ion GC-ESI/MS chromatograms obtained using (a) D$_2$O and (b) H$_2$O as the spray solvents.

chromatogram acquired with H$_2$O spray solvent is shown in Figure 3b. In both experiments, H$_2$O:CH$_3$CN or D$_2$O:CH$_3$CN (50:50, v/v) solution with 0.1% formic acid was used as a spray solvent, which is infused at a flow rate of 2 μL min-1. Comparison of these two chromatograms clearly indicates that the retention times of the 11 stimulants acquired using the D$_2$O solvent (Figure 3a) are almost identical to those acquired using H$_2$O as a solvent (Figure 3b). As the retention times of the current experiments are related solely to the gas-chromatographic retention times of the analytes, the identical retention times of the unexchanged and deuterated stimulants could be readily understood.

Table 2 summarizes the corrected relative abundances of the H/D-exchanged ions and the %D levels for the 11 stimulants. The %D levels of the stimulants were in the range 31.0%–60.8%, except for etamivan. In etamivan, an acidic phenolic OH group is exchanged, contrary to the other compounds. Methylephedrine and fenetylline contain a further basic center, where protonation may occur besides the exchanged OH or NH group as a reason for low exchange, which could explain the lower exchange yields. The H/D exchange efficiency of amines and alcohol can be reduced at low pH. However, the H/D efficiencies of methylephedrine and etamivan were not improved by spray solvents with neutral or basic pH. The observed %D levels for the –NH or –OH functional group in the stimulants were generally lower than those reported by Wolff et al. (32%–90%) [7] but similar to those reported by Tolonen et al. (44%–59%) [8], where H/D exchanges were performed in solution. This result strongly

Table 2 Corrected relative abundances and deuterium incorporation (%D) levels by GC-ESI/MS-based H/D exchange for stimulants.

Compound	Structure	MW	RT(min)	Corrected relative abundances			%D
				MH$_2$+	MHD+	MD$_2$+	
Isometheptene		141	2.34	33.2	96.6	70.0	59.2
Propylhexedrine		155	3.66	38.0	95.6	85.5	60.8
Methoxyphenamine		179	5.58	51.4	93.6	64.5	53.1
Methylephedrine		179	5.73	100.0	75.1	24.3	31.0
Mefenorex		211	7.07	37.1	95.0	65.0	57.1
Fencamfamine		215	7.79	52.1	91.2	59.6	51.8
Cyclazodone		216	11.01	59.9	91.7	26.8	40.7
Etamivan		223	9.11	100.0	10.3	1.8	6.2
Fenfluramine		231	4.41	38.5	94.8	63.4	56.3
Clobenxorex		259	9.66	70.0	87.5	39.5	42.2
Fenetylline		341	14.03	71.0	84.6	32.3	39.7

suggests that the present experimental configuration for online in-ESI-source H/D exchange coupled with GC-ESI/MS is also suitable for simultaneous H/D exchange of multi-target analytes.

Comparison of in-ESI-source and solution H/D exchange

The H/D exchange efficiency of the in-ESI-source H/D exchange method coupled with GC-ESI/MS was compared with that of the solution H/D exchange method. The solution H/D exchange was performed by directly infusing H/D-exchanged stimulants prepared in D_2O/H_2O/acetonitrile solutions containing 0.1% formic acid with varying percentages of D_2O: 100%, 83.3%, 71.4%, 50%, 33.3%, and 20% D_2O in aqueous solution. The relative abundances of MD$_2$+ obtained by the in-ESI-source and solution H/D exchange methods are summarized in Table 3. All relative abundances of the MD$_2$+ ions are corrected by

considering the isotopic contributions of the naturally occurring heavy isotopes. The relative abundances of MD$_2$+ from the in-ESI-source H/D exchange method were generally lower than those from the solution H/D exchange method for 100%, 83.3%, and 71.4% D_2O but higher for those with 50%, 33.3%, and 20% D_2O. In the case of methylephedrine, etamivan, and cyclazodone, the solution H/D exchange was limited. The relatively low H/D exchange efficiency of the in-ESI-source exchange method is presumably due to the limited exchange time of in-ESI-source H/D exchange [9].

Structural elucidation using deuterated MS/MS spectrum

MS/MS of deuterated compounds can provide valuable information for interpreting fragmentation pathways and further elucidating structures based on fragment ions whose mass values

Table 3   Relative abundances corrected by considering the naturally occurring heavy isotopes for the fully exchanged MD$_2$+ ion according to percentage D$_2$O in direct-infusion MS analysis in comparison to GC-ESI/MS

Compound	MD$_2$+	GC-ESI/MS	Percentage D$_2$O					
			100%	83.3%	71.4%	50%	33.3%	20%
Isometheptene	m/z 144	70.0	98.8	95.6	92.2	42.9	26.6	10.6
Propylhexedrine	m/z 158	85.5	99.1	95.6	91.7	42.2	25.8	9.8
Methoxyphenamine	m/z 182	64.5	98.1	94.8	90.2	45.0	25.9	9.6
Methylephedrine	m/z 182	24.3	23.0	20.5	16.9	8.5	5.4	2.1
Mefenorex	m/z 214	65.0	95.0	89.5	80.2	37.3	23.6	7.2
Fencamfamine	m/z 218	59.6	98.4	93.1	87.6	39.4	23.9	9.4
Cyclazodone	m/z 219	26.8	4.2	8.0	4.2	2.7	6.7	1.9
Etamivan	m/z 226	1.8	2.7	6.5	3.4	2.1	2.0	2.0
Fenfluramine	m/z 234	63.4	98.2	93.7	89.8	46.3	23.8	8.7
Clobenxorex	m/z 262	39.5	65.6	50.1	34.1	15.3	15.4	3.9
Fenetylline	m/z 344	32.3	27.1	21.9	15.1	8.1	9.3	4.8
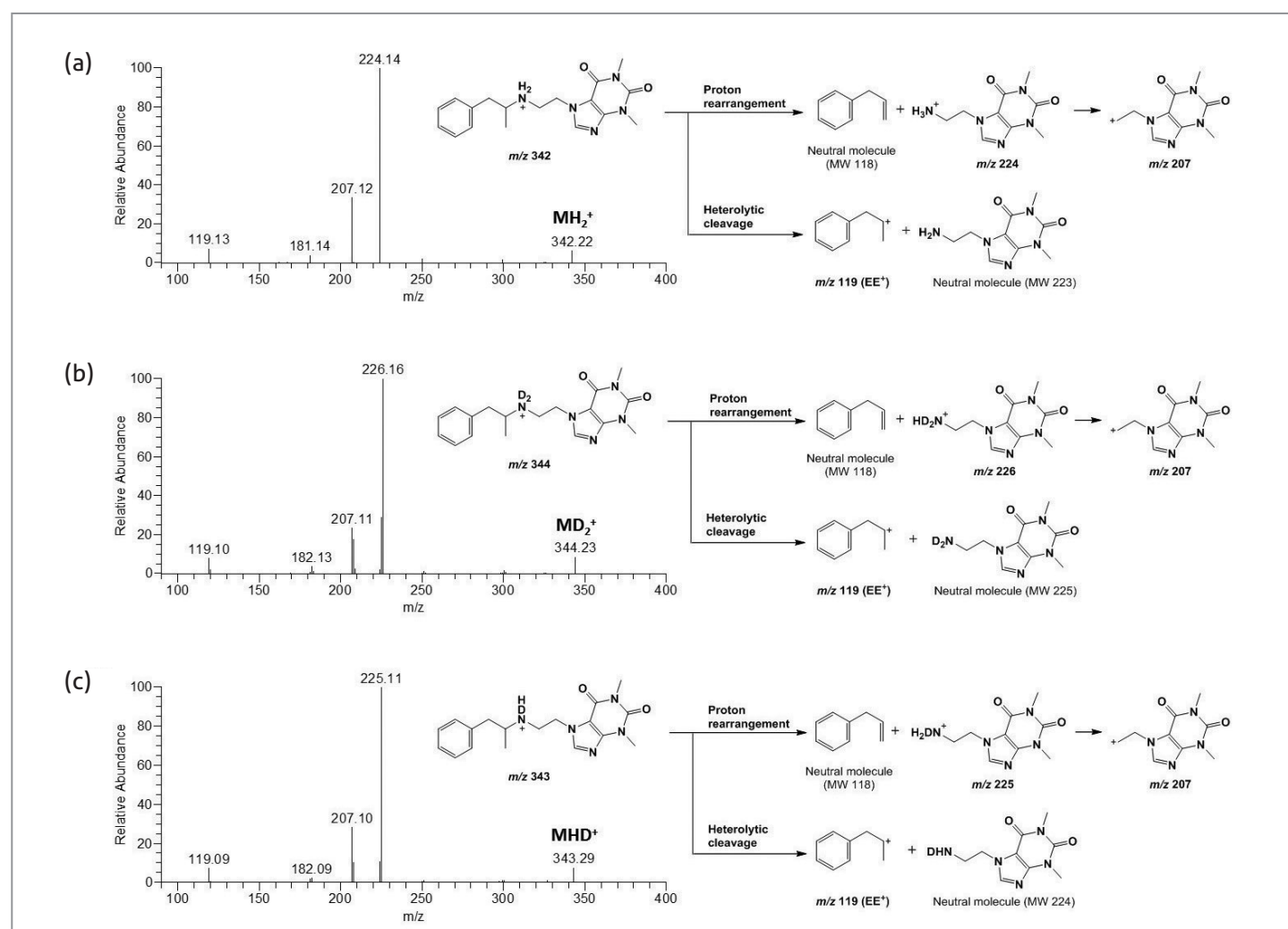
Figure 4   Product ion spectra and fragmentation pathways of (a) unexchanged MH$_2$+, (b) fully exchanged MD$_2$+, and (c) partially exchanged MHD+ ions of fenetylline obtained by GC-ESI/MS-based H/D exchange.

are affected by deuterium inclusion. Thus, collision-induced dissociation (CID) spectra were obtained for the H/D-exchanged stimulant ions. For example, Figure 4 shows the CID spectra of unexchanged (MH$_2$+), partially exchanged (MHD+), and fully exchanged (MD$_2$+) fenetylline ions generated by online in-ESI-source H/D exchange in GC-ESI/MS. For fenetylline, it is likely that a proton resides on the secondary nitrogen, due to its high proton affinity. The protonated fenetylline (*m/z* 342) can undergo unimolecular dissociation upon collisional activation via two fragmentation pathways (right-hand side of Figure 4a). First, heterolytic cleavage between the protonated nitrogen and the adjacent carbon gave rise to an even-electron cation (EE+) at *m/z* 119 and a neutral molecule of 223 Da. Alternatively, hydrogen rearrangement (H-shift) can accompany heterolytic cleavage, producing EE+ at *m/z* 224 and a neutral molecule of 118 Da. The produced EE+ at *m/z* 224 can further experience NH3 loss to give rise to a fragment at *m/z* 207. The suggested fragmentation pathways are consistent with the CID spectra of the fully and partially exchanged fenetylline ions. In particular, the production of the two fragment peaks at *m/z* 226 and 207 in the CID spectrum of MD$_2$+ supports the protonation site at the secondary nitrogen and the heterolytic bond cleavages occurring between the protonated nitrogen and adjacent carbons (Figure 4b). The suggested fragmentation pathways adequately explain why the mass shift occurred only with the fragment peak at *m/z* 224 (→ *m/z* 226) and not for that at *m/z* 207. The CID mass spectrum for the partially exchanged fenetylline ion (Figure 4c) is also consistent with the suggested fragmentation pathways, showing the mass shift of the fragment at *m/z* 224 to *m/z* 225 and no mass shift of the fragment at *m/z* 207, which indicates the loss of NDH$_2$.

Conclusions

Herein, simultaneous H/D exchange using GC-ESI/MS was newly investigated and optimized. The GC-ESI/MS-based H/D exchange method was applied to the 11 stimulants with secondary amino or hydroxyl groups. In this method, the H/D exchange for gas-phase stimulants occurred in the ESI source. The in-ESI-source H/D exchange efficiency obtained by GC-ESI/MS was relatively lower than those obtained by solution H/D exchange but was sufficient to determine the number of hydrogen by the interpretation of the fragmentation mechanism for the product ion spectrum. The online H/D exchange by GC-ESI/MS has the disadvantage of being restricted to small

volatile molecules due to the limitations of GC. However, the proposed method offers advantages such as low consumption of deuterated solvent, simultaneous H/D exchange of multi-target analytes, and direct analysis of samples without the purification of interesting peaks.

Note

This article and images are reprinted with permission from the article "Online Simultaneous Hydrogen/Deuterium Exchange of Multitarget Gas-Phase Molecules by Electrospray Ionization Mass Spectrometry Coupled with Gas Chromatography" in *Analytical Chemistry*, 2017; Vol. 89: 12284-12292. Copyright (2017) American Chemical Society.

References

[1] Lafaille F, Banaigs B, Inguimbert N, Enjalbal C, Doulain PE, Bonnet PA, Masquefa C, Bressolle FM. *Anal. Chem*. 2012; 84: 9865–9872.

[2] Ruggenthaler M, Grass J, Schuh W, Huber CG, Reischl RJ. *J. Pharm. Biomed. Anal*. 2017; 135: 140–152.

[3] Olsen MA, Cummings PG, Kennedy-Gabb S, Wagner BM, Nicol GR, Munson B. *Anal. Chem*. 2000; 72: 5070–5078.

[4] Shah RP, Garg A, Putlur SP, Wagh S, Kumar V, Rao V, Singh S, Mandlekar S, Desikan S. *Anal. Chem*. 2013; 85: 10904–10912.

[5] Brenner N, Haapala M, Vuorensola K, Kostiainen R. *Anal. Chem*. 2008; 80: 8334–8339.

[6] Cha E, Jeong ES, Cha S, Lee J. *Anal. Chim. Acta* 2017; 964: 123–133.

[7] Wolff JC, Laures AM. *Rapid Commun. Mass Spectrom*. 2006; 20: 3769–3779.

[8] Tolonen A, Turpeinen M, Uusitalo J, Pelkonen O. *Eur. J. Pharm. Sci*. 2005; 25: 155–162.

[9] Lam W, Ramanathan R. *J. Am. Soc. Mass Spectrom*. 2002; 13: 345–353.

Structural Evolution of LixNiyMnzCo1-y-zO2 Cathode Materials During High-Rate Charge and Discharge

Won Young CHANG

Principal Researcher
Center for Energy Storage
Research
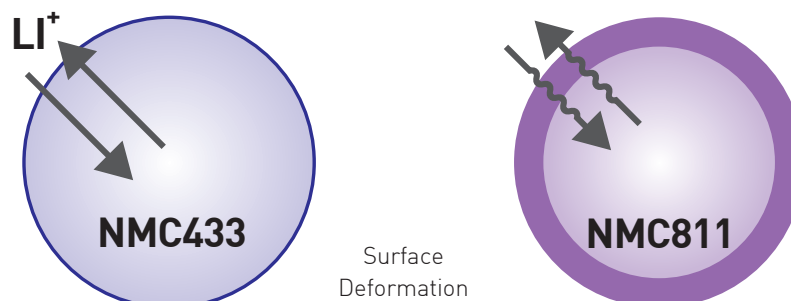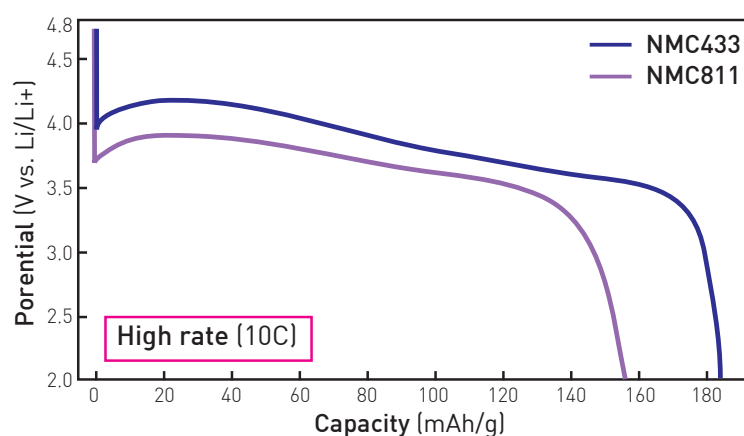Green City Technology Institute

cwy@kist.re.kr

Seung Min KIM

Principal Researcher
Carbon Composite Materials
Research Center
KIST Jeonbuk Institute of
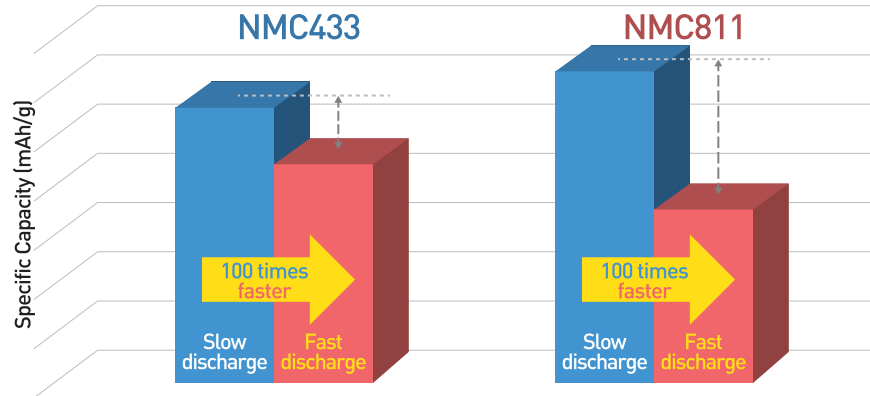Advanced Composite Materials

seungmin.kim@kist.re.kr

Ni-rich lithium transition metal oxides have received significant attention due to their high capacities and rate capabilities determined via theoretical calculations. Although the structural properties of these materials are strongly correlated with the electrochemical performance, their structural stability during the high-rate electrochemical reactions has not been fully evaluated yet. In this work, transmission electron microscopy is used to investigate the crystallographic and electronic structural modifications of Ni-based cathode materials at a high charge/discharge rate of 10 C. It is found that the high-rate electrochemical reactions induce structural inhomogeneity near the surface of Ni-rich cathode materials, which limits Li transport and reduces their capacities. This study establishes a correlation between the high-rate electrochemical performance of the Ni-based materials and their structural evolution, which can provide profound insights for designing novel cathode materials having both high energy and power densities.

Bio / Medical

Materials / Systems

Energy / Environment

Research Highlights

KIST News

Up Close

Interview

NMC433 and NMC811 after a discharge at a rate of 10C from 4.8V. Circles with the dotted line denotes the contribution from the spinel structure in case of mixed phase. L and S denote layered and spinel structures.
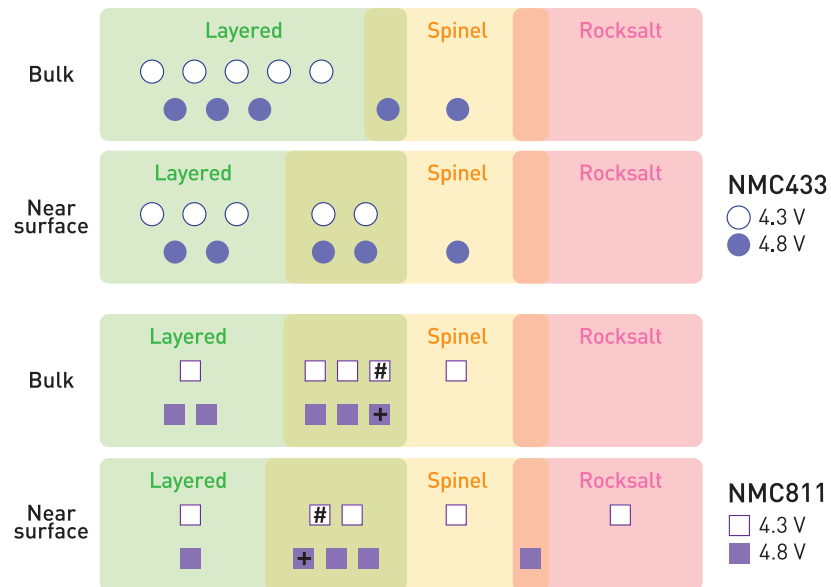
NMC811 particles after high-rate discharge from 4.3 or 4.8 V to 2V. Signs of + and # are used to indicate the identical particles in bulk and near the surface, respectively.

Technical Review

Preparation, Characterization, and Application of TiO₂-Patterned Polyimide Film as a Photocatalyst for Oxidation of Organic Contaminants

Seok Won HONG

Principal Researcher
Center for Water Resource Cycle Research
Green City Technology Institute

swhong@kist.re.kr

A Seom SON

Research Trainee
Center for Water Resource Cycle Research
Green City Technology Institute

sonaseom@kist.re.kr

Introduction

In recent decades, the pollution of water sources has been increasing due to inadequate treatment technologies and a growing number of contaminants, particularly micropollutants from pharmaceuticals, pesticides and endocrine disrupters. Researchers are now looking at various advanced oxidation processes to treat these pollutants and are working extensively on approaches involving heterogeneous photocatalysis with titanium dioxide (TiO_2). Immobilization of TiO_2 on substrates has been recognized as a potential methodology for enabling continuous and cost-effective uses of photocatalysts [1]. For water treatment applications, certain techniques have been commonly employed to deposit catalysts on substrates such as glass, polymer and metal [2], but recently, electrohydrodynamic processes (e.g., electrospinning and electrospraying) have attracted attention as more advantageous low-energy and cost effective material processing methods. As our previous studies have revealed, these techniques offer the advantages of high deposition efficiency and easy control of film thickness during the fabrication of TiO_2 nanoparticles (NPs) on polymer mat and polymer-coated steel mesh [3, 4].

In our first attempt, a self-cleaning photocatalytic paper was fabricated from hybrid poly(vinylidene fluoride)-TiO_2 nanofiber mats using a combination of electrospinning and electrospraying (Figure 1). The resultant photocatalytic papers were effective in degrading selected refractory emerging contaminants (bisphenol A, 4-chlorophenol and cimetidine), which dissolved in both deionized water and secondary wastewater effluents. However, the release of organic matter during prolonged photocatalytic tryout restricted its applicability on an industrial scale.
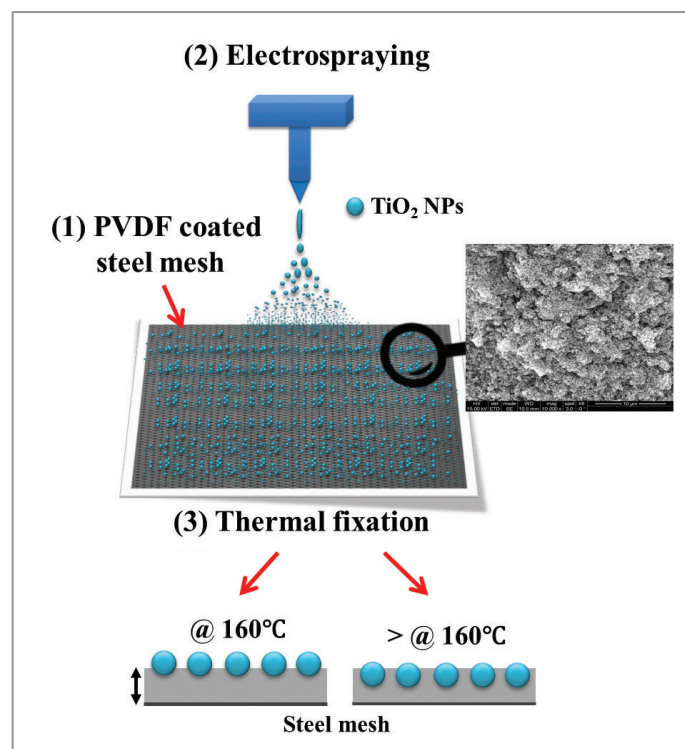
As a result, we made an effort to increase the mechanical stability and reusability of TiO_2 photocatalyst by immobilizing TiO_2 NPs on steel mesh through poly(vinylidene fluoride) coating, electrospray and thermal fixation techniques (Figure 2). As results revealed,
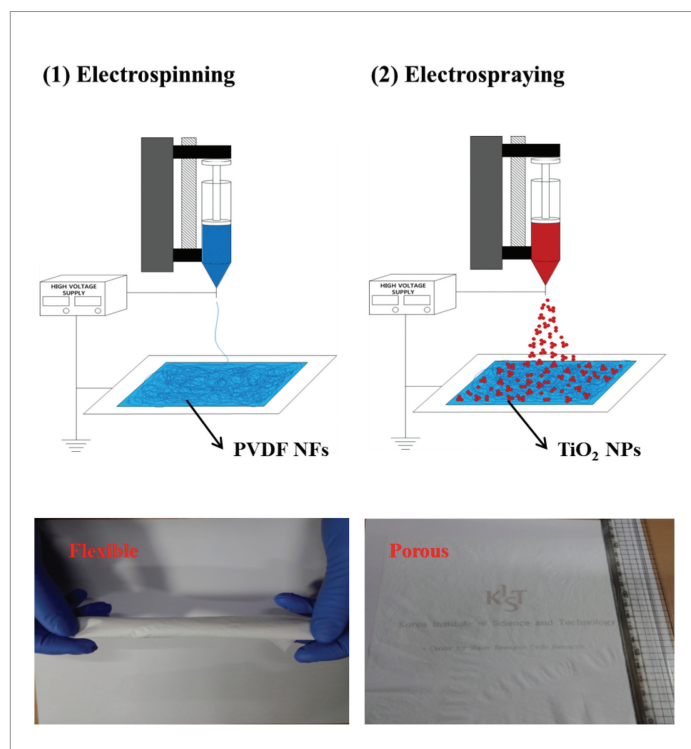
Figure 1 Fabrication of photocatalytic paper (PVDF–TiO$_2$ hybrids) via electrospinning and electrospraying (adapted from Ramasundaram et al. [3]).

Figure 2 Schematic of experimental procedure for fabricating immobilized TiO$_2$ on polymer-coated steel mesh (adapted from Ramasundaram et al. [4]).

the immobilized TiO$_2$ NPs (SM-TiO$_2$) exhibited good performance in the photooxidization of organic dyes and other pollutants in UV light. Unlike photocatalytic paper, the SM-TiO$_2$ has morphological advantages, high catalytic efficacy, good reusability and broad application potential. In general, our previous efforts demonstrated the possibility of a simple and easy scalable fabrication route for polymer-inorganic semiconductor photocatalyst for the removal of diverse organic pollutants. Nevertheless, cost effectiveness and stability against photocatalysis remained an open question. In this regard, oxidation-resistant polymer would be preferable as a photocatalyst substrate.

Polyimide (PI) is a representative polymer which has been widely used in electronics, aerospace, membrane fabrication, and other applications because of its excellent mechanical, thermal, electrical, and oxidation-resistant properties [5]. The aromaticity and electron-deficient imide bonds of PI structure lead to good stability against oxidization. Furthermore, in PI-TiO$_2$ coatings and composites, strong Ti-O-C and Ti-C bonds are known to exist in the interfacial region between TiO$_2$ and PI [6].

In this article, we discuss our attempt to fabricate a reliable, stable and cost effective photocatalyst via the thermal transfer patterning (TTP) method. The synthesis parameters, such as TiO$_2$ loading, surface chemical composition and hot press conditions for TTP, were optimized for the photocatalytic activity of PI-TiO$_2$.The photocatalytic efficacies were evaluated against dye (methylene blue, MB), herbicide (atrazine, ATZ), germicide (4-chloropheonl, 4-CP), and antibiotic (amoxicillin, AMX) compounds. Furthermore, the changes in toxicity or antibiotic activity of the selected compounds during photocatalysis, acute toxicity and bacterial regrowth potential of PI-TiO$_2$ treated samples were also measured using *Vibrio fischeri* and *Escherichia coli (E. coli)*.

Results and discussion

Fabrication
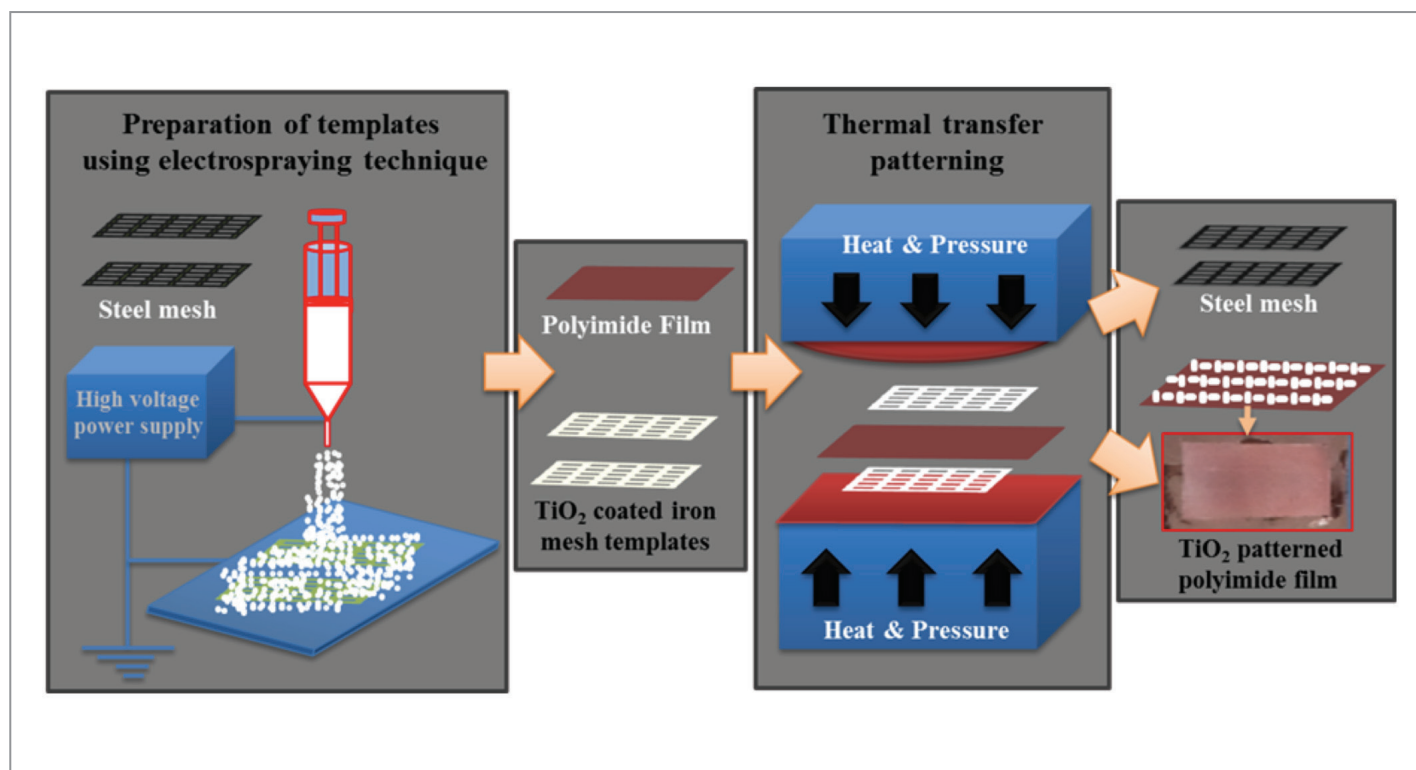
Figure 3 illustrates the overall preparation process

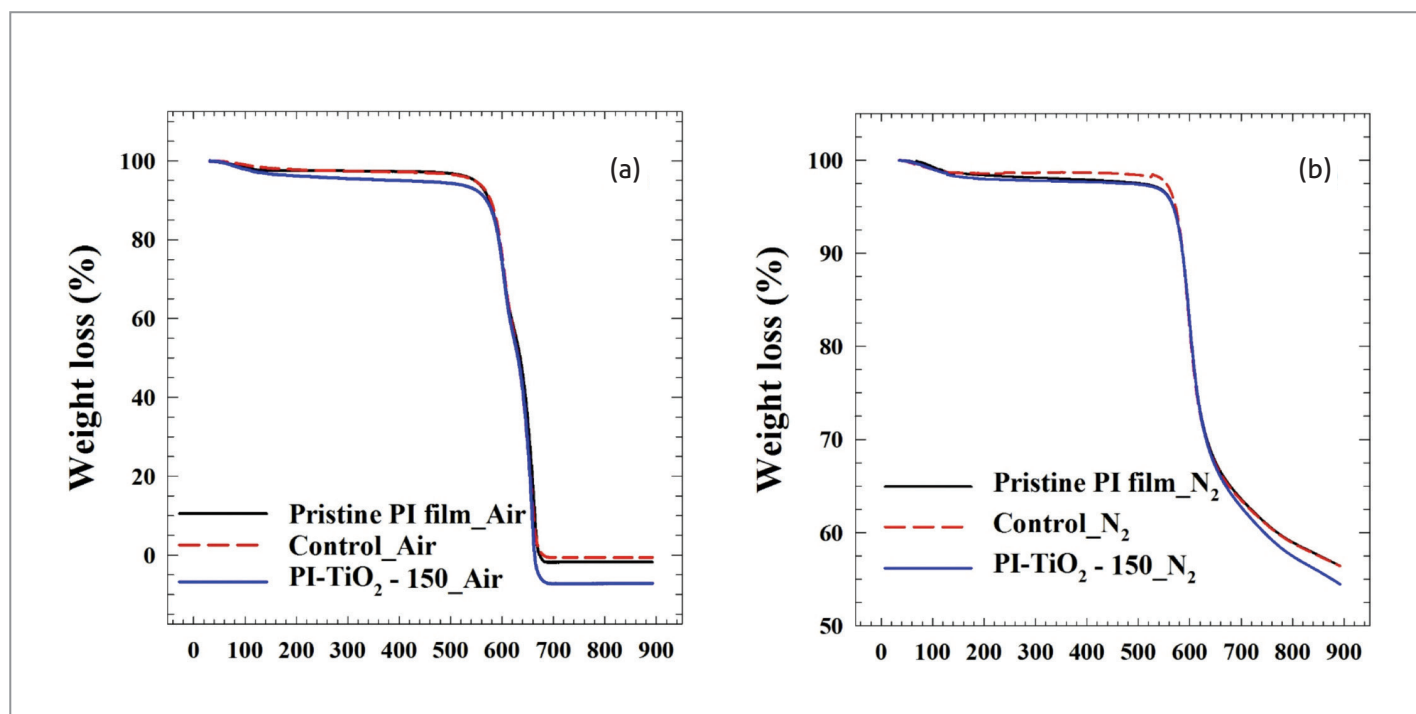**Figure 3**   Schematic of experimental procedure for fabricating TiO$_2$-patterned polyimide film.

Figure 4   Thermograms of pristine PI, substrate control and PI-TiO$_2$-150 recorded at (a) air and (b) N$_2$ atmospheres (scan rate = 10 °C/min).

for PI-TiO$_2$. A TiO$_2$ dispersion (P25) of 1 mg/ml was prepared by sonicating P25 powder with methanol at 40 kHz for 1h. This dispersion was electrosprayed on two pieces of 10×10 cm cleaned steel mesh (with a thickness of 244.4 μm) using a Nano NC electrospinning/electrospraying system. The distance between the electrospraying nozzle and collector was 12 cm. The 21G needle with an inner diameter of 514 μm was used as a nozzle. The flow rate and the applied voltage were 0.5 ml/ min and 20 kV, respectively. The 10×10 cm pristine PI (PPI) film was placed in between the two steel mesh templates. At that moment, the P25-coated side of template faced the PI film. This assembly was placed in a hot press and heated to 350°C and then subjected to a pressure of 100 MPa for 20 min. Later after cooling, PI-TiO$_2$ and the templates were easily separated by hand. To remove any loosely immobilized TiO$_2$, as-prepared PI-TiO$_2$ samples were washed with running tap water, rinsed with deionized (D. I.) water and dried at 60°C for 5 h. The substrate control (SC) was fabricated under identical conditions, but only templates electrosprayed with methanol (without TiO$_2$) were used. PI-TiO$_2$ samples were coded as PI-TiO$_2$-X, where X = the volume of P25 dispersion electrosprayed on the steel mesh.

Characterization

Optimization of hot press conditions for TTP

According to TGA thermographs in air, thermal degradation temperature (Td), the point of 5% weight loss, was 546°C for PPI and SC, and 402°C for PI-TiO$_2$-150 (Figure 4). For all samples, the onset weight loss occurred around 568°C. In N$_2$, the Td of PPI and PI-TiO$_2$- 150 was 568°C, while that of SC was 5°C higher due to structural stabilization which occurred during TTP. Contrary to the case of air, a considerable amount of residue remained in N$_2$ (PI-TiO$_2$-150: 54.5%; PPI and SC: 56.5%). In N$_2$, PI-TiO$_2$-150 showed a 2% higher weight loss below Td and 2% less residue than the others. This was due to catalytic oxidation of PI matrix by TiO$_2$ as observed in TiO$_2$ incorporated polymer materials [7] at elevated temperatures. Nevertheless, in the presence of TiO$_2$, the PI matrix was found to be stable at 350°C for 20 mins in air and N$_2$. Therefore, the maximum TTP working conditions were maintained at 350°C, 100 Mpa and 20 min.
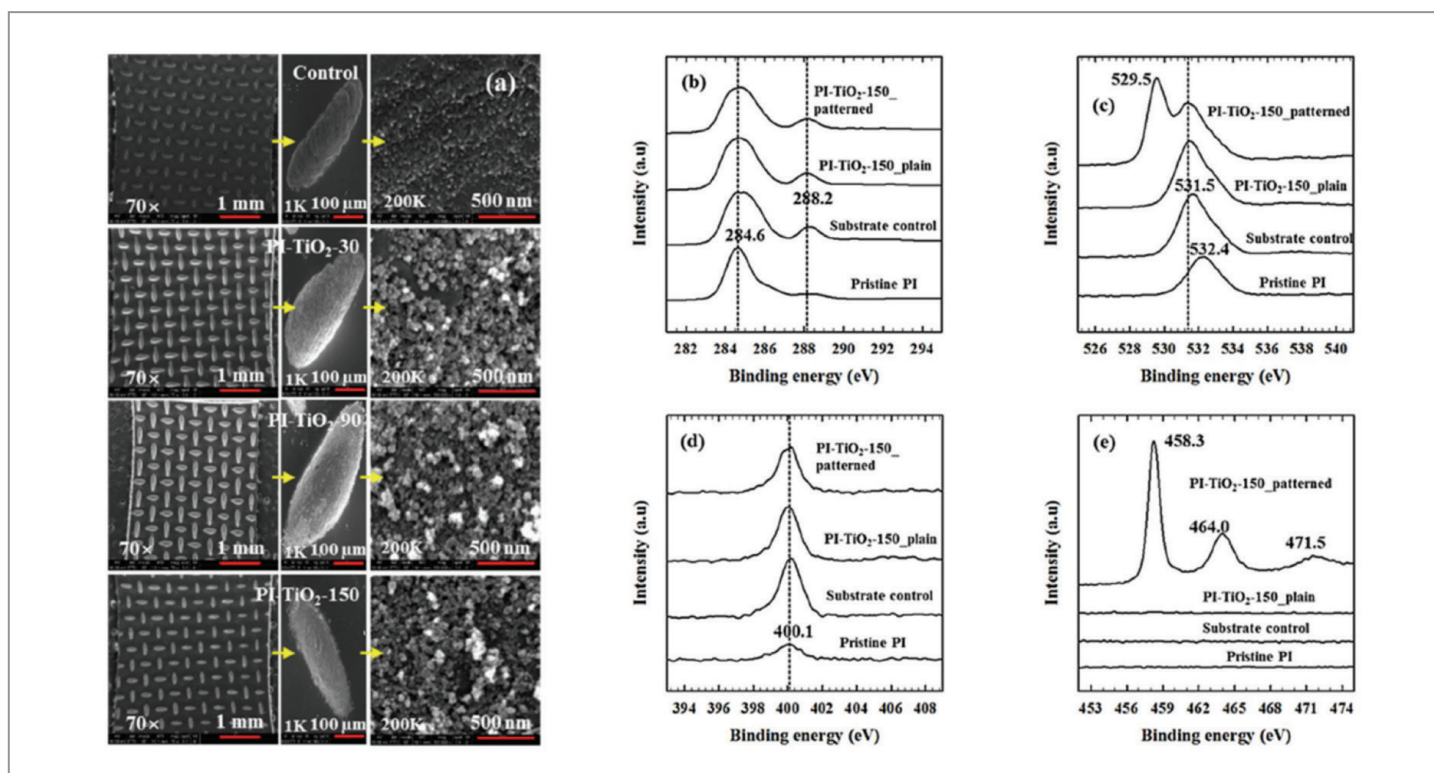
Figure 5 (a) Fe-SEM images of PI-TiO$_2$ samples fabricated with different TiO$_2$ loading and (b-e) XPS spectra of pristine PI, substrate control, and PI-TiO$_2$-150: C1s (b), O1s (c), N1s (d), and Ti2p (e). In PI-TiO$_2$-X, X = total volume (ml) of TiO$_2$-methanol dispersion electrosprayed on template. Left, center, and right columns present the overall image of PI-TiO$_2$, the image of typical TiO$_2$ deposited pattern, and 200K image of TiO$_2$ nanoparticles distributed on patterns, respectively.
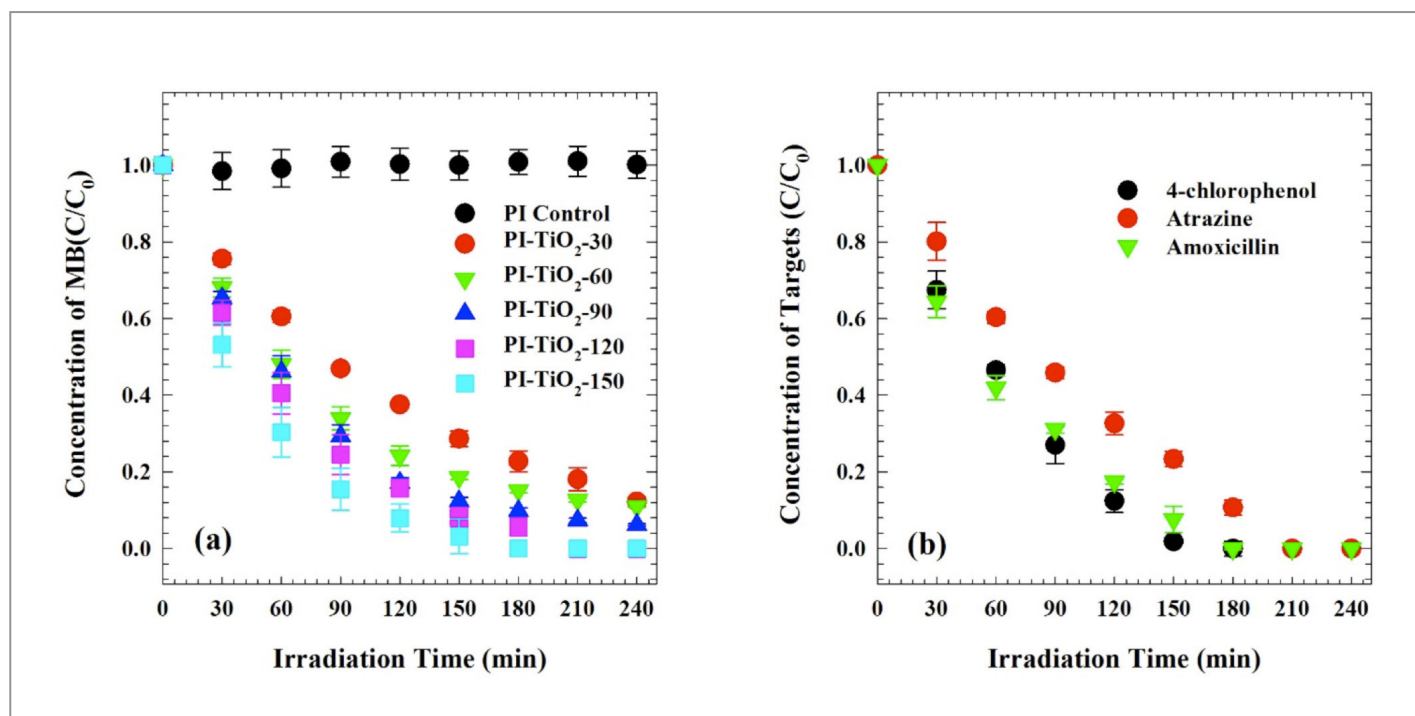
Figure 6   Photocatalytic degradation of (a) methylene blue using PI-TiO$_2$ samples with different TiO$_2$ loading and (b) other targets using PI-TiO$_2$-150. The initial conditions were: [MB]$_0$ = [AMX]$_0$ = [ATZ]$_0$ = [4CP]$_0$ = 10 μM and pHi = 6.8–7.0.

Morphology and surface chemical structure of PI-TiO$_2$

Figure 5a shows the Fe-SEM images of PI-TiO$_2$ fabricated as a function of the volume of TiO$_2$-MeOH electrosprayed on a steel mesh template. On SC, many checker plate patterns could be seen. In 200K images, the surface pattern appeared extremely rough and deformed. The roughness of interconnecting steel wire constituting the template was reflected on the surface pattern. Here, the well-defined pattern formation in SC indicates that under 100 Mpa pressure, PI film softened at 350°C and allowed TiO$_2$ immobilization. It is also known that PI film shrinks when heated at 550-650°C with an abrupt release of oxygen [8]. Nevertheless, SC and PI-TiO$_2$ showed no apparent change in flexibility or color, indicating that the PI film was not degraded during TTP. In all cases, 70× images showed the pattern formation and 200K images exhibited the extent of TiO$_2$ distribution on the patterns.

Figures 5b-e show the C1s, O1s, N1s and Ti2p components of the XPS spectra for PPI, SC, and PI-TiO$_2$-150. C1s spectra exhibit two peaks at 284.6 eV (C-C, C-H, and C-O) and 288.2 eV (C=O) corresponding to the PI chain [6].

The broader 284.6 eV peak also represents the carbon atoms of the phenyl ring singly bonded to oxygen and nitrogen, which are usually observed at 285.4 eV. The broad 288.2 eV peak, spanning from 287.4 to 289.7 eV in SC and all parts of PI-TiO$_2$-150, can represent C=O of imide (288.0 eV), carboxylate (287.9 eV) and amide (289 eV) [9]. Notably, the absence of a peak at 282 eV (Ti-C) indicates that there was no covalent bond formed between PI and TiO$_2$ [7]. In the O1s spectra (Figure 5c), PPI shows a broad peak at 532.4 eV attributed to C=O of imide and carboxylic acid, which are usually observed at 532 eV and 532.4 eV [10], respectively. In SC and all parts of the TiO$_2$-150 patterns, the 534.4 eV (C=O of amide) peak shifted to 531.5 eV. In the N1s spectra (Figure 5d), the peak at ~ 400 eV was diffused in PPI, relatively sharp in SC, and shifted to a lower region in all parts of PI-TiO$_2$-150. The N1s peaks of imide and secondary amide have been reported to appear at 401 and 399 eV, respectively [11]. Ti2p spectra (Figure 5e) show TiO$_2$ peaks at 458.3 and 464.0 eV. The satellite peak which appeared at 471.51 eV resulted from the ionization of Ti(2p3/2) by X-rays. Overall, XPS results indicate that during TTP, the imide ring cleaved to form amide and carboxylic acid groups

Bio / Medical

Materials / Systems

Energy / Environment

Research Highlights

KIST News

Up Close

Interview

due to hydrolysis of the PI surface by water adsorbed from the atmosphere. This type of imide ring opening occurs similarly during alkali hydrolysis of the PI surface.

Photocatalytic application

The photocatalytic properties of PI-TiO$_2$ prepared as a function of the amount of TiO$_2$ immobilized under UVA light conditions (six 4 W black light blue lamps, λ = 350–400 nm) were evaluated based on the removal efficiency of MB as a primary target. Changes in the concentrations of MB were quantified by measuring UV absorbance at 664 nm using a UV-Vis spectrophotometer. Both MB removal efficacies and pseudo-first order rate constants, k, (min^{-1}) increased as the quantity of TiO$_2$ was increased on the PI film. After 4 h irradiation, the removal efficiencies of MB over PI-TiO2-30, -60 and -90 were 87.7, 89.0 and 93.8%, respectively (Figure 6a). Complete decolorization was only achieved by PI-TiO$_2$-120 and -150 samples within 3 h of irradiation. However, direct photolysis and adsorption onto PI-TiO$_2$ were insignificant in the removal of

MB. These results suggest that the photocatalytic reaction which occurred on the surface of TiO$_2$ NPs patterned on PI film was mainly responsible for the degradation of MB.

The applicability of PI-TiO$_2$-150 was further investigated using different kinds of organic pollutants such as AMX, ATZ and 4-CP (Figure 6b). Their concentration profiles were measured by HPLC (LC-20AD, Shimadzu) equipped with a C-18 column (ZORBAX Eclipse XDB-18, Agilent) and UV–vis detector (SPD-20AD, Shimadzu). The direct photolysis and adsorption had insignificant effects on the removal of AMX [12]. After 180 min of illumination, PI-TiO$_2$-150 completely removed AMX with over 40% of TOC reduction. In the case of ATZ, negligible adsorption was observed because there are no specific functional groups in the ATZ molecules which can strongly bind it on the TiO$_2$ surface [1], while UVA light alone resulted in a 30% degradation of ATZ. Under UVA light, the degradation rate of ATZ (0.0170 min-1) by PI-TiO$_2$-150 was higher than that of AMX (0.0141 min-1), which might be attributed to the synergistic effect of direct photolysis and photocatalysis, although a similar TOC removal was found. Like other target
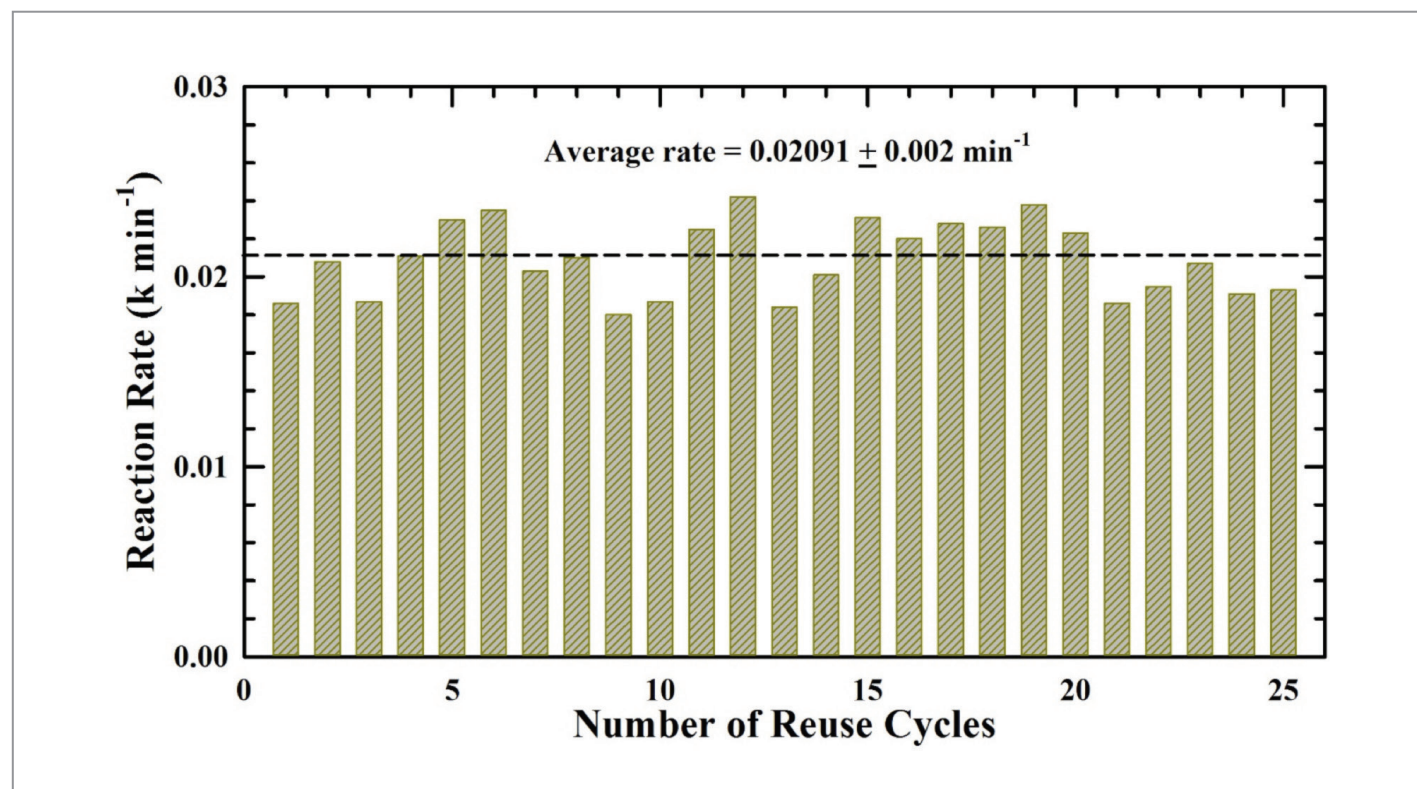
Figure 7   Reaction rate obtained for 25 repeated methylene blue degradation experiments under UVA irradiation using PI-TiO$_2$-150. The dotted line indicates the average reaction rate. The initial conditions were: [MB]0 = 10 μM and pHi = 6.8–7.0.

pollutants, the dominant mechanism for 4-CP removal was photocatalysis, with negligible contributions of adsorption and photolysis. The rate of 4-CP degradation was lower (0.0098 min-1) than those of other targets, but a 77% TOC removal was achieved. According to Stafford et al. [13], hydroxyl radicals and valance band holes contribute to the photocatalytic degradation of 4-CP and its intermediates.
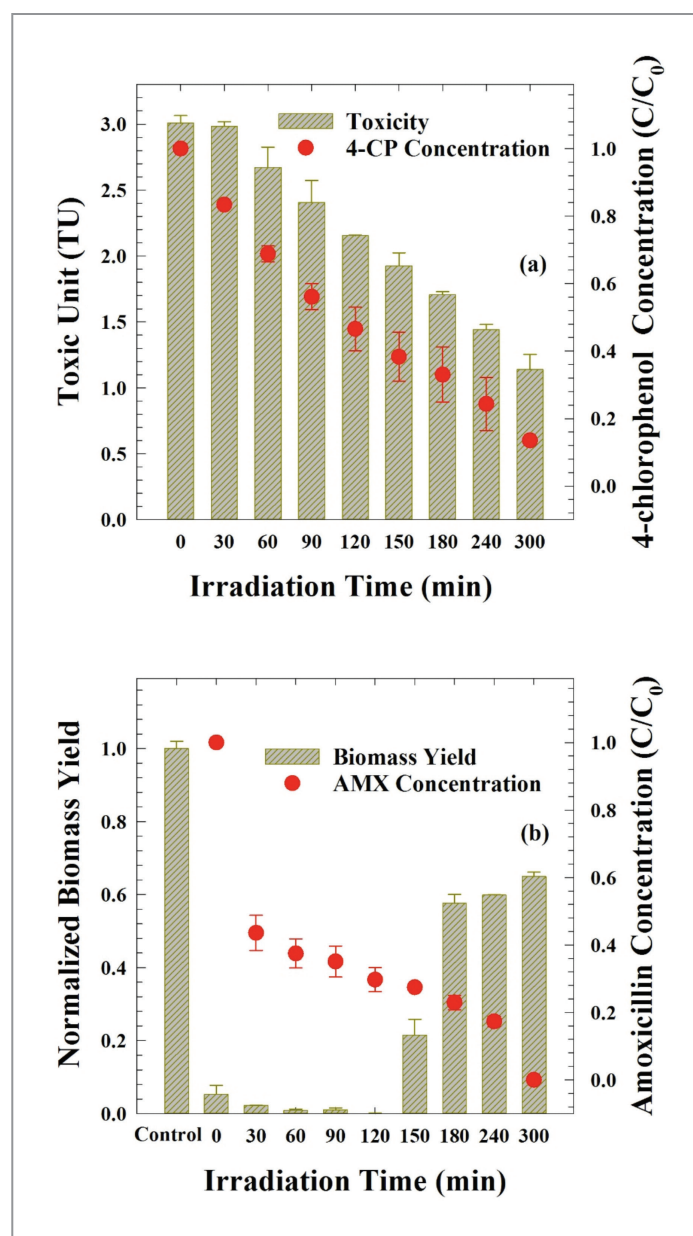
Figure 8   Changes in (a) toxicity of 4-chlorophenol against *Vibro fischeri* and (b) antibiotic activity of amoxicillin against Escherichia coli as a function of photocatalysis time and compared with control (D. l. water). PI-TiO$_2$-150 sample was used in both cases. The initial conditions were: [AMX]0 = [4CP]$_0$ = 20 µM and pHi = 6.8–7.0.

The challenge of a heterogeneous photocatalyst, i.e., immobilized TiO$_2$, is to fabricate a stable, reusable and scalable photocatalyst that has potential for the degradation of emerging pollutants without generating active and more toxic intermediates. Thus, to ensure the continued catalytic performance of fabricated PI-TiO$_2$, the photocatalyst was examined over successive runs (25 cycles) in separate batches. After each cycle, the PI-TiO$_2$-150 was washed thoroughly with water, and a fresh solution of MB was added before the next photocatalytic run. As Figure 7 presents, there was no obvious decrease in the MB degradation rate constants during 1-25 successive runs. The initial and final values were 0.0186 and 0.0193 min^{-1}, respectively, with a mean rate constant of 0.0209 min-1(standard deviation = 0.002). Compared to previously reported data for other forms of immobilized TiO$_2$ [14], the stability of PI-TiO$_2$-150 during reuse was higher, presumably due to roughness-induced adhesion and interfacial hydrogen bonding between the TiO$_2$ and PI. During 25 cycles, the absence of leaching of TiO$_2$ was confirmed by ICP-OES results (data not shown). Consequently, these results suggest that PI-TiO$_2$ was structurally stable upon recycling and could be reused multiple times.

In this study, the changes in toxicity of 4-CP and AMX by photocatalytic treatment with PI-TiO$_2$-150 were studied using the bacterial bioluminescent test Microtox® and growth inhibition assay, respectively. The toxicity results were expressed as toxicity units (TU) and biomass yield that were calculated by the EC$_{50,\ 15min}$ and the difference between the maximal and initial optical density (OD$_{600}$) values, respectively. In Figure 8a, the TU value remained unchanged at the beginning, but decreased gradually after 60 min of treatment due to elimination of 4-CP and its toxic reaction products. On the other hand, the TU values did not change when the sample was exposed to ATZ for 300 min (data not shown).This is consistent with a previous report demonstrating that ATZ is not toxic toward *V. fischeri* up to 6 mg L^{-1} [15].

In order to assess cell viability, the normalized biomass yield of E. coli was plotted as a function of photocatalytic time (Figure 8b). The complete inhibition of *E. coli* growth was observed between 0 and 120 min because the residual AMX concentrations in this period were above the minimum inhibitory concentration (MIC = 0.68-35 µM) [16]. However, after 150 min, the residual concentration of AMX declined below MIC. In response, cell density increased over that time, indicating the occurrence of bacterial growth. Collectively, the above results suggest that the PI-TiO$_2$ photocatalyst is effective

for removing emerging pollutants without generating more toxic intermediates.

Conclusions

In this study, TiO_2-patterned PI film photocatalysts were fabricated using TTP. Steel mesh substrates electrosprayed with TiO_2 were used as templates. Fe-SEM studies confirmed that uniform patterns with greater TiO_2 coverage were formed at 350°C and 100 MPa. EDXS results revealed that the Ti%, indicative of TiO_2, increased with increases in pressure and temperature of TTP. Increases in the electrosprayed volume of TiO_2 increased the quantity of TiO_2 immobilized on PI film as well as the density of TiO_2 coverage on surface patterns. XPS results confirmed the presence of TiO_2 on rice-shaped embossing patterns and indicated the formation of COOH and amide groups during TTP. Under UVA irradiation, PI-TiO_2 effectively photo-oxidized MB. The MB degradation efficiency increased with increases in immobilized quantities of TiO_2. PI-TiO_2-150 completely degraded MB with a degradation rate of 0.0225 min^{-1}. PI-TiO_2-150 exhibited stable degradation of MB for 25 reuse cycles with no leaching of TiO_2. PI-TIO_2-150 also effectively degraded other target compounds, AMX, ATZ, and 4-CP, which confirmed the preservation of the non-selective oxidation nature of TiO_2 photocatalysis. Photocatalysis with PI-TiO_2-150 for 300 min decreased the toxicity of 4CP against the bioluminescent bacteria *V. fischeri* by 62.1% and facilitated the regrowth of *E. coli* during AMX degradation.

Overall, our findings indicate that TTP is a simple and viable route to fabricate robust PI-TiO_2 photocatalyst. Furthermore, the high thermal and oxidative stability of PI film makes it an excellent candidate for applications in various fields, including microelectronics and space exploration.

Note

This article and images are drawn from "Preparation, characterization, and application of TiO_2-patterned polyimide film as a photocatalyst for oxidation of organic contaminants" in *Journal of Hazardous Materials,* 2017; Vol. 340: 300-308

References

[1] Chong MN, Jin B, Chow CWK, Saint C. *Water Res*. 2010; 44: 2997.

[2] Shan AY, Ghazi TIM, Rashid SA. *Appl. Catal. A Gen*. 2010; 389: 1.

[3] Ramasundaram S, Son A, Seid MG, Shim S, Lee SH, Chung YC, Lee C, Lee J, Hong SW. *J. Hazard. Mater*. 2015; 285: 267.

[4] Ramasundaram S, Seid MG, Choe JW, Kim EJ, Chung YC, Cho K, Lee C, Hong SW. *Chem. Eng. J*. 2016; 306: 344.

[5] Liaw DJ, Wang KL, Huang YC, Lee KR, Lai JY, Ha CS. *Prog. Polym. Sci*. 2012; 37: 907.

[6] Georgiev DG, Baird RJ, Newaz G, Auner G, Witte R, Herfurth H. *Appl. Surf. Sci*. 2004; 236: 71.

[7] Liaw WC, Cheng YL, Liao YS, Chen CS, Lai SM. *Polym. J*. 2011; 43: 249.

[8] Inagaki M, Harada S, Sato T, Nakajima T, Horino Y, Morita K. *Carbon N. Y*. 1989; 27: 253.

[9] Yu W, Ko TM. *Eur. Polym. J*. 2001; 37: 1791.

[10] Lee HS, Im SJ, Kim JH, Kim HJ, Kim JP, Min BR. *Desalination* 2008; 219: 48.

[11] Ghosh I, Konar J, Bhowmick AK. *J. Adhes. Sci. Technol*. 1997; 11: 877.

[12] Elmolla ES, Chaudhuri M. *Desalination* 2010; 252: 46.

[13] Stafford U, Gray KA, Kamat PV. *J. Phys. Chem*. 1994; 98: 6343.

[14] Su C, Tong Y, Zhang M, Zhang Y, Shao C. *RSC Adv*. 2013; 3: 7503.

[15] Doll TE, Frimmel FH. *Catalysis Today* 2005; 101: 195.

[16] Andrews JM. *Chemother. 48 Suppl*. 2001; 1: 5.

Feature Articles

A Highly Efficient, Photovoltaic-Thermoelectric Hybrid Generator

Introduction

Seung Hyub BAEK

Principal Researcher
Center for Electronic Materials
Post-Silicon Semiconductor Institute

shbaek77@kist.re.kr

Won Jun CHOI

Principal Researcher
Center for Opto-Electronic Materials
and Devices
Post-Silicon Semiconductor Institute

wjchoi@kist.re.kr

Among all photovoltaic technologies, concentrating photovoltaic (CPV) systems are currently attracting the most attention because they possess the highest efficiency [1]. CPV systems use mirrors or lenses to focus sunlight onto a small array of CPV cells. This not only potentially enhances the conversion efficiency from solar to electric energy, but also reduces the balance of system costs due to the system's small size [2-3].

However, concentrating sunlight inevitably causes heat generation, so it significantly increases the temperature of CPV cells. High temperature is very detrimental to the performance of solar cells. Band gap reduction and a higher recombination rate at high temperatures substantially decrease the open-circuit voltage (V_{oc}) of a solar cell, leading to a degradation of solar cell performance [4-5]. Usually, CPV systems include a heat sink to effectively dissipate heat [6-7]. There are, however, limitations associated with heat sink installation; for example, active cooling below the ambient temperature is not desirable because of the extra energy consumption for cooling.

One way to further enhance a CPV cell is to actively utilize the dissipated heat energy as a source for extra generation of electricity using a thermoelectric generator (TEG) [8-9]. All these hybrid generators have a common structure: the PV cell is placed on the top (hot) side of the TEG while the bottom side of the TEG is connected to a heat sink. In this structure, however, the CPV cell and TEG have a competing relationship: CPV cells prefer a low temperature while the TEG creates a high temperature (gradient). Moreover, as they are thermally connected with each other, interactive effects between the CPV and TEG emerge [10]. Therefore, for the hybrid generator to reach its full potential, a successful strategy must accommodate these effects.

This study focuses on the demonstration of a highly efficient CPV/TE hybrid generator designed as a vertical combination of a GaAs-based single-junction CPV cell and a commercial

thermoelectric module. This hybrid generator exhibits higher efficiency than a single CPV cell at a high solar concentration. The keys to the technology are (1) to control the thermal flow in such a way as to reduce the temperature of the CPV cell and (2) to consider the Peltier effect that can further decrease the CPV cell temperature while maintaining high TEG output power. The latter is achieved simply by impedance matching while the former is accomplished by transferring the CPV cell from a GaAs to Si substrate that has a higher thermal conductivity using the wafer bonding and epitaxial lift-off process.

Results and discussion

Schematic of our CPV/TE hybrid generator

Figure 1 shows a schematic illustration of our CPV/TE hybrid generator. This includes a Fresnel lens, a GaAs-based single-junction PV cell, a TE module, and a heat sink. The Fresnel lens concentrates the light from the xenon lamp in a solar simulator. The solar concentration can be varied by the position of the Fresnel lens as well as the power of the lamp. A single-junction, GaAs-based CPV cell is placed on top of a commercial TEG (RMT, 1MC04-030-05TEG). A homemade aluminum heat sink with a fan blowing air at a speed of 3.4 m/s is used for cooling the cold side of the TEG. The power generation of the GaAs-based CPV cell is monitored by the current density versus voltage (J-V) measurement. Meanwhile, the power generation of the TEG is evaluated by measuring electric power consumed in the external load to understand Peltier effects on the efficiency of our hybrid generator.

Comparison of PV cells on GaAs & Si substrates

In order to maximize the total performance of our hybrid generator, it is necessary to lower the temperature of the PV cell, the hottest part of the generator. For this, we replace the GaAs substrate on which the PV cell is initially grown with Si substrate using the wafer bonding and epitaxial lift-off process [11]. The thermal conductivity of Si is 150 W/m·K while that of GaAs is 46 W/m·K. Moreover, the heat capacity of Si (700 J/kg·K) is higher than that of GaAs (330 J/kg·K). As we discuss later, the PV cell transferred on the Si substrate shows a better performance than the as-grown one on the GaAs substrate
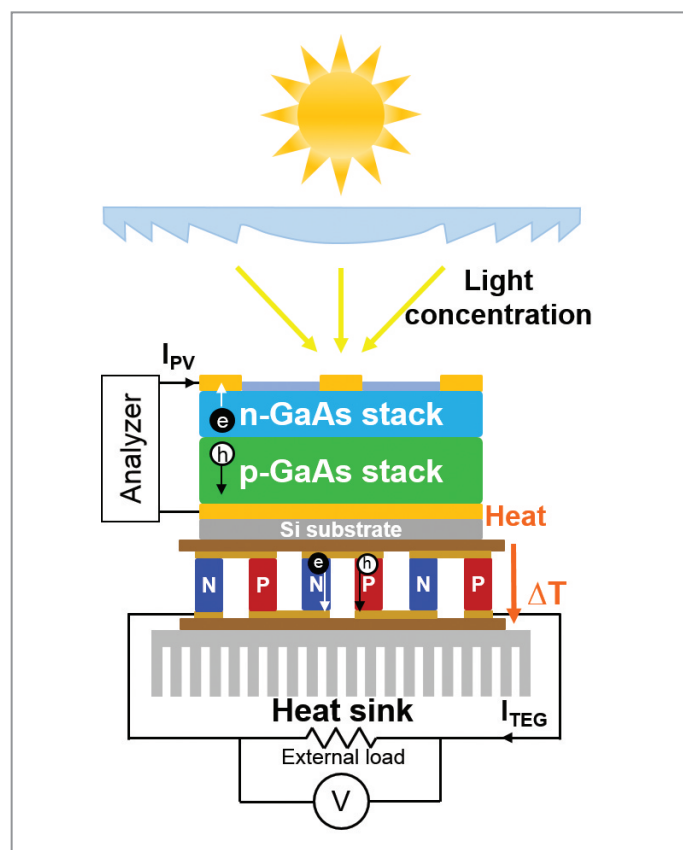

Figure 1 Schematic diagram of CPV/TE hybrid generator.

at high solar concentrations. The detailed process of PV cell transfer is described in Figure 2a. An epitaxial $Al_{0.85}Ga_{0.15}As$ layer (10 nm) is grown on (001) GaAs substrate as a sacrificial layer and then, GaAs-based heteroepitaxial stacks for PV cells are grown. An overlayer of Au (10 nm)/Pt (10 nm) is deposited on both a GaAs-based PV cell stack and a bare Si wafer. The Au/Pt layer is treated by Ar plasma in a reactive-ion etching chamber to activate the surfaces. The Au/Pt/Si wafer and Au/Pt/GaAs-based heteroepitaxial PV cell stack are bonded manually with a light pressure in the air. Then, we selectively etch the $Al_{0.85}Ga_{0.15}As$ sacrificial layer by HF solution to complete the transfer. Note that we are able to reuse the GaAs substrate for the growth of GaAs-based heteroepitaxial PV cell stacks.

We carry out a J-V measurement to compare a CPV cell on the GaAs substrate and one transferred to the Si substrate, as shown in Figure 2b. Note that all measurements are carried out in a thermally steady-state condition after the xenon lamp is turned on. The short circuit current density (J_{sc}) of the CPV cell on Si is 29.648 mA/cm^2, which is slightly higher than on the CPV cell on GaAs (26.655 mA/cm^2) under an air mass (AM)
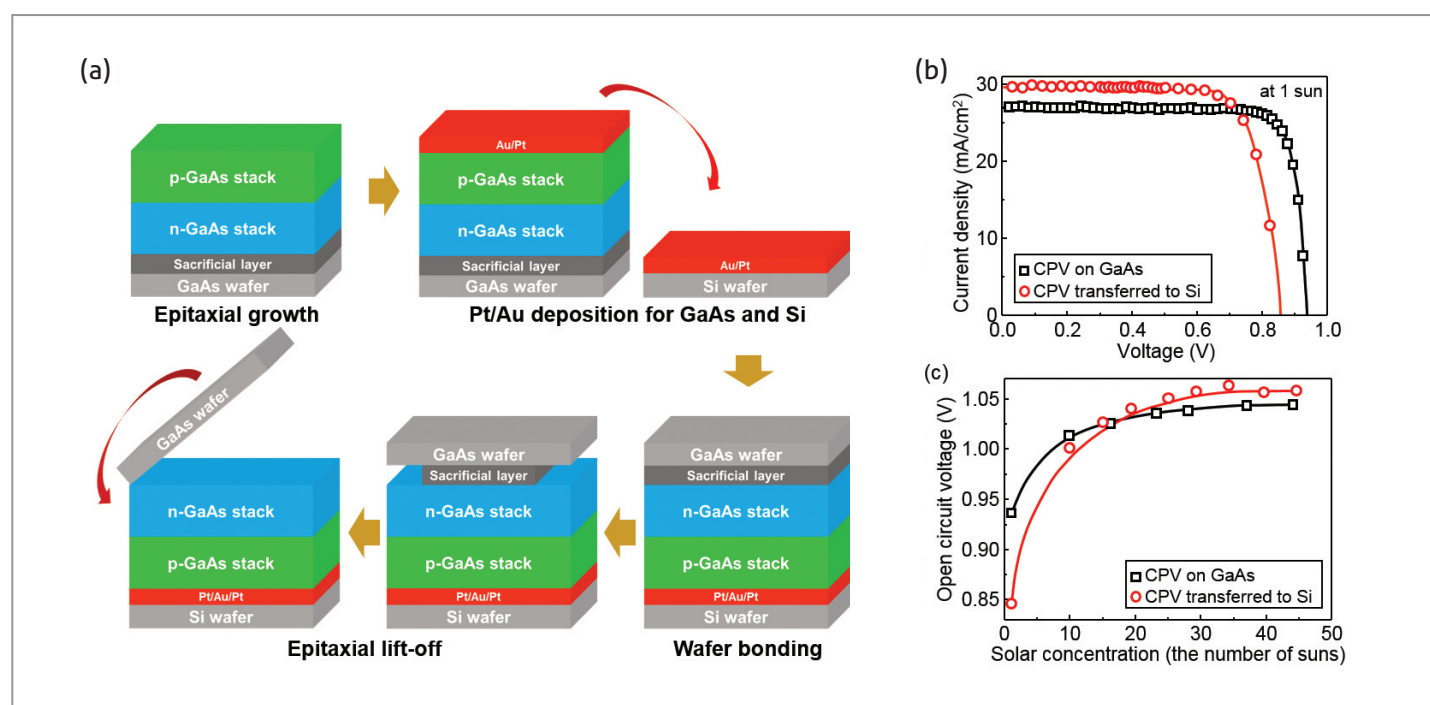
Figure 2 Wafer bonding & epitaxial lift-off process of GaAs solar cell and performance comparison of as-grown PV and transferred PV. (a) Schematic illustration of wafer bonding & epitaxial lift-off process of GaAs solar cell. (b) Comparison of J-V curve between CPV cell on GaAs and CPV cell transferred to Si at 1 sun. (c) Comparison of open-circuit voltages between CPV cell on GaAs and CPV cell transferred to Si with increasing solar concentrations.

1.5G 1 sun illumination (1 sun = 100 mW/cm² is the standard condition). We believe that a higher J_{sc} of the CPV cell on Si may be attributed to the light reflection from the back metal of Pt/Au, which is used for the wafer bonding. By contrast, V_{oc} of the CPV cell on Si (0.85 V) is smaller than that on GaAs (0.94 V). This is due to possible cracks formed during the bonding process and/or different qualities in the epitaxial layer for the CPV cell on GaAs and Si [12]. This unoptimized Ohmic contact between Pt/Au and the CPV cell in the transferred CPV reduces the fill factor (FF). Thus, despite the higher J_{sc} of the PV cell on Si than the one on GaAs, lower FF leads to a lower efficiency of the PV cell on Si (19.6 %) than that on GaAs (20.26%) at 1 sun.

To investigate the heat dissipation effect for different substrates at high solar concentrations, the V_{oc} of PV cells is measured as a function of the solar concentration, as shown in Figure 2c. Both cells are placed on an aluminum heat sink cooled by a fan during measurement. V_{oc} is directly affected by the temperature of the solar cell. Regardless of the substrates, the overall trend is that V_{oc} increases with the solar concentration and becomes saturated in high concentration due to thermal degradation. Note that the V_{oc} of the PV cell on the Si substrate, although initially smaller (at 1 sun), becomes larger at high solar concentrations than that on the GaAs substrate. This is attributed

to the advantageous thermal property of Si substrate over GaAs substrate for the effective reduction of the cell temperature by fast heat dissipation. These results strongly indicate that replacing GaAs substrates with Si substrates would greatly mitigate the performance degradation of the PV cell at a high solar concentration.

Optimization of the hybrid generator by controlling external conditions

To optimize conditions for maximum output of the hybrid generator, we characterize the performance of the PV cell and TEG at 30 suns. Figure 3a shows the efficiency of the TEG in the hybrid generator as a function of the load resistance. The output power of the TEG is evaluated by calculating the consumed electric power (V_{load}^2/R_{load}) at the load resistance, where V_{load} indicates the measured voltage-drop across the load resistance. The output power is normalized by an area of the TEG (0.64 cm × 0.64 cm) to obtain the energy density. The efficiency of the TEG is calculated from the ratio of this energy density with a unit of mW/cm2 to the input solar power (3000 mW/cm²).

The efficiency of the TEG increases with the magnitude
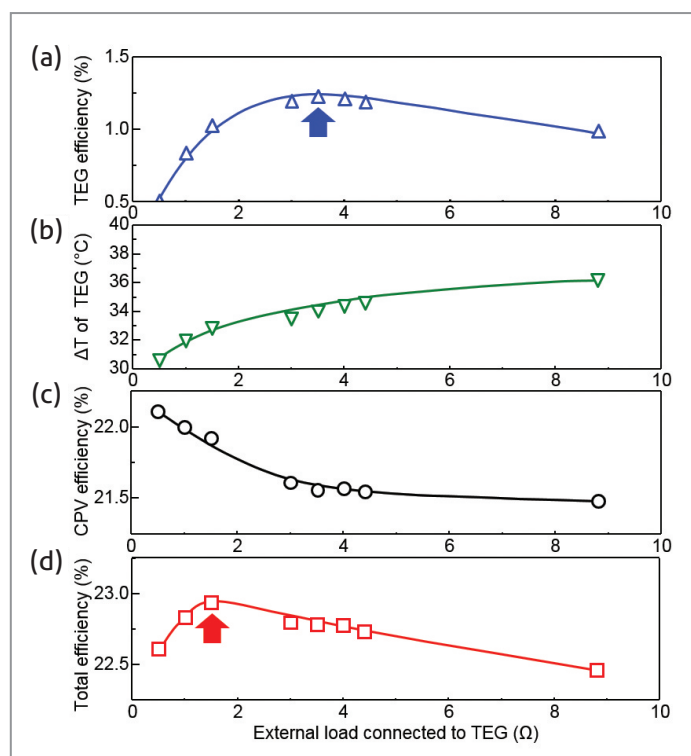
Figure 3   Effect of the resistance of an external load connected to TEG on the efficiency of the hybrid generator at 30 suns. (a) TEG efficiency. (b) The temperature difference between hot and cold sides of TEG. (c) CPV efficiency. (d) The total efficiency of the hybrid generator.

of the load resistance, and then, after the maximum point at around 3.5 Ω, it decreases. Usually, to optimally deliver energy from a generator to a load, impedance matching is required between the generator and the load. Note that the TEG is not an independent energy source; it is affected by the feedback of Peltier effects, the reverse phenomenon of the Seebeck effect. An analytical expression for optimum load resistance for a given ZT is $R_{Load} = R_{TEG}\sqrt{1 + ZT}$, where Z and T are the thermoelectric figure-of-merit and the absolute temperature, respectively [13]. Therefore, the optimum load resistance (~3.5 Ω) for the maximum power generation of TEG is determined, which is a little higher than the internal resistance (~2.7 Ω) of the TEG.

The temperature difference between the hot and cold side of the TEG can be evaluated by the Seebeck relation of $V_{oc}=\alpha\Delta T$, where α is the Seebeck coefficient of TEG, as shown in Figure 3b. ΔT of the TEG increases as the load resistance increases. This can be explained by the Peltier effect, where the temperature gradient between both ends of the TEG increases with the current flowing through it. As the Peltier effect counteracts the Seebeck effect, the temperature gradient

induced by the Peltier effect is developed in a way that reduces the externally given ΔT. With increasing load resistance, the current through the TEG decreases, leading to the reduction of the Peltier effect. The maximum limit of ΔT in the TEG can be estimated as ~41℃ by measuring V_{oc} when the Peltier effect becomes negligible.

The dependence of the ΔT at the TEG on the load resistance affects the efficiency of the CPV cell on top of the TEG as well. As shown in Figure 3c, the efficiency of the CPV cell in the hybrid generator shows a strong dependence on the load resistance connected to the TEG. In our hybrid generator, the TEG is placed on an aluminum heat sink, which maintains the cold side of the TEG at close to ~25℃. Therefore, the change of ΔT shown in Figure 3b leads mainly to a temperature change at the hot side of the TEG. Thus, the efficiency of the CPV cell decreases as the load resistance connected to the TEG increases, because the temperature of the CPV cell increases.

Such interplay between the PV cell and the TEG in the hybrid structure plays an important role in determining optimum conditions for maximum efficiency. Figure 3d shows the total efficiency of our hybrid generator as a function of the load resistance connected to the TEG. Notably, our hybrid generator shows a maximum efficiency at 1.5 Ω of the load resistance. Based on this result, we can deduce that the resistance of an external load should be lowered to enhance the CPV efficiency by Peltier cooling.

Performance analysis of the hybrid generator compared to the single PV cell

We compare the efficiency of the hybrid generator with that of the single CPV cell only as a function of the solar concentrations, as shown in Figure 4. Both the hybrid generator and CPV cell (transferred to Si substrate) are measured under the same conditions. For our hybrid generator, an external load with 2.5 Ω is connected to the TEG.

Our hybrid generator (red curve) outperforms the single CPV cell (green curve) when the solar concentration exceeds ~33 suns. At low solar concentrations, the hybrid generator exhibits lower efficiency than the single CPV cell. This is due to both the significant reduction of the CPV cell (black curve) in the hybrid structure and the insufficient output of the TEG (blue curve). The TEG works as a thermal barrier to block the heat flow from the CPV cell to the heat sink, resulting in an increase in the CPV cell temperature. Also, as ΔT is still small at low solar concentrations, the output power by the TEG
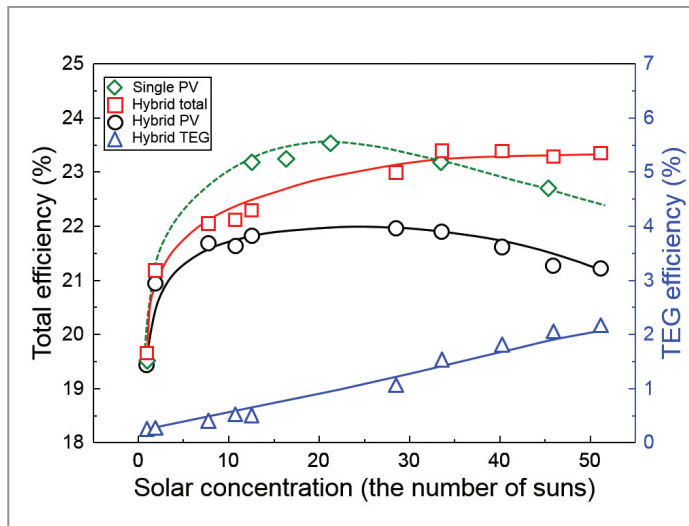
Figure 4   Comparison of total efficiency between the CPV/TE hybrid generator and the single CPV cell as a function of solar concentrations

does not compensate for this change. On the contrary, at high solar concentrations, the single CPV cell shows a degradation of efficiency from ~20 suns. The hybrid generator can compensate for such an efficiency loss by the TEG. Note that the efficiency of the TEG proportionally increases with solar concentration. This can be explained by the following relationships:

P_{out} of TEG ~ $(\Delta T)^2$ [14] ,
ΔT of TEG ~ solar concentrations ~ P_{in},
Efficiency of TEG = P_{out} / P_{in} ~ $(\Delta T)^2/\Delta T = \Delta T$

This indicates that the integration of the CPV cell with the TEG would be a promising way to further improve the efficiency of clean energy generation. Note that our hybrid generator is demonstrated using a commercially available TEG that is not specifically optimized for hybridization. By properly designing the structure of the TEG, it would be possible to develop a highly efficient generator, which a single branch of the various clean-energy technologies cannot achieve solely.

As stated above, in the hybrid structure, the two constituent generators, CPV and TEG, are competing with each other: low temperature is favorable for the CPV cell while high temperature (gradient) is a better condition for the TEG. Therefore, the key is to find an optimum condition with a consideration of the trade-off relationship between the CPV cell and TEG. For this, we presented two effective solutions: (1) transferring the CPV cell grown on GaAs substrate to Si

substrate using a wafer bonding and epitaxial lift-off process and (2) matching the load-resistance to utilize the Peltier cooling effect. The former process is meant to lower the temperature of the CPV cell (Si has a thermal conductivity four times higher than GaAs). The latter is to additionally improve the CPV's efficiency by further lowering the CPV temperature while maintaining high efficiency of the TEG.

Conclusions

We developed a highly efficient CPV/TE hybrid generator using a GaAs-based, single-junction CPV cell and a commercial TEG to resolve the issue of thermal degradation in a conventional CPV cell. We showed that our hybrid generator improves on the conversion efficiency of a single CPV cell by ~3% at a solar concentration of 50 suns. These results demonstrate conclusively that CPV/TE hybridization is a promising way to enhance efficiency and reveal that controlling the heat flow through the hybrid generator and exploiting the Peltier cooling effect of TEG are the keys to realizing a highly efficient hybrid generator. Our work provides a framework for designing a highly efficient hybrid generator utilizing both photoelectric and photothermal effects in clean-energy production.
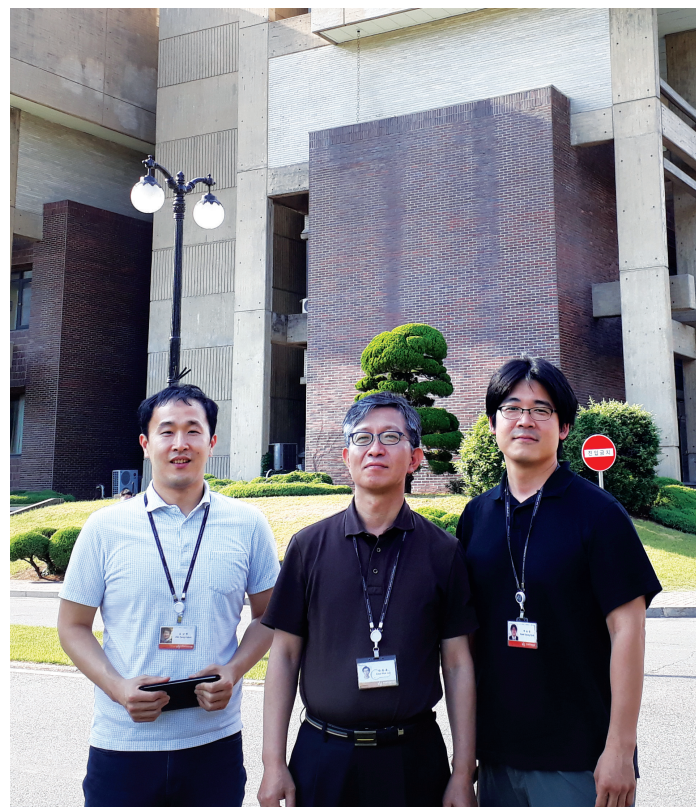
Note

This article and images are drawn from "A highly-efficient, concentrating-photovoltaic/thermoelectric hybrid generator" in *Nano Energy*, 2017; Vol. 37: 242-247.

References

[1] Green MA, Emery K, Hishikawa Y, Warta W, Dunlop ED. *Prog. Photovolt.: Res. Appl*. 2016; 24: 905–913.

[2] Nishioka K, Takamoto T, Agui T, Kaneiwa M, Uraoka Y, Fuyuki T. *Sol. Energy Mater. Sol. Cells* 2006; 90: 57–67.

[3] Feuermann D, Gordon JM. *Sol. Energy* 2001; 70: 423–430.

[4] Dalal VL, Moore AR. *J. Appl. Phys*. 1977; 48: 1244–1251.

[5] Skoplaki E, Palyvos JA. *Sol. Energy* 2009; 83: 614–624.

[6] Yang K, Zuo C. *Energy Convers. Manage*. 2015; 89: 214–221.

[7] Micheli L, Sarmah N, Luo X, Reddy KS, Mallick TK. *Renew. Sustain. Energy Rev*. 2013; 20: 595–610.

[8] Vorobiev Y, González-Hernández J, Vorobiev P, Bulat L. *Sol. Energy* 2006; 80: 170–176.

[9] Kraemer D, Hu L, Muto A, Chen X, Chen G, Chiesa M. *Appl. Phys. Lett*. 2008; 92; 243503.

[10] Beeri O, Rotem O, Hazan E, Katz EA, Braun A, Gelbstein Y. *J. Appl. Phys*. 2015; 118: 115104.

[11] Geum DM, Park MS, Lim JY, Yang HD, Song JD, Kim CZ, Yoon E, Kim S, Choi WJ. *Sci. Rep*. 2016; 6: 20610.

[12] Wu FL, Ou SL, Kao YC, Chen CL, Tseng MC, Lu FC, Lin MT, Horng RH. *Opt. Express* 2015; 23: 18156–18165.

[13] Lossec M, Multon B, Ben Ahmed H, Goupil C. *Eur. Phys. J. Appl. Phys*. 2010; 52: 11103.

[14] Rowe DM, Min G. *J. Power Sources* 1998: 73: 193–198.

Bio / Medical

Materials / Systems

Energy / Environment

Research Highlights

KIST News

Up Close

Interview

Highly Selective and Sensitive Detection of Cr^{6+} Ions Using Size-Specific Label-Free Gold Nanoparticles

November 2017 / *Sensors and Actuators B: Chemical* / Vol. 251 /683-691

Kang Bong LEE
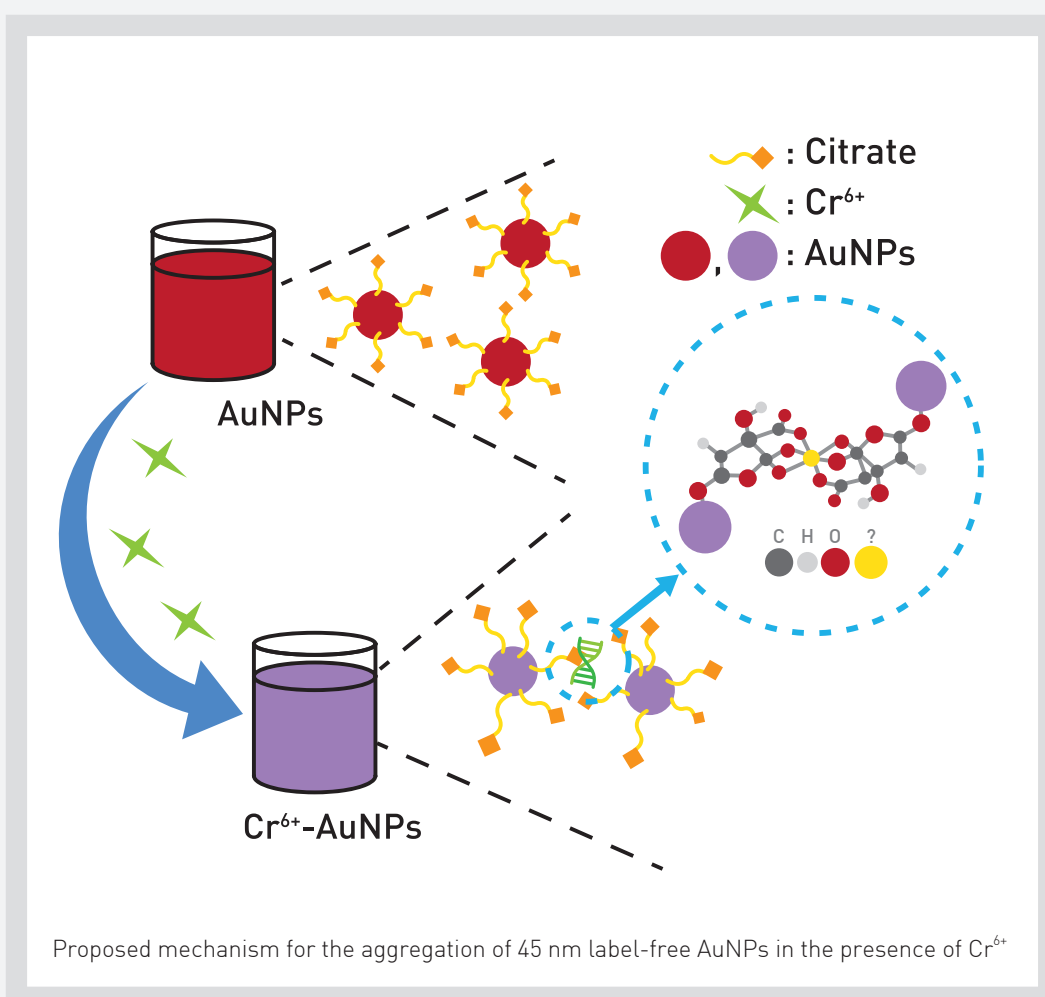
Principal Researcher
Green City Technology
Institute

leekb@kist.re.kr

Yun Sik NAM

Principal Specialist
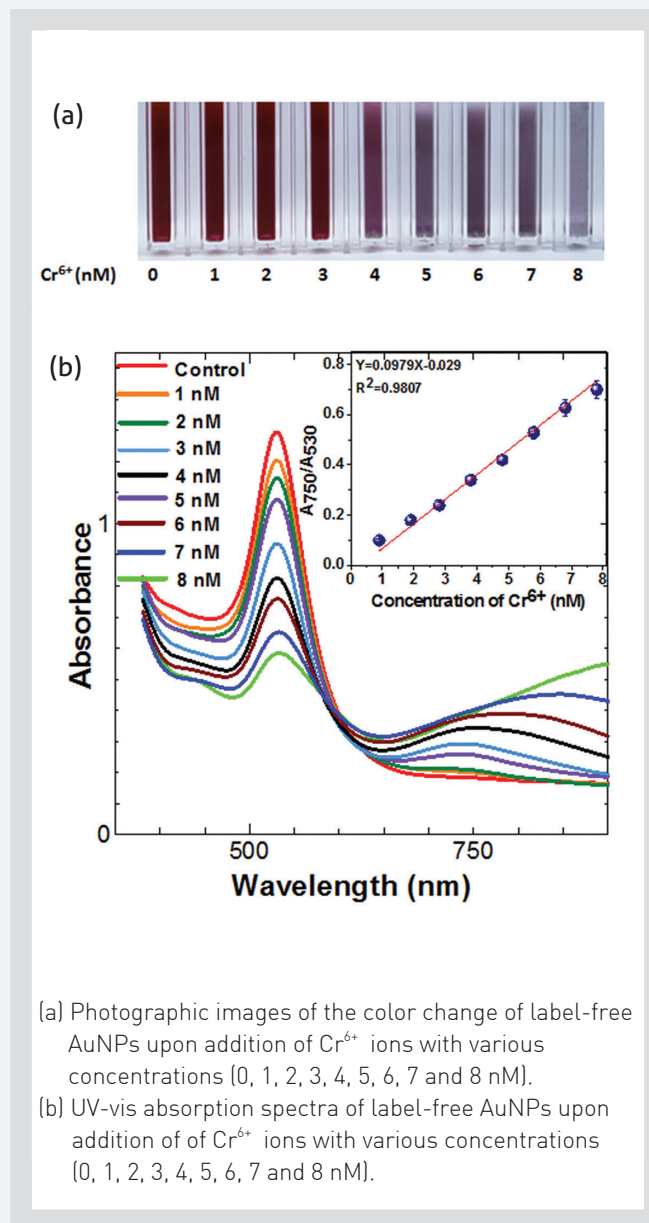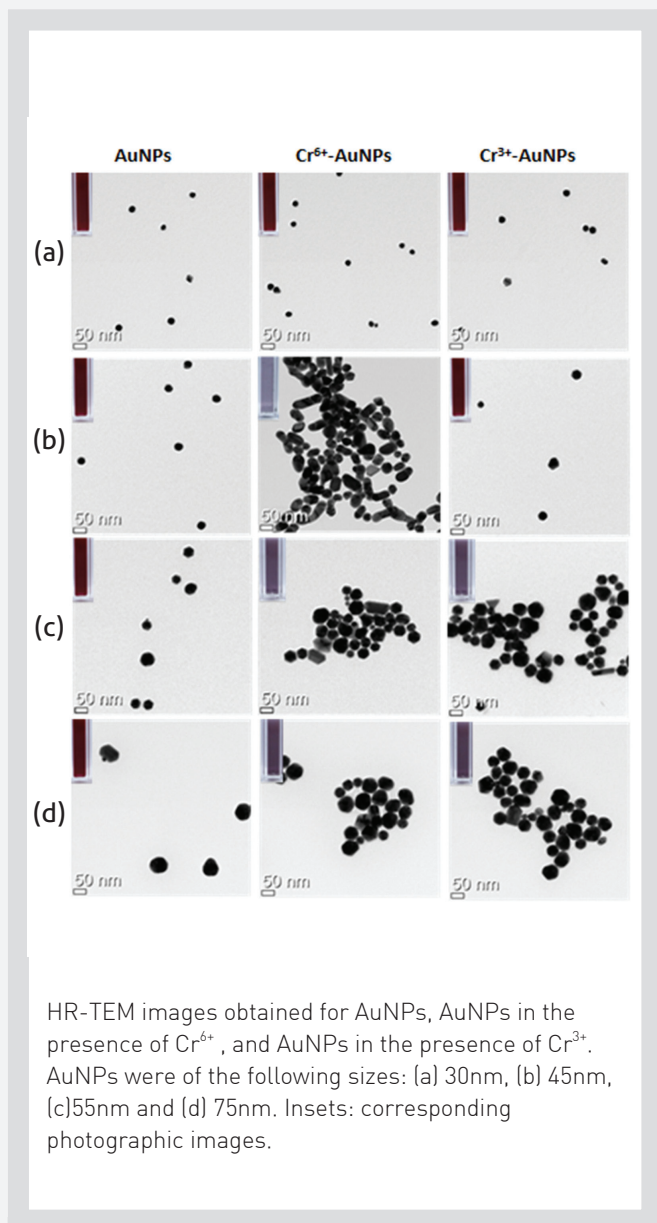Advanced Analysis
Center
Research Planning &
Coordination Division

ysnam@kist.re.kr

Proposed mechanism for the aggregation of 45 nm label-free AuNPs in the presence of Cr^{6+}

Gold nanoparticles (AuNPs) of various sizes were synthesized by modifying their citrate concentration; 45 nm AuNPs were found to respond to Cr^{6+} ions selectively. Label-free AuNPs, 45 nm, showed localized surface plasmon resonance bands at 530 nm, which decreased linearly upon addition of Cr^{6+}. The addition of Cr^{6+} also resulted in the appearance of a new band at 750 nm, along with a visible color change in the solution from wine red to violet. The decrease in absorbance and color change were due to AuNP aggregation upon coordination of

HR-TEM images obtained for AuNPs, AuNPs in the presence of Cr^{6+}, and AuNPs in the presence of Cr^{3+}. AuNPs were of the following sizes: (a) 30nm, (b) 45nm, (c)55nm and (d) 75nm. Insets: corresponding photographic images.

(a) Photographic images of the color change of label-free AuNPs upon addition of Cr^{6+} ions with various concentrations (0, 1, 2, 3, 4, 5, 6, 7 and 8 nM).

(b) UV-vis absorption spectra of label-free AuNPs upon addition of of Cr^{6+} ions with various concentrations (0, 1, 2, 3, 4, 5, 6, 7 and 8 nM).

Cr^{6+}. The detection limit for $Cr^{6+}$was 0.4 nM, and excellent selectivity was observed in the presence of other metal ions and anions. The binding site and sensing mechanism for Cr^{6+} and label-free AuNPs were characterized by X-ray photoelectron spectroscopy and time-of-flight secondary ion mass spectrometry. This method was applied to tap, pond, and wastewater samples and validated using inductively coupled plasma-optical emission spectrometry, illustrating the utility of our sensitive, selective, and simple AuNP sensor in the detection of Cr^{6+}.

Multiple hyperthermia-mediated release of TRAIL/SPION nanocomplex from thermosensitive polymeric hydrogels for combination cancer therapy

Zhi Qiang ZHANG, Soo Chang SONG

scsong@kist.re.kr

High throughput differential identification of TMPRSS2-ERG fusion genes in prostate cancer patient urine

Hyo Jin LEE, Dong Jin LEE, Jea Ho PARK, Sang Hoon SONG, In Gab JEONG, Choung Soo KIM, Peter C. SEARSON, Kwan Hyi LEE

kwanhyi@kist.re.kr

Tumor necrosis factor-related apoptosis-inducing ligand (TRAIL) possesses strong anti-cancer potential because of its ability to specifically kill cancer cells. However, clinical use of TRAIL is impeded by its short *in vivo* half-life and native TRAIL-resistant cancer cell populations. To overcome these limitations, we designed a multiple magnetic hyperthermia (MHT)-mediated TRAIL release system for combination therapy using an injectable, biodegradable and thermosensitive polymeric hydrogel. In this system, positively charged TRAIL and hydrophobic superparamagnetic iron oxide nanoparticles (SPIONs) were complexed with negatively charged poly (organophosphazene) polymers via ionic and hydrophobic interactions, respectively. Transmission electron microscopy images showed a nano-sized core-shell structure of the TRAIL/SPION polymeric nanocomplex in aqueous solution that transformed into a hydrogel at body temperature. Hyperthermia can enhance the release of TRAIL from hydrogels through temperature-sensitive hydrogel dissolution. TRAIL-resistant U-87 MG cells were killed by the combination of TRAIL and multiple hyperthermia via caspase-3 and -8 active apoptosis. The hyperthermia-enhanced cytotoxicity of TRAIL was dependent on the hyperthermia cycle number and corresponding TRAIL release. Significant *in vivo* tumor reduction was observed by combining 2 cycles of mild MHT and TRAIL release using a single injection of TRAIL/SPION nanocomplex hydrogels without damage to main organs. Furthermore, the therapeutic outcomes can be monitored by long-term magnetic resonance imaging

Identifying genetic diversity is important for studies in cancer as it can provide clues to disease progression and appropriate treatment. Although cancer patients may experience similar clinical outcomes and major symptoms, the type of overexpressed gene present in the disease may be different. Even though prostate-specific antigen assay is a good tool widely used for prostate cancer diagnosis, it is not capable of providing information on genetic differences. Therefore, a screening method that can differentiate genetic differences is necessary. Here we detected different types of TMPRSS2-ERG, prostate cancer-specific fusion genes, to verify the genetic diversity between patients using the high throughput screening method, bio-barcode assay. Prostate cancer patients with different types of fusion genes were successfully differentiated from their untreated urine, a result which traditional PSA assay cannot provide. This non-invasive assay, when used with PSA assay, can be a strong secondary screening method offering new insights on disease progression and clinical outcome.

Flexible and robust thermoelectric generators based on all-carbon nanotube yarn without metal electrodes

Jae Yoo CHOI, Yeon Su JUNG, Seung Jae YANG, Jun Young OH, Jin Woo OH, Ki Young JO, Jeong Gon SON, Seung Eon MOON, Chong Rae PARK, Hee Suk KIM

heesukkim@kist.re.kr

As practical interest in flexible or wearable power-conversion devices increases, the demand for high-performance alternatives to thermoelectric (TE) generators based on brittle inorganic materials is growing. Herein, we propose a flexible and ultralight TE generator (TEG) based on carbon nanotube yarn (CNTY) with excellent TE performance. The as-prepared CNTY shows a superior electrical conductivity of 3147 S/cm due to increased longitudinal carrier mobility derived from a highly aligned structure. Our TEG is innovative in that the CNTY can perform multiple functions in the same device. The CNTY is alternatively doped into n- and p-types using polyethylenimine and $FeCl_3$, respectively. The highly conductive CNTY between the doped regions is used as electrodes to minimize the circuit resistance, thereby forming an all-carbon TEG without additional metal deposition. A flexible TEG based on 60 pairs of n- and p-doped CNTY shows a maximum power density of 10.85 and 697 µW/g at temperature differences of 5 and 40 K, respectively, which are the highest values among reported TEGs based on flexible materials. We believe that the strategy proposed here to improve the power density of flexible TEG by introducing highly aligned CNTY and designing a device without metal electrodes shows great potential for flexible or wearable power-conversion devices.

Selective detection of chlorine at room temperature utilizing single-walled carbon nanotubes functionalized with platinum nanoparticles synthesized via ultraviolet irradiation

Sun Woo CHOI, Byung Moon KIM, Sang Hyub OH, Young Tae BYUN

byt427@kist.re.kr

In this study, photoreduction by an ultraviolet (UV) irradiation method was applied to synthesizing platinum (Pt) nanoparticles into networked single-walled carbon nanotubes (SWCNTs). To investigate the growth behaviour of Pt nanoparticles, we systematically controlled the UV irradiation intensity and exposure time. These processing factors significantly influenced the formation behaviour of Pt nanoparticles in regards to diameter and density. Utilizing the photoreduction process, the sidewalls of SWCNTs were uniformly functionalized with Pt nanoparticles synthesized under optimal UV conditions. For application as practical chlorine (Cl_2) sensors, the sensing performance of Pt nanoparticle-functionalized SWCNTs for Cl_2 was compared against the injection of other gases such as nitrogen dioxide, ammonia and carbon monoxide. The results indicate that UV irradiation is an effective way to functionalize the sidewalls of SWCNTs with catalytic Pt nanoparticles. In addition, the Cl_2 selectivity and response of SWCNT-based gas sensors were enhanced by functionalization with catalytic Pt nanoparticles.

Bio / Medical   Materials / Systems   Energy / Environment   **Research Highlights**   KIST News   Up Close   Interview

Flexible piezoelectric polymer-based energy harvesting system for roadway applications

In Ki JUNG, Youn Hwan SHIN, Sang Tae KIM, Ji Young CHOI, Chong Yun KANG

cykang@kist.re.kr

Interest in energy harvesters has grown rapidly over the last decade. The research effort in large-scale energy harvesting has mainly focused on piezoelectric ceramic-based devices due to their high piezoelectric constants. In this study, we demonstrate a piezoelectric energy harvester module based on polyvinylidene fluoride (PVDF) polymer for roadway applications. Flexible energy harvesters were fabricated with PVDF films and exhibited stable performance and durability over a repeated number of bending cycles. In order to structurally optimize the design, finite element analysis was performed on two possible module configurations, with detailed input conditions on how the flexible energy harvester had to be bent. A piezoelectric energy harvester module was then constructed with the fabricated unit energy harvesters inserted in the vertical direction with initial radii of curvature as high as possible. The module was tested with a model mobile load system (MMLS3) and exhibited up to 200 mW instantaneous power output across a 40 kΩ resistor. The power output scaled linearly with the number of parallel connected harvesters. The calculated power density at this impedance reached 8.9 W/m^2, suggesting that flexible energy harvesters based on piezoelectric polymers may provide energy density as high as those based on piezoelectric ceramics.

Interfacial reactions in the Li/Si diffusion couples: origin of anisotropic lithiation of crystalline Si in Li–Si batteries

Yong Seok CHOI, Jun Hyoung PARK, Jae Pyoung AHN, Jae Chul LEE

jpahn@kist.re.kr

As opposed to the common understanding that diffusion into a cubic-structured single crystal is independent of its crystalline orientation, the diffusion of Li to crystalline Si (c-Si) is anisotropic, which is the major cause of fracture in Si anodes in Li-ion batteries. Here, by conducting comprehensive multi-scale simulation studies based on molecular dynamics and density functional theory, we elucidate how and why Li diffusion in c-Si is anisotropic. We found that Li ions diffuse to c-Si by following a particular atomic-scale space corresponding to the lowest value of the valence orbital in c-Si, causing Li ions to take a tortuous diffusion pathway. The degree of pathway tortuosity differs depending on the crystallographic orientation of Si and is a major cause of anisotropic lithiation. We also developed a structural parameter that can quantitatively evaluate the orientation dependency of the lithiation of c-Si.

Solar energy dehumidifying and cooling air system

US 9702572B2(2017.03.14), KR 101594422B1(2016.02.17)

Dae Young LEE, Sung Chul SHIN

ldy@kist.re.kr

Provided is a solar dehumidifying and cooling system including a solar hot water device that produces hot water by using solar heat and a dehumidifying and cooling device that performs cooling through heat exchange with the hot water that is supplied from the solar hot water device.
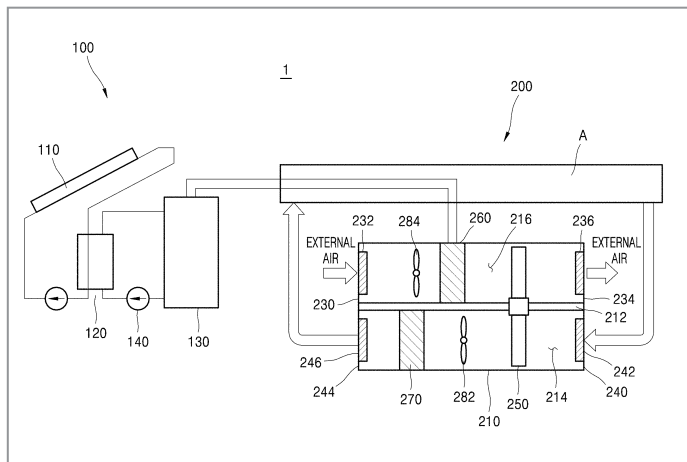

Manganese tin oxide transparent conducting oxide and transparent conductive film using the same and method for fabricating transparent conductive film

US 9704610B2(2017.07.11), KR 101700884B1(2017.02.01)

Ji Won CHOI, Won Kook CHOI, Jin Sang KIM, Hae Na YIM

jwchoi@kist.re.kr

Disclosed is a manganese tin oxide-based transparent conducting oxide (TCO) with an optimized composition, which has low surface roughness, low sheet resistance and high transmittance even when deposited at room temperature, a multilayer transparent conductive film using the same and a method for fabricating the same. The manganese tin oxide-based transparent conducting oxide has a composition of $Mn_xSn_{1-x}O$ (0<x≤0.055), and the multilayer transparent conductive film includes: a manganese tin oxide-based transparent conducting oxide having a composition of $Mn_xSn_{1-x}O$ (0<x≤0.055); a metal thin film deposited on the manganese tin oxide-based transparent conducting oxide; and a manganese tin oxide-based transparent conducting oxide having a composition of $Mn_xSn_{1-x}O$ (0<x≤0.055) deposited on the metal thin film.
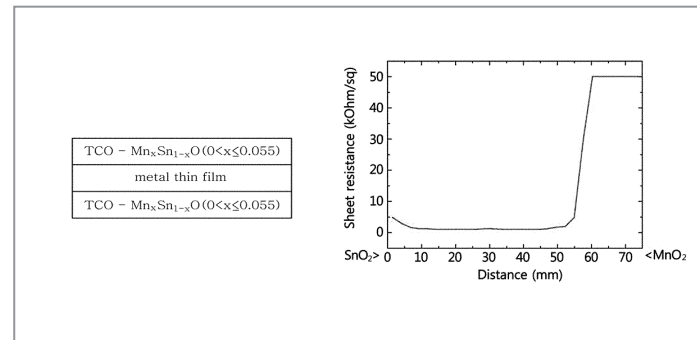
Method of fabricating nanoantennas array, nanoantennas array chip and a structure for lithography

Kyeong Seok LEE, Won Mok KIM, Taek Sung LEE, Wook Seong LEE, Doo Seok JEONG, Inho KIM

kslee21@kist.re.kr

A method for fabricating a nanoantenna array may include forming a resist layer on a substrate, forming a focusing layer having a dielectric microstructure array on the resist layer, diffusing light one-dimensionally in a specific direction by using a linear diffuser, forming an anisotropic pattern on the resist layer by illuminating the light diffused by the linear diffuser on the focusing layer and the resist layer, depositing a material suitable for a plasmonic resonance onto the substrate and the resist layer on which the pattern is formed, and forming a nanoantenna array on the substrate by removing the resist layer and the material deposited on the resist layer. A light diffusing angle by the linear diffuser and a size of the dielectric microstructure are determined based on an aspect ratio of the pattern to be formed.
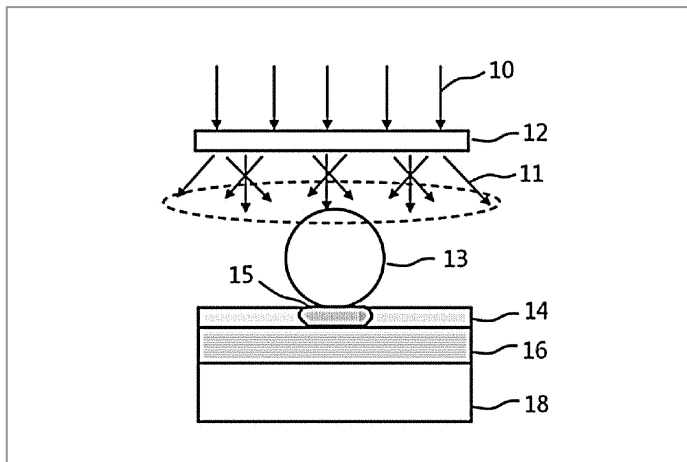

Apparatus and method for generating facial composite image, recording medium for performing the method

Ig Jae KIM, Young Ju CHOI, Yu Jin HONG

drjay@kist.re.kr

Disclosed is an apparatus for generating a facial composite image, which includes: a database in which face image and partial feature image information is stored; a wireframe unit configured to apply a face wireframe to a basic face sketch image, the face wireframe applying an active weight to each intersecting point; a face composing unit configured to form a two-dimensional face model to which the wireframe is applied, by composing images selected from the database; and a model transforming unit configured to transform the two-dimensional face model according to a user input on the basis of the two-dimensional face model to which the wireframe is applied. Accordingly, a facial composite image with improved accuracy may be generated efficiently
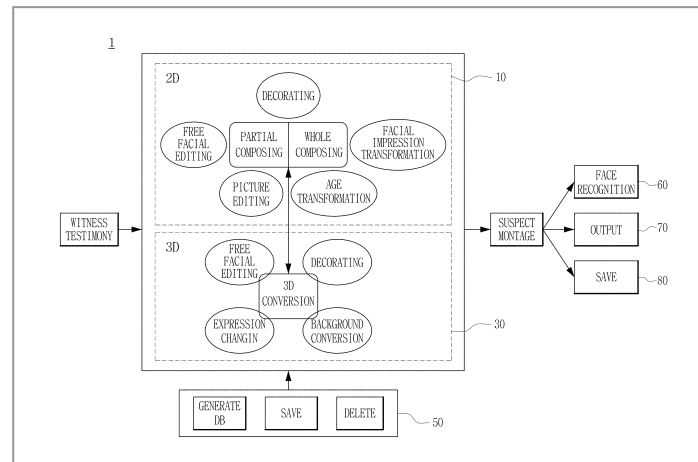
Optical logic gates and method for generating logic signals using DNA-based nanostructure

Chul Ki KIM, Jae Hum KIM, Byeong Ho PARK, Seok LEE, Chan Jun SEONG, Tak Jin LEE

chulki.kim@kist.re.kr

An optical logic gate includes: a DNA-based nanostructure including DNA and metal nanoparticles coupled to the DNA, the DNA-based nanostructure being configured to rotate a polarization plane of an incident light; a polarizer to which light passing through the DNA-based nanostructure is incident, the polarizer being configured to extract a component in a direction of a predetermined reference axis from light whose polarization plane is rotated by the DNA-based nanostructure; and a detection unit to which light passing through the polarizer is incident, the detection unit being configured to generate a logic signal based on a result obtained by comparing the intensity of the component in the reference axis direction extracted by the polarizer with a predetermined threshold value.
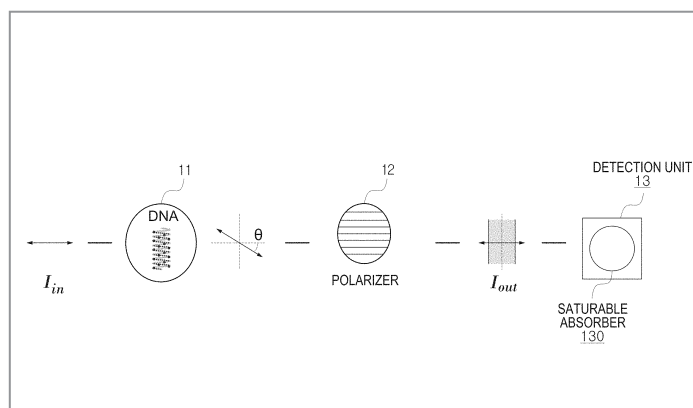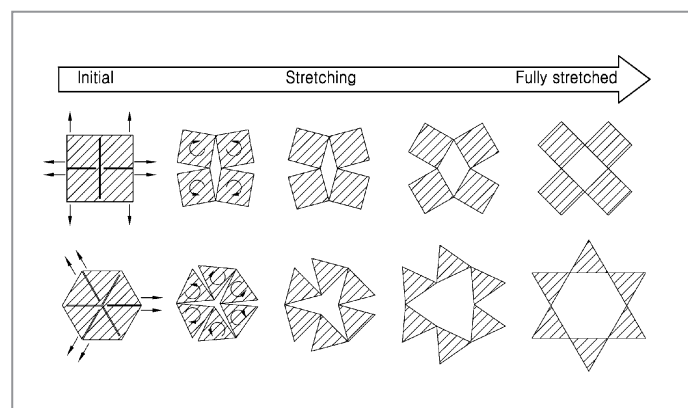
Shape changeable material having inherent shapes using hierarchical structure and electrode having same

In Suk CHOI, Yi Gil CHO

insukchoi@kist.re.kr

A shape changeable material includes a hierarchical structure including a basic displacement unit that includes a basic separation structure and basic unit cells, and a higher level displacement unit located inside the basic unit cell and including higher level unit cells distinguished from each other by a higher level separation structure, in which a separation structure including the basic separation structure and the higher level separation structure includes joints connecting neighboring unit cells to each other. By further forming a coating layer having electric conductivity, a shape changeable electrode includes a supporter that includes a shape changeable material, and the electric conductive coating layer provided on the supporter.

Bio / Medical   Materials / Systems   Energy / Environment   **Research Highlights**   KIST News   Up Close   Interview

Science News

Regional response needed to tackle the issue of fine particle air pollution

Northeast Asian countries must all recognize that we live in a community where we breathe the same air and set long-term objectives that are consistent with economic growth

Without being obvious at first, fine dust has been sweeping across the Korean Peninsula every fall and continuing until late spring. Add to that the yellow dust coming from Mongolia and China in the springtime and it's no surprise that some people talk of putting on gas masks.

Fine dust and air pollution are not problems unique to South Korea, nor are they new. Japan is a good example of a northeast Asian country that has experienced and overcome severe air pollution caused by industrialization. In 2003 South Korea passed legislation known as the *Special Act on the Improvement of Air Quality in the Seoul Metropolitan Area*. After that, focused efforts to improve Seoul's poor air quality proved effective as the city saw annual fine dust concentrations gradually decrease until 2012. However, since the occurrence of the severe fine dust smog that swept across all of China in January 2013, Korea has frequently experienced high concentrations of fine dust, and annual concentrations of this pollutant have remained steady, causing people to become increasingly anxious about what has become a natural disaster that calls for an urgent solution.

Fine dust has existed ever since human beings started using fire. The production of energy emits various pollutants into the air that contribute to climate change, pollutants such as carbon dioxide, fine dust, nitrogen oxide, sulfur oxides, and carbon monoxide. South Korea also suffered from serious air pollution during the country's industrialization period in the 1960's, spurring the country to implement policies for reducing pollution, such as replacing coal with city gas for residential fuel, reducing the sulfur content in gasoline, and continuously strengthening emission standards for factories and automobiles. These changes, however, were expensive.

China has been experiencing steep economic growth in recent years thanks to rapid industrial development. Such growth inevitably requires the use of energy, and China's energy use is rising fast. Coal, which is relatively high in pollutant emissions, represents 70% of China's current fuel consumption. It is surprising that no one pointed out that this would bring about such a disastrous deterioration in northeast Asia's air quality. Korea's vulnerability, reflected in our lack of preparedness in confronting such issues, is clearly evident in today's fine dust situation.

China's current fine dust pollution stems primarily from the rise in the energy consumption fueling its industrialization and economic growth. Undoubtedly, this issue will be addressed in the future, as was the case with South Korea and other advanced nations, but until then, we can't escape from the frequent and severe fine dust smog brought by wind blowing eastward from China to Korea.

Mobile air quailty monitor for creating air pollution map
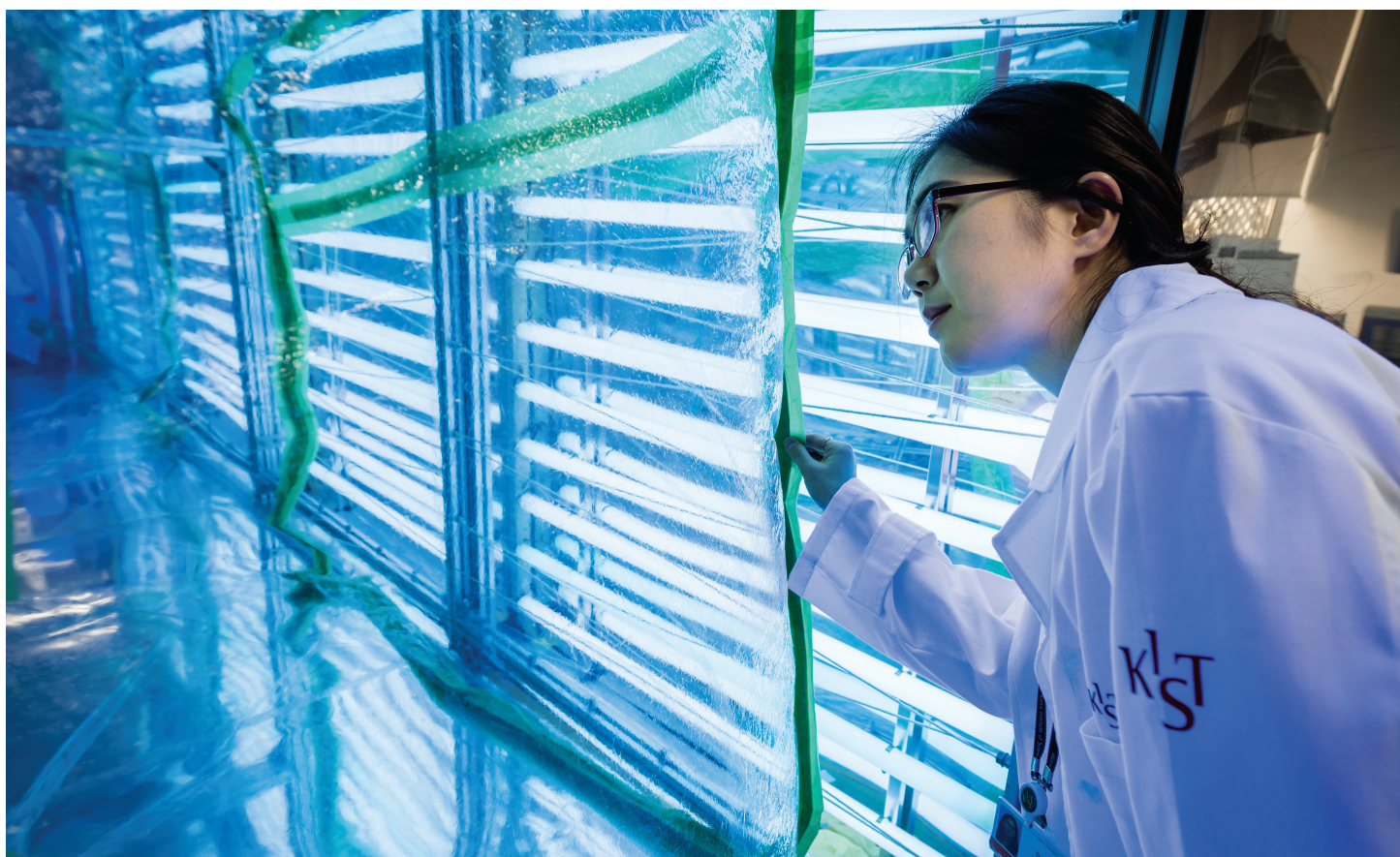
Dr. Hwa Jin LEE (Center for Environment, Health and Welfare Research) measures ozone concentration level using smog chamber

To respond to the sharp rise in fine dust and the damage it brings, South Korea's science and technology agencies are striving to develop technologies that measure and monitor fine dust levels and remove the dust. The director of the Center for Particulate Air Pollution and Health, Dr. Gui Nam BAE, has developed a mobile air quality monitor which is capable of creating a high-resolution air pollution map, and Dr. Se Gyu JANG of KIST Jeonbuk has developed the world's first ceramic filter that filters out 99.9% of ultrafine particles. In addition, the Ministries of Science and ICT, Environment, and Health and Welfare are working together to address pollution issues, an example being the jointly held "Northeast Asia Forum on Air Pollution and Health" whose purpose was to discuss solutions to the fine particulate pollution that affects the entire northeast Asian region.

In the end, a wise response to the damage caused by fine dust requires an urgent nationwide strategy. Before a national approach can be effected, however, all northeast Asian countries must first accept a trans-regional vision that we live in a community where we breathe the same air, and step-by-step measures must be implemented to reduce fine particulate air pollution. Countries must establish long-term forecasts of fine dust that accurately reflect the region's use of energy, economic growth, and other environmental changes. These forecasts will then enable the establishment and implementation of realistic policies on a domestic level.

KIST News

KIST transfers a nanostructure-based oil-water separation technology to Cheongsu Industry

A team from KIST's Computational Science Research Center, led by Dr. Myoung Woon MOON, has succeeded in developing the world's first marine pollution prevention technology that uses a nanostructured oil-scooper. This new oil-removing method uses a large-scale nanostructuring technology to create a curved scooper which allows water, but not oil, to pass through it. By capturing the oil in this way, the scooper can remove oil directly from a spill site. The main feature of this advanced and highly efficient technology is the use of the plasma method to construct a high aspect ratio nanostructure on the surface of a porous hydrophilic material. A thin film forms on the surface of the oil-scooper upon contact with water. Gravity pulls the water, but not the oil, through the scooper's openings, trapping the oil for easy removal. This new technology operates very efficiently to reduce the severe environmental and economic damage caused by oil spills and represents a highly innovative approach as it requires no power source, is easy to use, and enables the reuse of separated oil.

At a signing ceremony held at KIST's Seoul campus, KIST agreed to transfer this advanced technology to Cheongsu Industry and cooperate in its commercialization with the aim of entering the global marine pollution prevention market. This market is expected to grow to USD 13.4 billion globally and KRW 800 billion domestically by 2020. Through the technology transfer agreement, Cheongsu Industry's commercialization strategy will be applied to KIST's new technology to create a profitable business.

According to KIST president Dr. Byung Gwon LEE, "In light of the increasing global demand and need for technologies to fight marine pollution, this technology transfer will be a steppingstone to combat ocean pollution and reduce the economic impact of oil spills, thereby creating high added value." Cheongsu Industry president Gye Dong OH confirmed these comments and added, "We will use this innovative oil-water separation technology from KIST to become a leader in Korea's marine pollution prevention market. We will also take a leading role in the global market in order to solve emerging environmental problems around the world."

Bodyfriend and KIST agree on joint R&D to build healthcare platform with focus on medical massage chairs

On Dec 22, KIST and Bodyfriend, a Korean company providing smart wellness products, signed a joint R&D agreement to develop a healthcare product platform with a focus on medical massage chairs. According to the agreement, Bodyfriend will contribute KRW 10 billion to KIST for research over the next five years.

Bodyfriend, which has grown into Korea's leading massage chair brand, agreed to cooperate with KIST to develop exclusive core technology for massage chairs. In addition, the two institutions will work together to develop and transfer relevant technologies with the goal of developing massage chairs into a medical healthcare product line. Bodyfriend and KIST will perform R&D in a variety of advanced fields of technology, including robotics, AR·VR, mechanical engineering, healthcare, biomedical engineering, and brain science, to develop massage chairs. In the short term, the two organizations will work to standardize technologies used for product manufacturing while securing the future technologies needed to develop an advanced healthcare platform in the mid- to long term.

Bodyfriend will contribute KRW 10 billion (KRW 2 billion annually for five years) to research and set up an on-site lab at KIST. By agreeing to an "open innovation" type of joint R&D characterized by policies such as the mutual disclosure of technologies and patents, the two institutions expect to establish a new model for cooperation between medium-sized companies and government-funded research institutions.

Dr. Young Wook CHO of KIST's Center for Quantum Information develops method to verify quantum computing

The realization of a quantum computer, with capabilities far beyond those of supercomputers, has been the subject of much attention around the world. Joint research conducted by Korea's leading scientists has found a way to realize and verify quantum computing, which operates under
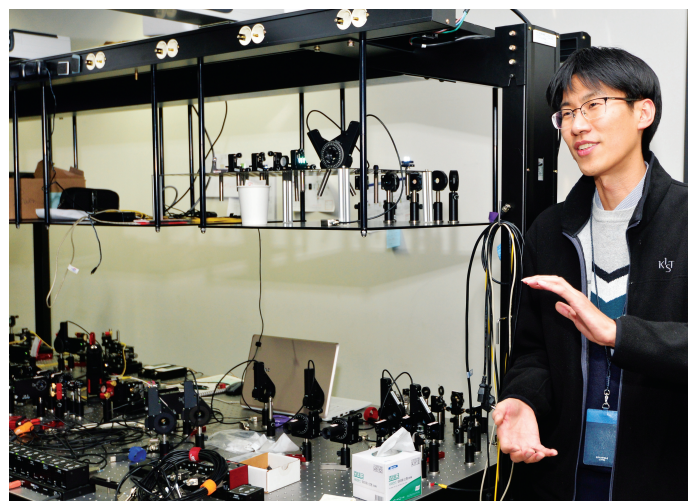
the laws of quantum physics and is considered the foundation for the development of next-generation computers.

Dr. Young Wook CHO's team at KIST's Center for Quantum Information carried out joint research with a Pohang University of Science and Technology (POSTECH) team led by Dr. Yoon Ho KIM. Their work represents a new form of convergence research based on KIST's Open Research Program (ORP). The researchers announced that they have found a new and efficient method to verify a quantum computer's operational process.

The research results break the long-held belief in quantum physics that two incompatible observables cannot be measured at the same time. The researchers showed that two observables can be measured simultaneously and used these findings to devise an efficient method of verifying quantum computation.

According to the uncertainty principle, a well-known principle in quantum mechanics, incompatible observables exist. For example, a particle's position and momentum cannot be measured at the same time because the act of measuring will disturb the quantum state. The KIST-POSTECH study used the most standard method of quantum measurement called the "weak measurement." By not entirely breaking the quantum state, researchers succeeded in measuring incompatible observables at the same time. The study also demonstrated potential applications of such quantum measurement in efficiently verifying a quantum

computer's operational process, which was shown through experimental investigation using a single-photon qubit.

This research is significant in that it was carried out by a consortium of exclusively Korean scientists through the ORP, and the results are expected to contribute to the development of large-scale quantum computers in the future.

"Quantum information technology, one of the most cutting-edge technologies of the future, is increasingly gaining interest around the world," said KIST's Dr. Cho. He added,"Our work was carried out as basic science research to develop quantum computers. We expect the results will be used widely across quantum information technology, where fundamental principles of quantum physics are applied directly, and will contribute greatly to building a research foundation for quantum computing."

This research was conducted as part of KIST's ORP and the National Research Foundation of Korea's Mid-Career Researcher Program and was funded by the Ministry of Science and ICT. The results have been published in the international academic journal *Nature Communications* (IF:12.124) in the January 15, 2018, online edition.

KIST Innovation Forum

On January 25, KIST held a forum on innovation whose theme was "Beyond Miracle, Toward People - Changes in KIST 2018." Discussions at the forum centered on the current and future activities of KIST, particularly the changes required to bring about successful innovation. KIST's vice president, Dr. Seok Jin YOON, set the stage by stating that KIST must now prepare for the next 50 years and present solutions for the problems of a new era.

This year KIST will establish a more people-centric research system and expand R&D that is more relevant to people's needs. This approach will involve increases to funds for research projects run exclusively at KIST and boost individual researchers' autonomy and responsibilities. KIST's management system will be re-designed to further build a

creative talent pool at the institute and maximize researcher capacity in parallel with the government's policy to build a human-focused R&D system.

Specific strategies for implementing changes will be developed in the following four areas: research programs, research methods, research areas, and the research environment.

As regards the first strategy, KIST will strengthen the competitiveness of its basic programs by carefully evaluating the programs and expanding its graded fund allocation accordingly. Participating in pre-studies for government-commissioned projects or assisting in research for the purpose of funding personnel costs will be de-emphasized. Instead, KIST will expand its participation in projects performed exclusively at KIST. It will focus on building a stable research foundation by increasing the funds researchers actually receive.

In terms of research method, KIST will establish research targets and desirable solutions through its demand-based aim-oriented research for the public agenda (K-DARPA) program. This program requires researchers to set a goal with a likely success rate of 10~20% and identify practical solutions. The program will be introduced first in areas related to security, disaster relief and safety and later expanded to other sectors.

KIST plans to continue to identify and develop research areas that will contribute to economic growth through innovation as well as raise people's quality of life. Such paths of inquiry represent uncharted territory but have great potential to fulfill public needs and establish new avenues for industrial growth.

Finally, KIST will focus on creating a research environment where top-quality scientists can build successful careers. It also intends to introduce a special professional track for researchers who produce exceptional results. Recognizing the importance of lifelong learning, KIST plans to offer customized career development where experienced researchers can receive specialized training to further deepen their expertise.

Korean president Moon attends groundbreaking ceremony for VKIST

A groundbreaking ceremony for the Vietnam-Korea Institute of Science and Technology (VKIST) was held on March 22 at Hoa Lac Hi-Tech Park in Hanoi, Vietnam. The VKIST support program was initiated following a Vietnamese government request for Korea's help in establishing a science and technology research center along the lines of KIST for the purpose of economic development through the promotion of science and technology. Since the signing of a joint cooperation agreement in December 2014 between KIST and the Korea International Cooperation Agency (KOICA), planning has been ongoing for the establishment of VKIST operations.

Over the period 2014 to 2020, with a budget of USD 35 million, KIST and KOICA will work with Vietnam's Ministry of Science and Technology to build the VKIST research complex, install research equipment, provide operational consulting and assistance, conduct joint pilot research, and train researchers. For its part, the Vietnamese government will provide a 20-hectare site for the new institute as well as the concomitant utilities such as water and sewage, electricity, and telecommunications.

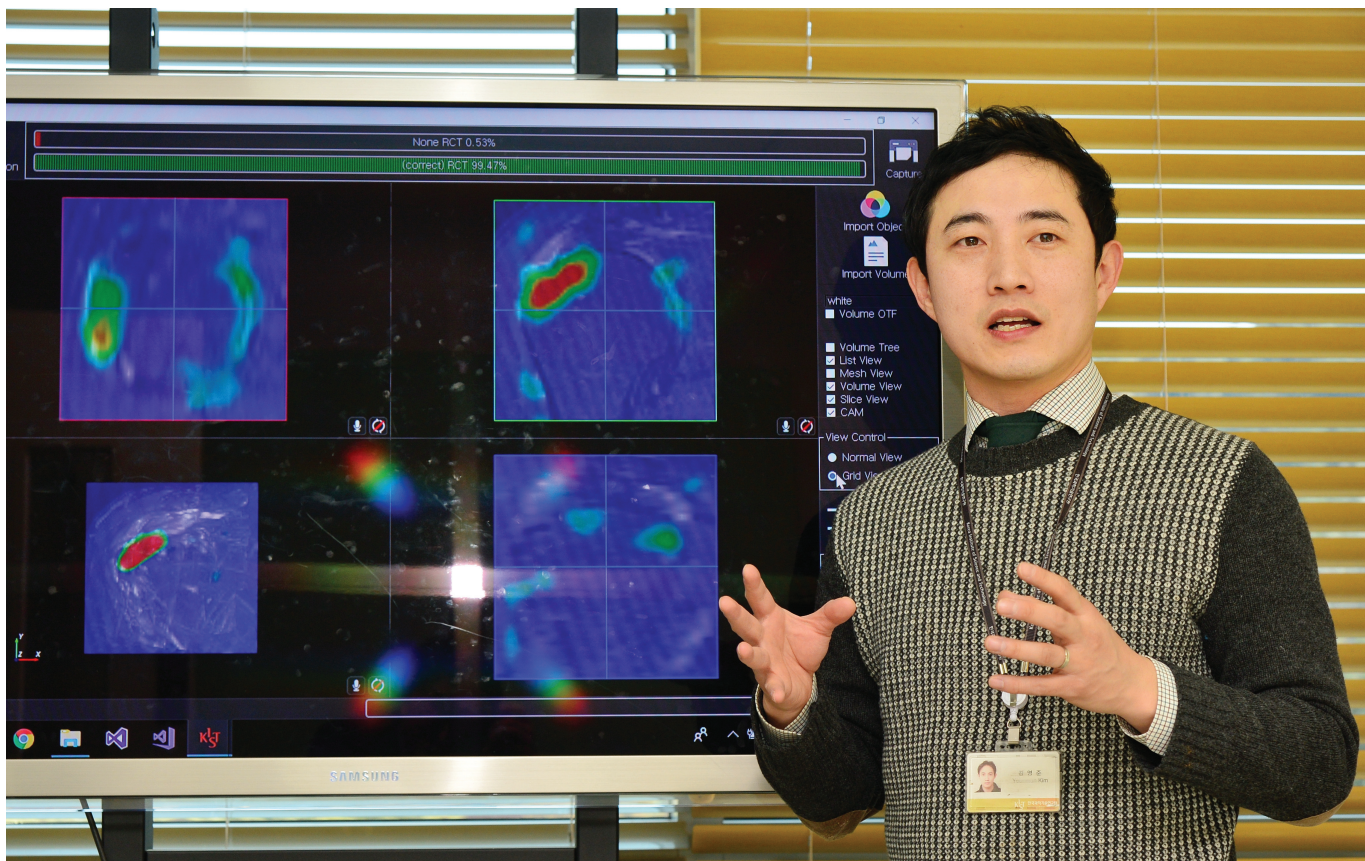To celebrate the successful start of the VKIST support program, the president of South Korea, Jae In MOON, was joined at the groundbreaking ceremony by the vice president of Vietnam, Dang Thi Ngoc Thinh, the Vietnamese minister of science and technology, Chu Ngoc Anh, the Korean minister of science and ICT, Young Min YOO, Korea's National Research Council of Science and Technology chairman, Kwang Yun WON, KOICA's president, Mi Kyung LEE, KIST's president, Byung Gwon LEE, and VKIST's president, Dong Wha KUM.

President Moon underscored the importance of the event by saying, "The groundbreaking of VKIST brings Vietnam a step closer to achieving its dream of building a modern industrial nation." He added, "I firmly believe that VKIST will drive Vietnam's industry and future growth engines while contributing significantly to the creation of a RoK-ASEAN community."

The VKIST support program symbolizes the future of Korean-Vietnamese relations built on mutual growth and economic cooperation. It represents an expansion of the relationship with Vietnam, a key partner in the Korean government's "New Southern Policy," a foreign policy initiative that goes beyond economic and cultural exchange into scientific and technological cooperation. Going forward, VKIST will serve as a base for science and technology exchange and cooperation between the two nations, particularly in the fields of ICT and biotechnology.

During the ceremony, small and medium-sized businesses from both nations held technology exhibitions and corporate exchange events to better understand each other's technologies and needs. Such events will enable KIST to gain insight into Vietnam's technological research demands from the earliest planning stages and thus design VKIST's operations to focus on research that Vietnam's private sector truly needs. In taking measures such as this, KIST will continuously promote technology transfer and business cooperation between Korean and Vietnamese companies.

Bio / Medical

Materials / Systems

Energy / Environment

Research Highlights

KIST News

Up Close

Interview

The Fourth Industrial Revolution and Digital Healthcare

Young Jun KIM

Principal Researcher
Center for Bionics
Biomedical Research
Institute

junekim@kist.re.kr

Controversy regarding the Fourth Industrial Revolution (4IR) is intense. The term is omnipresent in headlines and policy reports these days, but if you ask experts, many feel uncomfortable about all the fuss. Some experts have even given the term a new name - the "False"Industrial Revolution - out of concern that people don't fully understand the term 4IR which could lead to support for inappropriate government policies. My recently published textbook on programming displays the phrase "Key Technology in the Fourth Industrial Revolution" in embarrassingly large print on the cover. My plea to omit the

phrase was met with a flat refusal by the publisher, who defended it for marketing reasons. Amid controversy over the term 4IR, "digital healthcare" technology is emerging as a new growth driver in this era of change. Digital healthcare merges healthcare with various IT technologies, such as artificial intelligence (AI), big data, 3D printing, virtual and augmented reality, the Internet of Things, and robots.

Despite its conservative tendencies, the healthcare industry has become a key sector in the 4IR era of super-intelligence and hyper-connectivity and has been one of the first sectors to vigorously adopt deep learning (deep reinforcement learning), an innovative version of machine-learning AI based on big data. There have been various attempts to apply this technology in healthcare's core functions of diagnosis, treatment, and prognosis analysis, such as diagnosing cancer, analyzing lung images, and predicting heart disease. The medical industry is also actively adopting 3D visualization techniques, including 3D printing and virtual·augmented reality. Just take a look at today's surgical robots. Constant developments are being made in microbots that can be used in neurosurgery, ophthalmology, and cardiac surgery, as well as robotic systems for radiation therapy that can now track disease areas in real time.

The Finnish government, in its search for a new growth engine after the fall of Nokia, has focused on digital healthcare. As a result of the government's extensive support, Finland has pioneered a five billion euro market by connecting digital healthcare with medical welfare. Even the notoriously strict US FDA has taken steps to relax digital healthcare regulations by issuing the "Digital Healthcare Innovation Action Plan," which aims to modernize relevant policies and increase expertise. Japan is also showing strong policy support for digital healthcare. For example, the effectiveness of mock operations prior to surgery has been recognized by the government and taken into account when setting medical insurance fees. That is why I welcome the Korean government's recent announcement to make regulatory reforms in new industries/technologies and implement "regulatory sandboxes" where regulations are initially light but later tightened as appropriate in response to specific issues. An example of this approach is the UK's pro-FinTech policy.

Such changes should be applied to digital healthcare. For instance, institutions should be allowed to cooperate in setting up big data on patient information where personally identifiable information (PII) has been encrypted. I also propose 3D simulations for high-risk and highly complex operations and reflecting 3D printing-based operations when setting medical insurance fees. Korea has world-class IT as well as advanced medical systems and physicians. Digital healthcare can become a new growth engine for Korea that helps us compete with advanced countries as well as rapidly growing China. Let's not fuss over the term 4IR. It is time we focus on designing ways that can push Korea into becoming a powerful digital healthcare nation. Proactively easing regulations, speedily reflecting approved new technologies in medical insurance fees, and setting polices that actively promote relevant industries can be a good start.

Unraveling the secrets of brain function at KIST
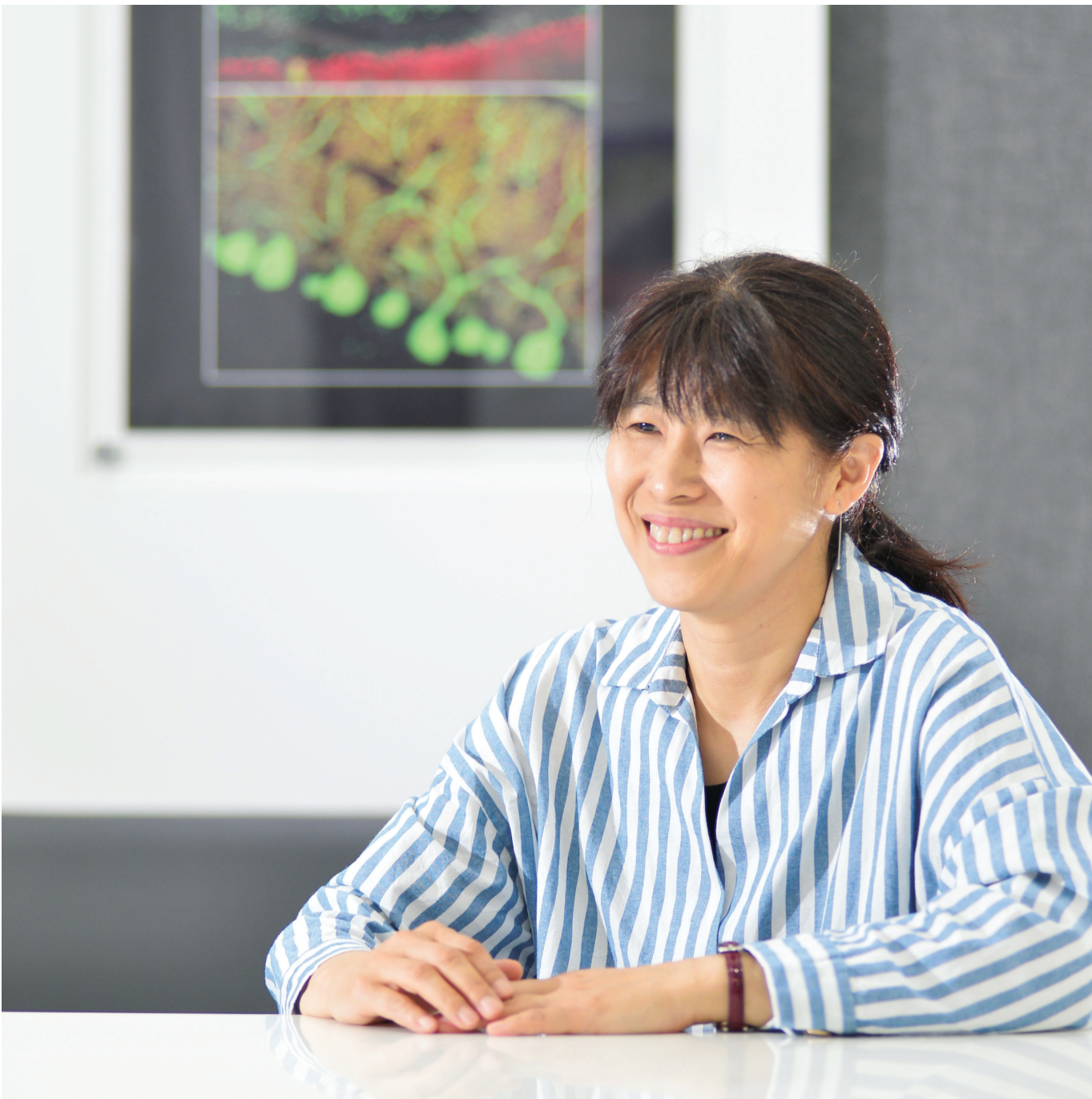
Exploring Brain connectivity

"If you ask me what cure my research is trying to find, I would reply that I am not doing any research related to curing disease. I am focused on defining how our brains work. Without that knowledge, we end up conducting random, rather than accurate treatment when we do need to cure something."

Dr. Keiko Yamamoto, who joined KIST through the World Class Institute (WCI) program, is now in her 8th year of doing research at KIST's Center for Functional Connectomics (CFC). During her postdoctoral training, Dr. Yamamoto's advisor was Dr. George Augustine, director of the WCI program. He introduced the program to Dr. Yamamoto, which ultimately led to her joining KIST.

A career in neuroscience

"I am fond of neurons, which have complicated structures rather than a simple round shape. I am still fascinated by them when doing research."

Dr. Yamamoto received her bachelor's, master's and doctoral degrees all in veterinary Medicine. While still a student, she joined a basic research lab in the physiology department, which sparked her interest in how neurons and cells affect our daily lives. What she found particularly interesting was cell signaling, which is a cell's response to external stimuli, such as hormones. This interest ultimately led to her decision to become a neuroscientist.

Understanding brain function mechanisms

The CFC, where Dr. Yamamoto is a principal research scientist, is an international cooperative lab designed to study brain connectivity and its functions. The human brain is extremely complicated in structure, so the first step in research is to create a map of brain connections followed by investigation into the functions of those connections. Dr. Yamamoto says that these two steps guide her research and that of her colleagues at the CFC. Their work is facilitated by the CFC, which is one of the world's most advanced research labs for the study of not only how the brain functions, but also how its complex parts are connected.

While Dr. Yamamoto makes a clear distinction between research on brain function mechanisms and research on brain-related disease, she stresses that both approaches are important. For example, she says that while today's antidepressants can be effective, it's not clear in what ways they work. Also, antidepressants don't work for everyone - they often cause unwanted side effects. That is why a deeper understanding of brain mechanisms can help define what is causing a brain disease and how to treat it. Take for example a broken car. Dr. Yamamoto explains that having a good understanding of the car's structure and systems will enable you to fix the car more effectively than in the absence of such knowledge. Likewise, understanding the brain's structure and mechanisms can suggest options for people who are working on developing a cure for brain disease and provide a better way to understand it. Dr. Yamamoto says that as the scope of brain science expands, different approaches for understanding the brain system as well as varied treatment options are all necessary for finding a path forward in treating brain disease.
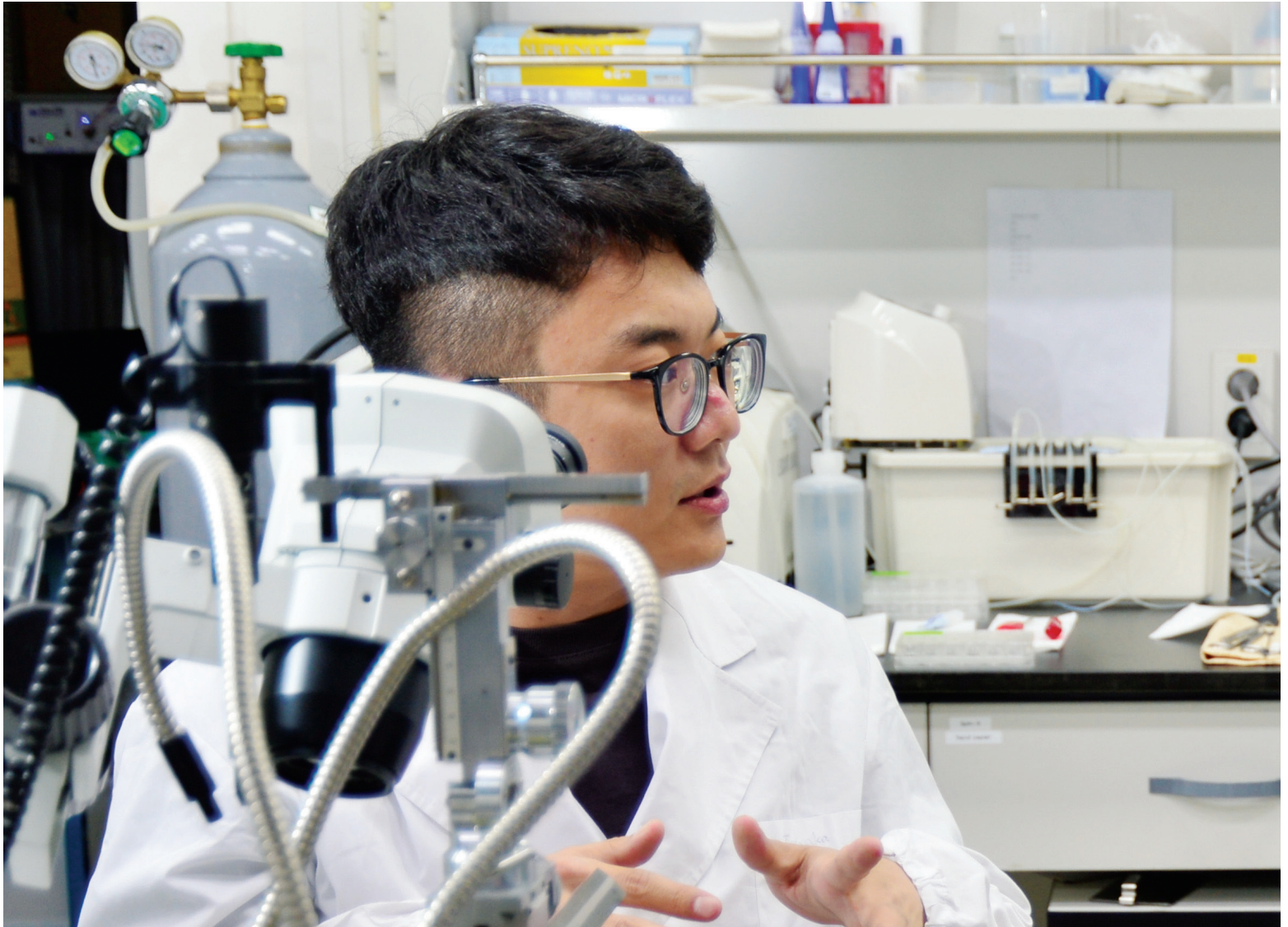
Defining the stable learning mechanism of the cerebellar synaptic system

The cerebellum is the part of the brain where Dr. Yamamoto's research is currently focused. Last September, the journal Nature Communications published her findings on defining the learning mechanism of the synaptic system in the cerebellum. Her paper was entitled, "Timely regulated sorting from early to late endosomes is required to maintain cerebellar long-term depression."

The cerebellum is an important part of the brain that is responsible for the orchestration and fine-tuning of movements, such as walking straight or moving the eyelids or pupils. Such cerebellar activity occurs when the signaling efficiency between immense number of neurons inside the cerebellum changes and is maintained in that changed state. Dr. Yamamoto, together with Dr. Tae Gon KIM, developed a new optogenetic protein (LOV-Rab7TN) that deactivates intercellular transport only when it absorbs blue light. They used this methodology to examine how the synaptic changing/maintaining switches work. Through these experiments, the research team proved their theory that the intercellular

endosomal pathway is the core mechanism responsible for the changing/maintaining of signaling efficiency and revealed the switching system that enables the changing/maintaining of signaling efficiency within the cerebellar synaptic system.

Dr. Yamamoto attributes the beauty of Purkinje cells to her interest in defining cerebellar mechanisms. Because long-term synaptic depression experiments involve visual examination primarily of cerebellar granule cells and Purkinje cells, Dr. Yamamoto is able to watch these lovely Purkinje cells on a regular basis and enjoys doing it. She adds that Purkinje cells are not only beautiful, but are also useful for the photoactivation process in many experimental situations, another reason she likes them so much.

According to Dr. Yamamoto, the mechanism defined by her recent research is a system utilizing cellular events common to all cells and can thus be connected to learning mechanisms elsewhere in the brain. She also believes her research can make a significant contribution in the rehabilitation of patients who have difficulty fine-tuning their movements or learning such control.

Life as a researcher in Korea

"People are nice and help each other here."

  Dr. Yamamoto says that her biggest challenge in her recent research was to find a new optogenetic tool for making accurate examinations. She expressed gratitude to her colleagues who gave her so much help in resolving this issue.

  Asked if she had any difficulty adjusting to life in Korea, she answered that she received a lot of help from friends and colleagues, and though not everything went as smoothly as planned, she was able to solve many problems thanks to the people around her.

"When I moved my lab to Korea, I took accurate measurements of the lab space and ordered desks and shelves accordingly. But when I tried to install the last shelf, it was 2 cm too long. I knew I could not fix this myself, so I asked the people who were helping me with the lab relocation and installation if this could somehow be fixed. The next day, I was surprised to find that they had taken the shelf back to the factory to cut 2 cm off, and the shelf now fit exactly right. I was deeply impressed by their quick action and kindness."
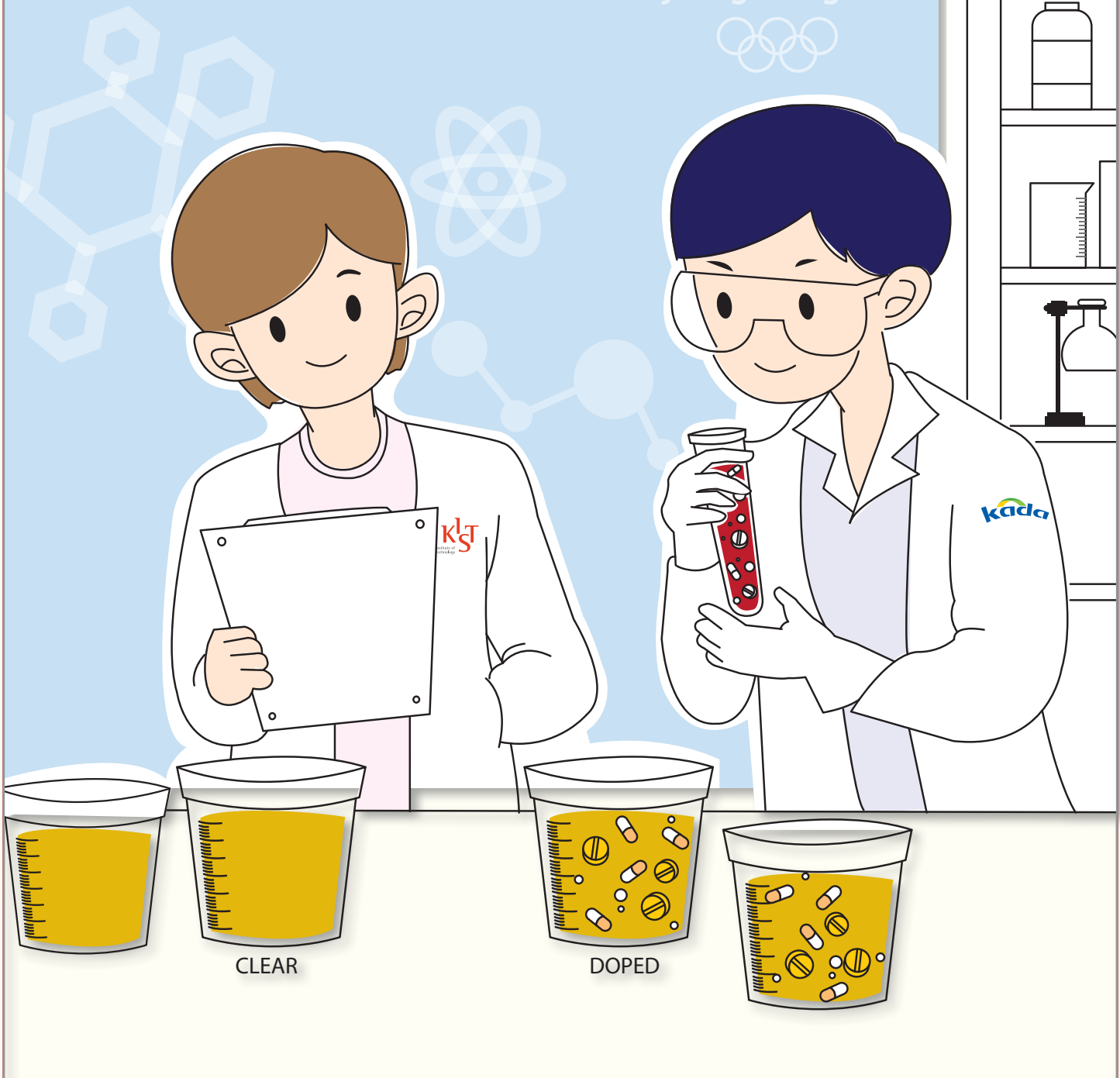
  Dr. Yamamoto adds that whenever she asked for help and explained any urgent requirements, she received the help she needed. Because her colleagues are similarly motivated and passionate about their work, her life as a researcher in Korea has been very positive.
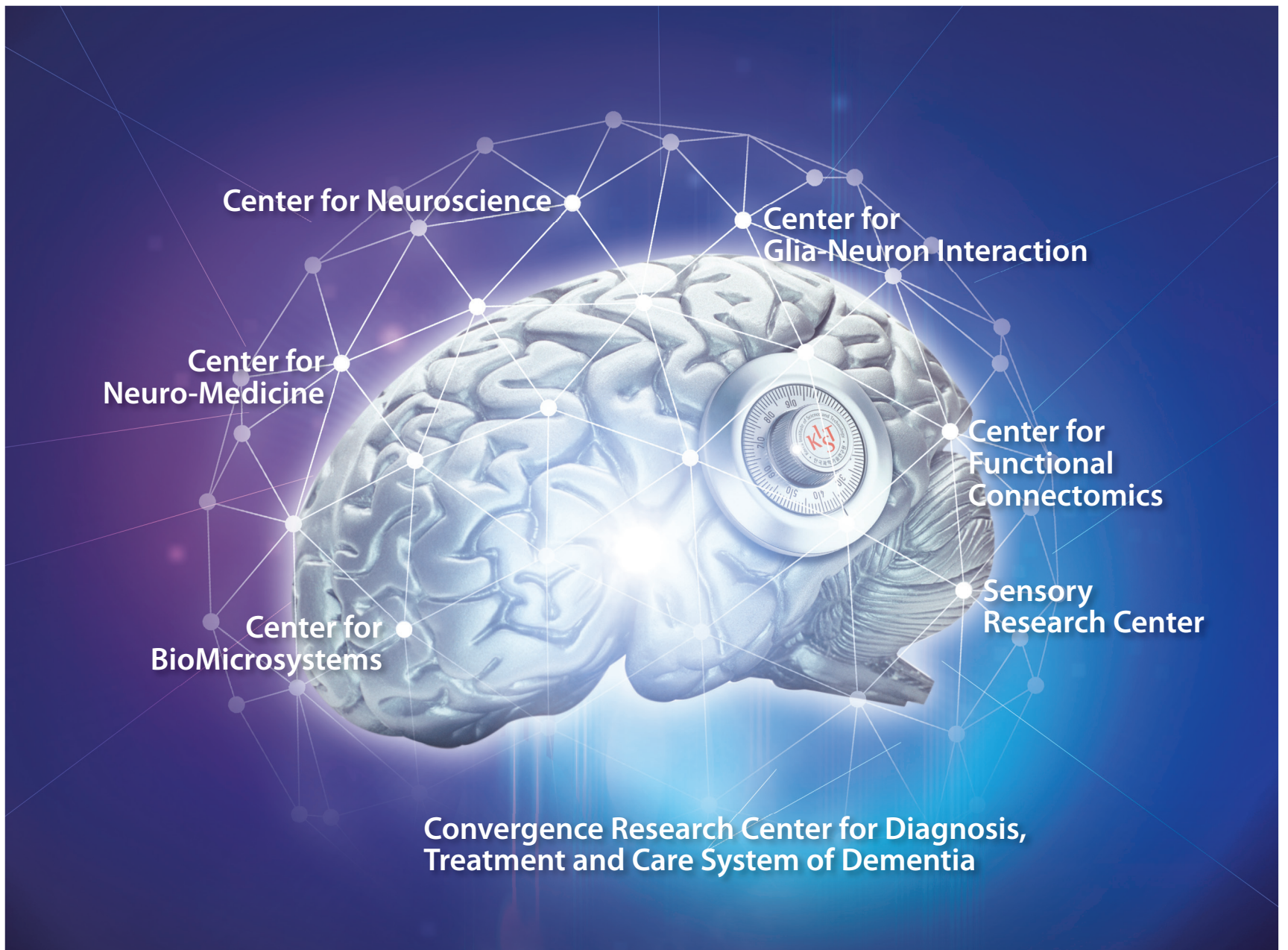
Studying the mobility and cognitive functions of the cerebellum

  Dr. Yamamoto intends to continue her research on the key role the cerebellum plays in movement and learning. In addition, she plans to continue studying the cognitive functions of the cerebellum with the aim of an integrated examination of the brain's two seemingly separate functions of mobility control and cognition. Through such research, she hopes she can contribute to overcoming disabilities in human activity and cognitive function.

Center for Neuroscience

Center for Glia-Neuron Interaction

Center for Neuro-Medicine

Center for Functional Connectomics

Sensory Research Center

Center for BioMicrosystems

Convergence Research Center for Diagnosis, Treatment and Care System of Dementia

Brain Science Institute

The human brain is a highly complex system often dubbed a "miniature universe." Its many mysteries have yet to be unveiled. The Brain Science Institute specializes in convergence research that includes neuroscience, nanoengineering, medicine, and genetics, through which it aims to understand the neural mechanisms responsible for controlling human behavior and to discover ways of overcoming brain dysfunctions. The Brain Science Institute's goal is to unravel the mysteries of the brain and ultimately become the global hub for brain science research.

KIST
Korea Institute of
Science and Technology